

OPTICAL-FREQUENCY MIXERS IN PERIODICALLY POLED LITHIUM  
NIOBATE: MATERIALS, MODELING AND CHARACTERIZATION

A DISSERTATION  
SUBMITTED TO THE DEPARTMENT OF APPLIED PHYSICS  
AND THE COMMITTEE ON GRADUATE STUDIES  
OF STANFORD UNIVERSITY  
IN PARTIAL FULFILLMENT OF THE REQUIREMENTS  
FOR THE DEGREE OF  
DOCTOR OF PHILOSOPHY

Rostislav Vatchev Roussev

December 2006

© Copyright by Rostislav Vatchev Roussev 2007  
All Rights Reserved

I certify that I have read this dissertation and that, in my opinion, it is fully adequate in scope and quality as a dissertation for the degree of Doctor of Philosophy.

---

Martin M. Fejer Principal Adviser

I certify that I have read this dissertation and that, in my opinion, it is fully adequate in scope and quality as a dissertation for the degree of Doctor of Philosophy.

---

Robert L. Byer

I certify that I have read this dissertation and that, in my opinion, it is fully adequate in scope and quality as a dissertation for the degree of Doctor of Philosophy.

---

Stephen E. Harris

Approved for the University Committee on Graduate Studies.



# Abstract

Efficient wavelength conversion is an attractive approach for obtaining coherent radiation in regions of the spectrum where lasers are unavailable or impractical. Optical signal processing in WDM networks, optical-CDMA communications, and quantum communication are examples of applications that can utilize efficient nonlinear frequency conversion at low power levels. Lithium niobate (LN) is a very promising material for the purpose, because it has a mature crystal-growth process, wide transparency range, large second-order nonlinear coefficient, and allows quasi-phasematching via periodic poling (PP). Waveguides enable efficient conversion at low powers and can be formed via reverse proton-exchange. Precise modeling of both the fabrication process and the properties of the resulting waveguides is thus necessary for the demonstration of high-density optical integrated circuits.

This dissertation presents a complete fabrication model that accurately predicts the nonlinear diffusion of protons in PPLN as well as the dispersion of the waveguides between 450 and 4000 nm. Using this model, waveguides are fabricated for two experiments: efficient generation of 3–4- $\mu\text{m}$  radiation for spectroscopy via difference frequency generation using two near-IR lasers; and parametric amplification of 1.57- $\mu\text{m}$  seed signal radiation for remote wind sensing using a 1.064- $\mu\text{m}$  pump laser.

The waveguides are fabricated in conventional congruent-composition LN. Photorefractive damage (PRD) and green-induced infrared absorption (GRIIRA) limit the generated output power in these devices at room temperature due to the presence of high-intensity visible light. Resistance to PRD and GRIIRA can be achieved by heavy doping with  $\text{Mg}^{2+}$ , or by using crystals with stoichiometric composition.

PRD-resistant, bulk near-stoichiometric lithium niobate (SLN) was fabricated by vapor-transport equilibration (VTE) of originally congruent lithium niobate wafers with light MgO (0.3–1 mol%) doping. Details of the poling process and the dependence of photorefractive properties on crystal composition are presented. We obtained periodic poling down to a

period of 7  $\mu\text{m}$  and achieved 2 W at 532 nm via second harmonic generation in a 0.3 mol-% VTE-MgO:LiNbO<sub>3</sub> bulk crystal at room-temperature. These breakthroughs will enable efficient tunable radiation from the visible to the mid-IR for a variety of applications.

# Acknowledgements

I have been very fortunate to pursue my advanced degree at the Stanford University department of Applied Physics, where I had the opportunity to interact with many extraordinary people. They have contributed significantly to my growth as a scientist and as a person. I would like to acknowledge their support.

My research adviser, Prof. Martin Fejer, has helped me not only with difficulties in research, but also in my personal life. Without his support, I would not have gotten this far. I have been amazed at how he always found time to check if students had any difficulties, and to offer very helpful advice. He has done that for me throughout my Stanford years, and I am very grateful to him for that. I have learned a lot from him not only about science, but also about responsibility and devotion. I enjoyed many technical discussions with my adviser, which were both helpful and stimulating. I learned a large fraction of my technical knowledge through direct interactions with him. I would also like to thank him for making time to read and correct my dissertation according to my schedule.

Prof. Robert Byer has been very supportive of my collaborations with members of his group. He has made me believe that a person can be great at many things and need not worry about it. I would also like to thank Prof. Byer for the wonderful presentations about beautiful places around the globe, for reading my dissertation during the only time interval in which I could deliver it and for the encouraging final remarks.

I would like to thank Prof. Stephen Harris for the very stimulating and inspirational presentations that he and his students have given at local symposia. In addition, I would like to thank him for the great care taken in the teaching of the Nonlinear Optics class that I took in my first year. Taking the class was a pleasant learning experience for me. Finally, I would like to thank Prof. Harris for the great support during his reading of my thesis and for the remarks of approval.

I would like to thank the other two members of my thesis defense committee - Prof.

Robert Feigelson and Prof. James Harris, for accepting the responsibility on a short notice, and for making my defense a memorable experience in a good way. I would also like to thank Prof. Feigelson for helpful discussions about lithium niobate and vapor-transport equilibration.

I would not be writing acknowledgements today if it were not for the support of my reading committee and two of my student colleagues – Arun Sridharan and Carsten Langrock. Carsten helped me a lot by proof-reading chapters of my dissertation and providing helpful suggestions. I would like to also thank him for his perseverance throughout our collaborations in the past, which helped us achieve remarkable results, as well as for being a great friend. Arun has been a friend of mine since the beginning of my Ph.D. study. He has helped me many times. We have had a significant amount of joint work and achieved great results together. In addition, I would like to thank him for the superior technical and logistical support related to the writing and submission of my dissertation over the past several weeks.

I would like to thank Roger Route for getting me up to speed on the VTE process, as well as for many thoughtful discussions about materials, processes, and furnace building. In addition, I would like to thank Roger for quality advice about life.

I have been very fortunate to start my Ph.D. studies in the Fejer group under the direct guidance of Krishnan Parameswaran. He spent a long time teaching me everything that he knew about photolithography, periodic poling, waveguide fabrication, waveguide testing, and testing equipment. In addition, he gave me a lot of helpful advice about living in the Stanford area.

I would like to thank Andrew Schober for always showing interest in discussions about physics and optics, and sharing his knowledge. I am also thankful to him for boosting my self-confidence and optimism during hard times. I would like to thank Genady Imeshev for providing me with a good background on short-pulse QPM theory, for our collaboration on MgO-doped LiNbO<sub>3</sub>, and for helpful discussions about career paths after Stanford.

I am thankful to Jonathan Kurz for taking the initiative to pursue a more repeatable fabrication process, and for the collaborative work during my early years at Stanford, when we helped each other solve many technical problems. I would like to thank David Hum for many helpful discussions about near-stoichiometric materials, periodic poling, and many aspects of engineering in general. In addition, I am thankful to Xiuping Xie for developing the code for two-dimensional modeling simulations, as well as for many discussions of the

fabrication process. I would like to acknowledge the significant contributions of Joseph Schaar to the automation of the short-pulse poling process. I am thankful to Paulina Kuo for taking time to satisfy my curiosity about orientation-patterned GaAs, and to Jie Huang for sharing his device fabrication and testing experience.

Besides Arun, other members of the Byer group with whom I have had significant collaboration were Karel Urbanek and Supriyo Sinha. Karel has contributed very significantly in the OPA experiments in Chapter 3 which would not have succeeded without his constant optimization of the pump laser and his participation in the measurement process. In addition, he fixed and optimized the pump lasers for the green SHG experiments described in Chapter 5, and personally made the final measurements, including the curve of SHG power as a function of pump power. I also thank Karel for several outdoor expeditions and for some wonderful times at lake Tahoe, where he managed to gather a large crowd of Byer and Fejer students for some unforgettable experiences. Supriyo built and supported the 1119-nm fiber laser that was used as the pump for the 4- $\mu$ m-DFG experiments, and collected the final data of DFG output power versus pump and signal power. In addition, we have had many interesting discussions about fiber lasers, PPLN crystals. and possibilities to combine them, I am very thankful to Supriyo for our collaboration.

I thank all students from the Byer group for their support with equipment for experiments, their kindness, and humor. I would also like to thank Luigi Scaccabarozzi and Ke Wang from the J. Harris group for being great friends and helping me pass the time when my wife and daughter were on the east coast.

I thank Mordechai Katz for developing the MgO-doped vapor-transport equilibrated lithium niobate to the point that showed its promise as a material resistant to photorefractive damage, and for introducing me to the development process. I also thank him for introducing me to his wonderful family, and for joyful outdoor trips that our families shared. I am very thankful to Romain Gaume for making time for many helpful discussions of chemistry issues that we tried to resolve over the past 3 years. I also thank Sergei Orlov for discussions of the photorefractive effect and near stoichiometric lithium niobate.

I am very thankful to Tim Brand for his support with crystal polishing and dicing. In addition, we had a great time discussing music and life. I am also thankful to Larry Randal for computer and machine-shop support.

I thank Dieter Jundt and Claudia Kajiyama from Crystal Technology for growing the precursor substrates and supplying powders for the VTE-SLN research and for our technical

discussions. I thank Prof. Takunori Taira and Dr. Hideki Ishizuki for helpful discussions about MgO-doped lithium niobate and thermal conductivity.

I would like to thank Alex Alexandrovski, Kostya Vodopyanov, Vlad Kondilenko, Vlad Shur, Greg Miller, Ming-Hsien Chou, Tomas Plettner, Koichiro Nakamura, Douglas Bamford, and Dimiter Shumov, for helpful technical discussions.

I would like to thank Paula Perron and Claire Nicholas for perfect department administrative support during my graduate student years. I also thank Vivian Drew for her kind group-administrative support over the past few years.

I hope to keep in touch with these wonderful people in the future.

I would like to thank my wife's sister Dobrina and her husband Mihail for helping us tremendously over the years of my study. In addition, I would like to thank my parents for bringing me up the way I am, for being supportive of my interest in physics, and for the sacrifices they have made to help me pursue my interests all the way to Stanford.

Finally, I would like to thank my wife Katerina and my daughter Kalina for loving me and making my life wonderful.

# Contents

<b>Abstract</b>	<b>v</b>
<b>Acknowledgements</b>	<b>vii</b>
<b>1 Introduction</b>	<b>1</b>
1.1 Motivation . . . . .	1
1.2 Nonlinear optics . . . . .	3
1.2.1 Generation of new optical frequencies . . . . .	3
1.2.2 Quasi-phasematching . . . . .	5
1.2.3 Efficiency of nonlinear optical frequency mixing . . . . .	9
1.3 Photorefractive damage and damage-resistant QPM materials . . . . .	11
1.4 Overview . . . . .	14
<b>2 Waveguide model</b>	<b>16</b>
2.1 Three-wave mixing in an optical waveguide . . . . .	16
2.2 History of proton-exchanged waveguides . . . . .	21
2.3 Phase diagram of PE LiNbO <sub>3</sub> . . . . .	24
2.4 Previous models of annealed proton-exchanged waveguides . . . . .	26
2.5 Waveguide characterization techniques . . . . .	27
2.5.1 Refractive-index-profile measurements using prism coupling . . . . .	27
2.5.2 Absorption spectroscopy of the OH stretching vibration . . . . .	29
2.6 Model for high-temperature proton diffusion . . . . .	30
2.6.1 Soft anneal . . . . .	30
2.6.2 Assumptions . . . . .	36
2.6.3 Concentration-dependent diffusion in one dimension . . . . .	37

2.7	Wavelength dispersion of proton-exchanged lithium niobate . . . . .	44
2.8	Undercutting and diffusion along the crystal y-axis. Model predictions for QPM for channel waveguides. . . . .	46
2.9	Full-range Sellmeier equation for proton-exchanged LiNbO <sub>3</sub> . . . . .	50
2.10	Propagation losses and mixing efficiency . . . . .	51
<b>3</b>	<b>Mid-IR DFG and OPA</b>	<b>54</b>
3.1	Brief history of mid-IR DFG in PPLN waveguides . . . . .	55
3.2	Mixing efficiency. Design approach. . . . .	56
3.3	Experimental results on mid-IR generation . . . . .	60
3.4	Parametric amplification in RPE waveguides . . . . .	68
<b>4</b>	<b>VTE:SLN</b>	<b>77</b>
4.1	Photorefractive effect in lithium niobate . . . . .	77
4.2	PRD-suppression via doping and stoichiometry control . . . . .	79
4.3	PRD-suppression in lightly-MgO-doped SLN . . . . .	80
4.4	Fabrication method . . . . .	81
4.5	Material characterization . . . . .	82
4.5.1	Photorefractive properties . . . . .	82
4.5.2	Material absorption . . . . .	88
4.5.3	Dispersion of the extraordinary refractive index of SLN . . . . .	90
<b>5</b>	<b>Periodic poling and green SHG</b>	<b>92</b>
5.1	Electric-field poling . . . . .	93
5.2	Domain-wall velocity and nucleation-site density in 0.3 mol-% MgO:SLN . . . . .	98
5.3	Other properties relevant to poling . . . . .	99
5.4	Pulsed periodic poling . . . . .	102
5.5	Results of periodic poling with LiCl electrodes . . . . .	102
5.6	SHG of high-power CW green radiation in PPMgSLN near room temperature	107
<b>6</b>	<b>Conclusion</b>	<b>110</b>
6.1	Summary of contributions . . . . .	110
6.2	Future possibilities . . . . .	112
<b>A</b>	<b>Calibration of the OH absorption measurement</b>	<b>114</b>

<b>B List of acronyms</b>	<b>117</b>
<b>Bibliography</b>	<b>119</b>

# List of Tables

2.1	Time $t$ , temperatures $T$ , thickness $d$ and $\Delta n_e$ measurements from SA study	33
-----	---	----

# List of Figures

1.1	SHG power and QPM. . . . .	7
1.2	Phasematchng in Fourier space. . . . .	9
2.1	$\Delta n$ vs $x$ in PECLN. . . . .	25
2.2	PE index profile . . . . .	30
2.3	SA evolution . . . . .	33
2.4	SA stability . . . . .	34
2.5	SA with slow cooling . . . . .	35
2.6	Planar diffusion profiles . . . . .	40
2.7	Diffusivity dependence on temperature . . . . .	41
2.8	RPE concentration profiles . . . . .	42
2.9	Proton dose decay with RPE time . . . . .	43
2.10	Dependence of diffusivity on concentration . . . . .	44
2.11	Wavelength dependence of $\Delta n_e$ . . . . .	45
2.12	APE waveguide concentration recovered from IWKB profiles at different wavelengths . . . . .	47
2.13	Sketch of the transverse cross-section of a PE waveguide with undercutting	48
2.14	Predicted SHG phasematching in APE waveguides . . . . .	49
2.15	Experimental data for $\Delta n_e(\lambda, C=1)$ and the fitted Sellmeier curve . . . . .	51
3.1	Schematic drawing of a PPLN waveguide device for mid-IR DFG . . . . .	58
3.2	Mode overlap for DFG of 4- $\mu\text{m}$ radiation in a planar RPE waveguide . . . . .	60
3.3	Phasematching signal wavelength versus waveguide width . . . . .	62
3.4	DFG power versus signal power . . . . .	65
3.5	DFG power versus pump power . . . . .	66
3.6	DFG tuning curves taken at different times . . . . .	67

3.7	DFG output power at 3428 nm versus pump power . . . . .	69
3.8	Signal phasematching wavelength of RPE waveguide OPAs versus channel width . . . . .	72
3.9	Signal phasematching wavelength and peak gain of RPE waveguide OPAs versus channel width . . . . .	73
3.10	Temperature tuning of the phasematching signal wavelength of a waveguide OPA . . . . .	75
3.11	Gain of the waveguide OPA versus square root of peak pump power in the pulse . . . . .	76
4.1	A schematic diagram of the photocurrent measurement . . . . .	83
4.2	Specific photoconductivity versus VTE weight gain . . . . .	85
4.3	Saturated space-charge field versus VTE weight gain . . . . .	86
4.4	A beam-fanning comparison between CLN and VTE- 0.3 mol-% MgO:SLN . . . . .	87
4.5	Optical transmission spectra of 1 mol-% MgO:CLN and VTE-MgO:SLN . . . . .	89
4.6	Dispersion of the extraordinary refractive index, $n_e$ , of VTE-SLN . . . . .	91
5.1	Top view of a typical periodic pattern used for poling . . . . .	93
5.2	Schematic comparison of self-termination field caused by uniform planar trapped-charge and localized or non-uniform charge distribution . . . . .	97
5.3	Domain-wall velocity of VTE- 0.3 mol-% MgO:SLN versus applied field . . . . .	98
5.4	Nucleation-site density in 0.3 mol-%MgO:SLN versus voltage normalized to the sample thickness . . . . .	100
5.5	A schematic of the photoresist pattern for periodic poling . . . . .	101
5.6	Typical voltage waveform used in short-pulse poling of MgO:SLN . . . . .	103
5.7	Domain pattern with period of 9.6 $\mu\text{m}$ in 0.28-mm thick 0.3-mol-% MgO:SLN . . . . .	104
5.8	Domain pattern with period of 9.7 $\mu\text{m}$ in 0.28-mm thick 0.5-mol-% MgO:SLN . . . . .	105
5.9	Domain pattern with period of 7 $\mu\text{m}$ in 0.28-mm thick 0.3-mol-% MgO:SLN . . . . .	106
5.10	SHG power inside the crystal at 532 nm versus input pump power . . . . .	108
A.1	Calibration curves for the absorption measurement . . . . .	115

# Chapter 1

## Introduction

### 1.1 Motivation

The advent of the information age has introduced an ever increasing demand for bandwidth on communication systems. Fiber-optic communication systems became prevalent at the end of the last century due to their unmatched capacity for long-haul data transmission. For larger data bandwidth to be available at low cost, higher bit-rates, denser WDM-channel spacings and longer transmitter-receiver spacings are needed. To follow this path, dispersion and nonlinear effects in the fiber must be managed, at increasing level of difficulty. One possible approach to addressing this challenge is mid-span spectral inversion, which can be achieved by optical frequency mixing (OFM), and allows the compensation of both dispersion and nonlinear effects.

Providing larger bandwidth to the end user at low cost can be obtained by increasing the “network transparency”, i.e., bringing the optical signal closer to the user by replacing expensive high-speed signal-processing electronics for multi-user management with all-optical signal processors in the design of a next-generation communication system. This approach has the additional advantage of making signal conversions between the optical and the electrical domain unnecessary. Signal manipulations such as wavelength switching, time-division multiplexing, switching between time-division and wavelength-division multiplexing, picking and delaying of optical data pulses or packets, etc., could be done in the optical domain. These functions can be implemented with the help of optical-frequency mixers. Combining several functions in an integrated optical circuit on a single chip significantly enhances the applicability of optical signal processing but requires accurate modeling

of the device fabrication process and performance.

Demand for secure communications has also grown significantly in recent years. Optical code-division multiple access communication systems may provide increased security by encoded spreading and overlapping of the spectra of multiple information channels. Proper decoding with high suppression of multi-user interference is necessary for data recovery and protection. Nonlinear thresholding performed by frequency doubling of the decoded signal in an optical-frequency mixer drastically improves the contrast between properly and improperly decoded signals.

Theoretically, only quantum communications promise absolute security of information sharing. Quantum key-distribution systems based on single-photon data encoding require low transmission losses and efficient single-photon detection. While propagation losses in optical fibers are lowest in the 1550-nm communications band, detection of single photons in that band has traditionally been done with InGaAs/InP avalanche photodiodes with quantum efficiencies smaller than 15 %, cryogenic cooling and significant “dead time” which limits the data transmission bit rate. The best single-photon detectors, namely, silicon avalanche photodiodes, operate near 700 nm with quantum efficiencies exceeding 70 % and very low rate of dark counts. In addition, silicon avalanche photodiodes do not require cryogenic cooling and their dead time has only a small effect on high bit-rate detection due to a large ratio between the detector area and the area affected by a single-photon avalanche process. Efficient wavelength conversion of 1550-nm single-photon data to 700 nm by using sum-frequency generation in an optical-frequency mixer would make it possible to combine low-loss transmission with efficient detection, allowing secure communication at high data rates.

Bright coherent sources of narrow-line tunable mid-infrared radiation in the range 3000-4000 nm operating near room temperature at milliwatt power levels are of interest to laser spectroscopy and trace gas detection. Such sources at power levels exceeding 100  $\mu$ W are still lacking. Mid-infrared radiation can be obtained by difference-frequency mixing of two solid-state lasers (for example, one operating near 1100 nm, and the other near 1550 nm). This optical-frequency mixing process can also be used to convert the wavelength of optical data channels from the telecommunications band to the mid-infrared and vice-versa, which would allow signal processing with standard telecommunications equipment of data transmitted at mid-infrared wavelengths through free space. When high-energy pump pulses are used, the same mixing process allows the parametric amplification of a narrow-line

1550-nm laser to  $\mu\text{s}$ -pulses with energy levels unavailable from conventional laser sources in this wavelength range. Such pulses are of interest to space-borne wind-velocity sensing.

Lithium niobate is a ferroelectric crystal with high electro-optic and second-order nonlinear coefficients and a wide transparency range (0.3-4.5  $\mu\text{m}$ ). It can be periodically poled, allowing quasi-phasematching for optical-frequency mixing. Large crystals of excellent optical quality are commercially available at low cost. Periodically poled lithium niobate waveguides provide the combination of low propagation losses and high conversion efficiency necessary for the implementation of the functions described earlier.

The traditional powerful Watt-level continuous-wave coherent sources in the range 450-600 nm are based on ion lasers and are very inefficient, with typical wall-plug efficiencies of less than 0.1%. Such lasers can be replaced by frequency-doubled or frequency-summed solid-state lasers, which would increase the energy efficiency by two-to-three orders of magnitude. Lithium niobate has adequate nonlinear coefficient to allow single-pass frequency doubling at these power levels, but the standard optical-grade congruent-composition crystals of this material suffer from photorefractive damage and green-induced infrared absorption in the presence of intense visible or ultraviolet light. Developing methods to suppress photorefractive damage in lithium niobate is still an area of active research due to the significant potential impact for efficient and reliable solid-state laser sources in the visible.

This dissertation provides an accurate model for the fabrication of annealed proton-exchanged and reverse proton-exchanged waveguides in congruent lithium niobate. These waveguides are the basis of integrated optical-frequency mixers optimised for different applications. In addition, a significant portion of the dissertation is devoted to the development of lithium niobate resistant to photorefractive damage by combining light MgO-doping and vapor-transport equilibration.

## **1.2 Nonlinear optics**

### **1.2.1 Generation of new optical frequencies**

The process of optical-frequency mixing involves the generation of new optical frequencies during interaction between an optical field and a propagation medium. If the response of the medium to the field is linear, new frequencies are not generated. Therefore, a nonlinear medium is necessary for optical-frequency mixing. One kind of interaction between

the medium and the optical field is the absorption of a photon by the medium at one frequency, followed by some relaxation process and subsequent emission of a photon at a lower frequency. This process is used in the optical pumping of lasers and is effectively optical frequency conversion, but it is not the kind of coherent process considered in this work. The nonlinear-optical processes used here involve off-resonance interactions of optical fields with frequencies within the transparency range of the medium, where absorption of light is negligible. In this case, the optical field polarizes the medium, causing the electric dipoles of the medium to oscillate at the same frequency as that of the driving field. In many media, this oscillation is not perfectly harmonic, such that a small fraction of the energy of the oscillators is at frequency components different from the driving frequency. This anharmonic part of the oscillation leads to the generation of an optical field at these new frequency components. While some photons of the driving field are destroyed in the process to provide energy for the creation of photons at the new frequencies, this process does not involve absorption, conserves the field energy and can occur on a femtosecond time scale.

The propagation of light in optical media is governed by Maxwell's equations:

$$\nabla \times \tilde{\mathbf{E}} = -\frac{\partial \tilde{\mathbf{B}}}{\partial t} \quad (1.1)$$

$$\nabla \times \tilde{\mathbf{H}} = \tilde{\mathbf{J}} - \frac{\partial \tilde{\mathbf{D}}}{\partial t} \quad (1.2)$$

$$\nabla \cdot \tilde{\mathbf{D}} = \rho \quad (1.3)$$

$$\nabla \cdot \tilde{\mathbf{B}} = 0, \quad (1.4)$$

where  $\tilde{\mathbf{E}}$  is the electric field,  $\tilde{\mathbf{D}}$  is the displacement vector,  $\tilde{\mathbf{B}}$  is the magnetic flux density,  $\tilde{\mathbf{H}}$  is the magnetic field vector,  $\tilde{\mathbf{J}}$  is the free-current density, and  $\rho$  is the the free charge density. Vector quantities are denoted by boldface type and tildes appear over time-dependent variables.

The electric and magnetic properties of the medium play a role through the constitutive relations given below in MKS units:

$$\tilde{\mathbf{D}} = \epsilon_0 \epsilon_r \tilde{\mathbf{E}} + \tilde{\mathbf{P}}_{NL} \quad (1.5)$$

$$\tilde{\mathbf{B}} = \mu_0 \mu_r \tilde{\mathbf{H}} = \mu_0 \tilde{\mathbf{H}} \quad (1.6)$$

We will only consider nonmagnetic media, setting  $\mu_r$  to 1 in Eq. 1.6, accordingly. The nonlinear polarization  $\tilde{\mathbf{P}}_{NL}$  in Eq. 1.5 consists of the quadratic and higher order terms of the expansion in the electric field of the induced dipole moment in the medium:

$$P_{NLi} = \epsilon_0(\chi_{ijk}^{(2)}E_jE_k + \chi_{ijkl}^{(3)}E_jE_kE_l + \dots) \quad (1.7)$$

where summation over repeating indices is assumed. This dissertation is restricted to consideration of only second-order nonlinear optics (three-wave mixing processes). For all the material systems and applications considered in subsequent chapters, the third-order and higher terms in the expansion 1.7 are negligible compared to the quadratic term. Therefore, the symbol  $P_{NL}$  will be used to denote:

$$P_{NLi} = \epsilon_0\chi_{ijk}^{(2)}E_jE_k \quad (1.8)$$

Let the optical field impinging on the medium consist of two frequency components at frequencies  $\omega_1$  and  $\omega_2$ . Then, considering all permutations of indices in 1.8, the nonlinear polarization will contain frequency components at  $2\omega_1$ ,  $2\omega_2$ ,  $\omega_1 \pm \omega_2$  and DC. The corresponding frequency-conversion processes are second harmonic generation, sum and frequency mixing, and optical rectification. In order for efficient energy transfer to a newly generated optical frequency to occur, the nonlinear oscillations of all dipoles along the medium need to be properly phased to ensure constructive interference of the emitted optical waves. This leads to the requirement of phasematching.

### 1.2.2 Quasi-phasematching

Consider three-wave mixing in a uniform nonlinear medium. One way to ensure that energy is transferred efficiently to a new optical frequency is to use a medium without dispersion, such that the phase velocity of light at all frequencies involved in the mixing process are identical. In the case of second harmonic generation, for example, there is a driving field at a frequency  $\omega$  generating linear polarization at a frequency  $\omega$  and nonlinear polarization at  $2\omega$ . All oscillators along the propagation direction are locked in phase by the driving field. The fixed phase-difference between two oscillators separated in space along the propagation direction is determined by the product of the frequency of the oscillators and the time it takes for the driving field to travel between them. This time equals the ratio of the propagation distance and the phase velocity of light in the medium at the frequency of the driving field.

Thus, the phase difference between the dipole oscillations at frequency  $\omega$  is  $\omega\Delta zn_\omega/c = k_\omega\Delta z$ , where  $k_\omega = \omega n_\omega/c$  is the magnitude of the k-vector at the frequency of the driving field, and  $\Delta z$  is the distance between the two dipoles. Accordingly, the phase difference between the nonlinear oscillations at  $2\omega$  is  $(2\omega)\Delta zn_\omega/c \equiv 2k_\omega\Delta z$ . The field at the second harmonic  $2\omega$  generated by the first nonlinear oscillator accumulates a phase of  $k_{2\omega}\Delta z \equiv (2\omega n_{2\omega}/c)\Delta z$  while traveling to reach the second oscillator. If  $n_{2\omega} = n_\omega$ , then this phase exactly compensates the phase difference of the nonlinear dipole oscillations and the fields at  $2\omega$  generated by the two oscillators interfere constructively along the propagation direction leading to quadratic growth of the second harmonic power with propagation distance in the medium (curve (a) on Fig. 1.1). Otherwise, there is a phase mismatch of  $(k_{2\omega} - 2k_\omega)\Delta z$  which leads to oscillations of the power in the second harmonic (curve (b) on Fig. 1.1). The maximum second harmonic power in this case is limited to the power generated over an interaction distance equal to the so called coherence length:

$$L_c = \frac{\pi}{\Delta k} \equiv \frac{\pi}{k_{2\omega} - 2k_\omega} \equiv \frac{\lambda_\omega}{4(n_{2\omega} - n_\omega)} \quad (1.9)$$

where  $\Delta k$  is the k-vector mismatch and  $\lambda_\omega$  is the fundamental wavelength. It is clear from 1.9 that the coherence length is the distance over which the phase mismatch becomes equal to  $\pi$ .

The coherence length in most nonlinear media is very small. For instance, in lithium niobate the coherence length for second harmonic generation of 532-nm green light is only 6.5  $\mu\text{m}$ . Such a small interaction length is usually not adequate for efficient energy transfer to the new frequency component. Therefore, for efficient nonlinear mixing, phasematching is necessary. One solution to the problem of phasematching was proposed by Bloembergen and coworkers in 1962[1]. The method is called quasi-phasematching (QPM) and relies on resetting of the phase mismatch to 0 every coherence length. After one coherence length of propagation, the phase mismatch becomes  $\pi$ . If the sign of the nonlinear susceptibility  $\chi^{(2)}$  is changed at that location, an additional  $\pi$  phase shift is added to the nonlinear polarization (see Eqn. 1.8), resetting the phase mismatch to 0. After another coherence length of propagation, another  $\pi$  of phase shift is accumulated and the sign of the nonlinear coefficient has to be changed again in order to reset the mismatch to 0. In such way, the power in the second harmonic field is allowed to grow along the crystal quasi-quadratically (curve (c) on Fig. 1.1).

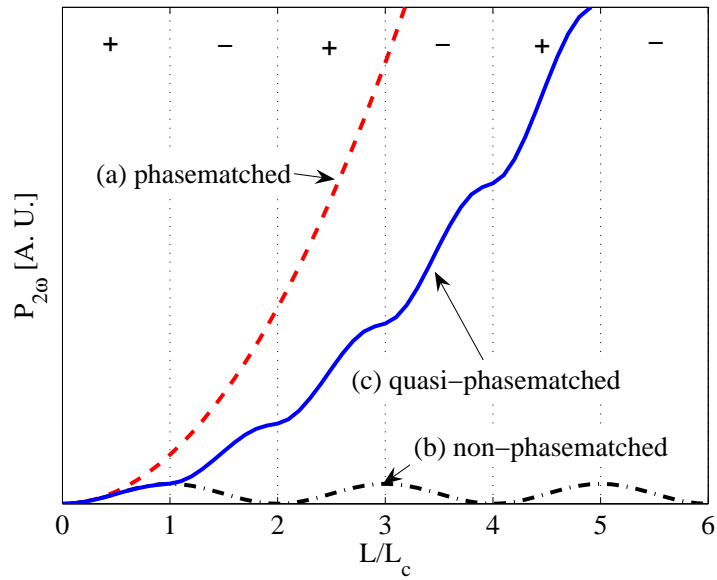


Figure 1.1: SHG output power versus distance  $L$  normalized to the coherence length  $L_c$ . (a) Quadratic growth in the case of phasematched SHG. (b) Oscillatory behavior in the non-phasematched case. (c) Quasi-quadratic growth in the case of first-order quasi-phasematched SHG using periodic sign reversal of the nonlinear susceptibility.

In uniaxial ferroelectric crystals such as lithium niobate, the sign of the nonlinear susceptibility is fixed with respect to the polar axis. Therefore, periodic sign reversal of the nonlinear susceptibility can be obtained by periodic reversal of the polar axis (periodic poling) along the propagation direction. The resulting periodic pattern of the nonlinear susceptibility is often referred to as a ‘‘QPM grating’’ with period  $\Lambda_g$ . With periodic poling, the QPM grating has the functional form of a square wave in space. In the spatial Fourier domain, this square wave can have frequency components at all harmonics of the fundamental grating k-vector  $2\pi/\Lambda_g$ :

$$K_m = \frac{2\pi m}{\Lambda_g} \quad (1.10)$$

Phasematching can be viewed in the spatial Fourier domain as k-vector conservation. In the process of optical-frequency mixing, photons are created and destroyed. For instance, in the case of second harmonic generation, two photons at the fundamental frequency  $\omega$  are destroyed for the creation of each second harmonic photon at frequency  $2\omega$ . If  $2\mathbf{k}_\omega = \mathbf{k}_{2\omega}$ , then the k-vector is conserved and the process is phasematched. If the k-vector is not conserved, then the process is not phasematched and the mentioned oscillations of the second harmonic power occur, limiting the energy conversion. Quasi-phasematching is represented in the Fourier domain as the elimination of k-vector mismatch by including the grating k-vector in the vector sum. Example k-vector diagrams for the cases of perfectly phasematched, non-phasematched and quasi-phasematched SHG are shown on Fig. 1.2. As can be seen on Fig. 1.2 (c), any harmonic  $K_m$  of the fundamental grating k-vector can be used for quasi-phasematching. Because the Fourier-series expansion coefficient of the  $m^{\text{th}}$  harmonic of a square wave is  $2/(m\pi)$ , the effective nonlinear coefficient of the medium for quasiphase-matched optical frequency mixing is[2]:

$$\chi_{eff}^{(2)} = \frac{2}{m\pi} \chi^{(2)} \quad (1.11)$$

Therefore, for strongest nonlinear mixing, it is desirable to use first-order quasi-phasematching ( $m = 1$ ).

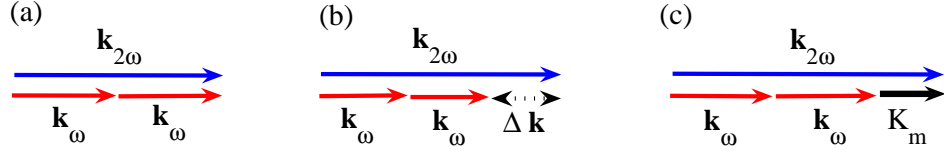


Figure 1.2: Phasematching represented by  $k$ -vector diagrams in Fourier space. (a) Phase-matched SHG. (b) Non-phasematched SHG with  $k$ -vector mismatch  $\Delta k$ . (c) Quasi-phasematched SHG with QPM order  $m$ .

### 1.2.3 Efficiency of nonlinear optical frequency mixing

Phasematching allows the accumulation of the local effects of optical frequency mixing along the volume of the dielectric medium exposed to intense optical fields. From Eq. 1.8 it can be seen that the strength of the local nonlinear response increases linearly with the intensity of the optical field. The commonly used way to obtain high intensity is to use pulsed lasers (Q-switched or mode-locked). For efficient continuous-wave optical-frequency mixing, the two ways to increase intensity are to use cavity enhancement of the field (e.g., in pump-resonant second harmonic or difference-frequency generation, optical parametric oscillation) or tight focusing of the input laser beam. In the case of SHG without depletion of the fundamental field, the efficiency of power conversion in a plane-wave interaction is given by the expression [2]:

$$\eta^{SHG} = \frac{P_{2\omega}}{P_{\omega}} = \frac{8\pi^2 d_{eff}^2}{n_{2\omega} n_{\omega}^2 c \epsilon_0 \lambda_{\omega}^2} \frac{P_{\omega} L^2}{A_{eff}} \text{sinc}^2 \left( \frac{\Delta k L}{2} \right) \quad (1.12)$$

where  $d_{eff}$  is the effective nonlinear coefficient equal to  $\chi_{eff}/2$ ,  $A_{eff}$  is the effective beam area for the interaction,  $L$  is the interaction length,  $\Delta k$  is the wave-vector mismatch and  $P_{\omega}$  is the optical power at frequency  $\omega$ . The above expression, a good approximation for  $\eta \leq 0.2$ , demonstrates that the SHG efficiency increases linearly with the pump intensity (which is proportional to  $P_{\omega}/A_{eff}$ ) and quadratically with the interaction length  $L$ . With limited fundamental power, the efficiency can be increased by increasing  $L$  or reducing  $A_{eff}$ . The former leads to a reduction of the bandwidth available for phasematching due to the  $\text{sinc}^2$  term in 1.12. Since the efficiency increases quadratically with  $L$ , while the phasematching

bandwidth decreases only linearly, in many cases a large interaction length is desirable. Occasionally, though, the bandwidth requirement of certain devices sets an upper limit on  $L$ . Reducing  $A_{eff}$ , on the other hand, increases efficiency without a bandwidth penalty. This is why, in bulk crystals, efficiency is increased by properly focusing the beam such that its transverse dimensions are kept as small as possible throughout the length of the crystal. The optimum focusing for a gaussian beam in the case of SHG occurs when the length of the crystal equals 2.84 times the beam confocal parameter[3].

Performing the optical-frequency mixing in a waveguide allows the combination of a small  $A_{eff}$  with a large interaction length. The interaction length  $L$  can be set independently of the effective area by adjusting the waveguide length. In the case of a quasi-phasematched interaction,  $L$  is the length of the periodically poled part of the waveguide. The effective area is determined by the mode overlap[2]:

$$A_{eff} = \left\| \int \int \hat{d}(x, y) \hat{E}_\omega^2(x, y) \hat{E}_{2\omega}(x, y) dx dy \right\|^{-2} \quad (1.13)$$

where the waveguide modal fields are normalized according to

$$\int \int \hat{E}^2(x, y) dx dy = 1 \quad (1.14)$$

and

$$\hat{d}(x, y) = \frac{d(x, y)}{d_{eff}} \quad (1.15)$$

where  $d(x, y)$  is the transverse distribution of the effective nonlinear coefficient, which may vary across the waveguide. From equation 1.14 it follows that the normalized modal fields  $\hat{E}_\omega$  and  $\hat{E}_{2\omega}$  are large when the transverse size of the mode is small. It is clear from 1.13 that the effective area is minimized when the peaks of the field distributions of the modes at the different interacting frequencies are spatially aligned with each other (and with the region of high nonlinear coefficient if the latter is not constant across the waveguide).

### 1.3 Photorefractive damage and damage-resistant QPM materials

Some ferroelectric materials such as  $\text{LiNbO}_3$  and  $\text{LiTaO}_3$  have the rare combination of a high second-order nonlinear coefficient, a wide transparency range spanning from the mid-infrared to the near-ultraviolet, and a possibility for periodic poling allowing for flexibility in the design and fabrication of devices for optical-frequency mixing using QPM. A great number of experimental demonstrations of practical devices have been published. Several examples can be found in the following references: [2, 4, 5, 6, 7, 8, 9, 10, 11, 12, 13, 14, 15, 16, 17, 18, 19, 20, 21, 22, 23, 24, 25, 26, 27, 28, 29, 30, 31, 32, 33, 34, 35, 36]. Many of the demonstrations involve the propagation of intense visible or ultraviolet light in the ferroelectric crystal and cannot be used in practical applications unless the problem of photorefractive damage (PRD), which severely limits their lifetime or maximum power, is solved. The photorefractive effect is a result of the combination of two phenomena: the absorption of light by crystal defects leading to the formation of a space-charge field by the generated photocarriers and the subsequent modulation of the refractive index of the medium by this space-charge field via the electro-optic effect [37, 38, 39, 40, 41]. In standard optical-quality  $\text{LiNbO}_3$  (LN) and  $\text{LiTaO}_3$  (LT) the dominant photorefractive effect is of the photogalvanic (photovoltaic) type, where the space-charge field is formed due to a photogalvanic current generated by the crystal defects upon illumination and absorption [38]. For the same photogalvanic current, crystals with higher electrical conductivity would exhibit smaller photorefractive effects due to a reduction of the space-charge field. The standard congruent lithium niobate (CLN) and lithium tantalate (CLT) have a composition determined by the point in the phase diagram where the liquid phase and the single-crystal  $\text{LiNbO}_3(\text{LiTaO}_3)$  phase with the same composition are in equilibrium at the temperature of crystal growth ( $\sim 1250$  °C for CLN). For these crystals, the equilibrium occurs at a Li-poor composition (the ratio  $x_{\text{Li}} = [\text{Li}] / ([\text{Li}] + [\text{Nb,LT}])$  is  $\sim 0.484$ , rather than the stoichiometric value  $x_{\text{Li}} = 0.5$ ). The excess of Nb(Ta) ions leads to the formation of Nb(Ta) antisites - Nb(Ta) ions located at lithium lattice sites and represented by the symbol  $\text{Nb}_{\text{Li}}(\text{Ta}_{\text{Li}})$ . These antisites act as relatively deep traps for electrons [38, 42, 43], significantly reducing their mobility. As a consequence, CLN and CLT exhibit a very low conductivity and prominent photorefractive effects. In both  $\text{LiNbO}_3$  [44, 45, 46, 47, 43] and  $\text{LiTaO}_3$  [48, 49, 50], some combination of doping with a suitable ion and changing of

the crystal composition toward stoichiometric can help reduce photorefractive damage to levels that cause no problems for practical applications. Examples on the two extremes in composition include 5 mol-% MgO:doped congruent  $\text{LiNbO}_3$  (5%MgCLN)[44, 45], non-doped  $\text{K}_2\text{O}$ -flux grown near-stoichiometric  $\text{LiNbO}_3$  [51, 52], near-stoichiometric  $\text{LiTaO}_3$  prepared by the double-crucible Czochralski growth (DCCG) [53] and near-stoichiometric vapor-transport equilibrated  $\text{LiTaO}_3$  (VLT)[49]. Examples of a combined approach are 1 mol-% near-stoichiometric  $\text{LiNbO}_3$  and  $\text{LiTaO}_3$  produced by top-seeded solution growth (TSSG) or DCCG [54].

Direct growth of PRD-resistant  $\text{LiNbO}_3$  and  $\text{LiTaO}_3$  is difficult both for congruent crystals with doping above the threshold for PRD-suppression (e.g., 5 mol-% MgO for  $\text{LiNbO}_3$ ) [55] and for near-stoichiometric crystals with or without doping. On the other hand, congruent crystals with small amounts of doping (below the PRD-suppression threshold) are relatively easy to grow. The method of vapor-transport equilibration (VTE) developed for lithium niobate in the last quarter of the past century [56, 57, 58, 59, 60, 61] allows to enrich in lithium the composition of originally congruent crystals via indiffusion of lithium from  $\text{Li}_2\text{O}$  vapor. VTE is a relatively easy to implement self-terminating process, producing a homogeneous single-phase crystal with composition corresponding to the phase-boundary between a single-phase monocrystal and a two-phase lithium-rich polycrystal. The combination of VTE and a moderate MgO-doping of the congruent precursor crystal allows flexibility in the choice of final crystal composition and related properties while avoiding the difficulties of direct growth of off-congruent or heavily doped crystals.

Most of the crystal properties relevant in periodic poling (coercive field, conductivity, domain nucleation density) vary significantly with crystal composition in both  $\text{LiNbO}_3$  and  $\text{LiTaO}_3$ . For example, the coercive field changes linearly with deviation from stoichiometric composition [62] from about 21 kV/mm in congruent crystals ( $\text{Li}/[\text{Li}+(\text{Nb,Ta})]\approx 0.484$ ) to less than 50 V/mm in VTE- $\text{LiTaO}_3$ . Gopalan et al.[62] proposed that the large coercive field in congruent crystals is due to the need to reorient electric dipoles formed by the lithium vacancies and niobium antisites associated with the lithium deficiency. In stoichiometric crystals such defects are eliminated and the coercive field is more than two orders of magnitude smaller than in congruent crystals.

In non-doped crystals, the electric field necessary to initiate the poling of z-cut wafers by domain nucleation is comparable to and somewhat higher than the field necessary for

the domain to grow laterally in the x-y plane by domain-wall movement in the x- crystallographic direction(s). In 5 mol-% MgO:LiNbO<sub>3</sub> the electric field necessary for observing domain inversion (switching) at room temperature varies between 4.5 and 7 kV/mm [63] for switching times ranging from about 150 to a few seconds. These values of the switching field are smaller than the field necessary for domain inversion in congruent non-doped crystals, but much larger than the field necessary for stoichiometric crystals, which is in the range of a few tens to a few hundred V/mm[51, 49]. Even though the MgO-doping eliminates the vast majority of Nb antisites, the switching field is only 4-5 times smaller than that for the non-doped congruent crystal. On the other hand, the domain-wall velocity in this material is appreciable (of order 1  $\mu\text{m}/\text{sec}$ , appropriate to pole at a period of a few microns over time span of a few seconds) at a field of only 2 kV/mm[64]. At 4.5 kV/mm, the domain wall velocity is several hundred  $\mu\text{m}/\text{sec}$ . Over the characteristic poling time of  $10^2$  s at this electric field, a domain that started at the beginning of the poling would grow to many mm in size, much larger than the required period of several microns. The reason for this discrepancy between the necessary field for poling and the field necessary for appreciable domain expansion via domain wall motion is that the nucleation site density for domain formation at room temperature is very low in 5 mol-% MgO:LiNbO<sub>3</sub>. Because of this problem, short-pitch periodic poling of 5 mol-% MgO:LiNbO<sub>3</sub> is challenging and requires the use of means for nucleation enhancement such as high poling temperature combined with metal electrodes[65, 66], “two-dimensional” field application [67, 68] or corona-discharge poling [69]. Without these means for nucleation enhancement, the inverted domains tend to merge at short periods ( $< 10\mu\text{m}$ ), preventing the transfer of the electrode pattern to a periodic domain pattern. At longer periods, there are significant fluctuations in the domain width along the beam propagation direction, causing significant reduction in the conversion efficiency (for effects of irregularity of the domain width on conversion efficiency, see Ref. [70]).

The more basic methods for electric-field periodic poling of z-cut wafers rely on applying voltage between a patterned periodic electrode deposited on one z-face of the wafer and a uniform electrode contacted on the other z-face[71, 72, 73]. For first-order QPM of SHG of visible light (yellow and green), domain patterns with periods ranging from 6 to 10  $\mu\text{m}$  are needed. In this range of periods, domain reversal of non-doped congruent or near-stoichiometric LiNbO<sub>3</sub> or LiTaO<sub>3</sub> involves only a single-step-patterned hard-baked photoresist on the +z face to serve as a periodic dielectric mask under a covering liquid

electrode (LiCl dissolved in water). This domain reversal method can be applied to 5 mol-% MgO:LiNbO<sub>3</sub>, but to achieve the 6-10- $\mu$ m periodicity, some additional steps (e.g. combining patterning of metal electrodes, high temperature poling and short poling voltage pulses)[66] have to be included in the fabrication process. As will be demonstrated later in the dissertation, combining light MgO-doping with VTE allows the elimination of PRD in crystals with doping levels as small as 0.3 mol-% [74]. Such crystals can be periodically poled by adding only two modifications to the conventional technique used for non-doped crystals: performing the hard-bake of the photoresist at a lower temperature for longer time, and using pulsed poling voltage [75]. Both modifications are easy to implement. This process for periodic poling is not only simpler compared to that for the 5 mol-% crystals, but can also be advantageous for waveguide devices. The quality of the periodic pattern is usually better near the surface on which the electrode was patterned, so for high mixing efficiency and better device reproducibility it is desirable that waveguides be fabricated on that surface. Avoiding metal deposition keeps the surface pristine for waveguide fabrication and helps circumvent issues with absorption, photorefractive damage or scattering loss (even after the metal is removed by chemical etching) that commonly occur in waveguides fabricated on the same surface where metal electrodes have been used.

Another advantage of near-stoichiometric crystals over congruent or 5%MgO-doped ones is their higher thermal conductivity[76, 77]. Assuming equal absorption, crystals with higher thermal conductivity can handle higher laser power because of better heat dissipation. In addition, the UV absorption edge of SLN is several nm shorter than that of 5 mol-% MgO:LiNbO<sub>3</sub>.

## 1.4 Overview

The first goal of this dissertation is to provide tools for accurate modeling of the fabrication process of optical-frequency mixers based on proton-exchanged PPLN waveguides, including devices that efficiently generate mid-infrared radiation. The second major goal is to provide an attractive solution for the problems of photorefractive damage and green-induced infrared absorption (GRIIRA) in LiNbO<sub>3</sub>.

Chapter 2 lists the main formulae that describe optical frequency mixing in waveguides and then describes a new complete model for the fabrication and properties of annealed (APE) and reverse (RPE) proton exchanged waveguides in congruent lithium niobate (CLN).

The model includes the properties of proton diffusion in CLN, and the dispersion of the proton-exchanged material, providing the means for the reconstruction of the waveguide refractive index profile. This information is adequate to allow the accurate modelling of the mode field distributions and propagation constants by numerical solution of the wave equation.

Chapter 3 describes recent results on mid-infrared generation in the region 3100-4000 nm by difference-frequency mixing in RPE waveguides including the design, fabrication and characterization of the mixing devices. In addition, the same difference-frequency mixing process is used to demonstrate over 40 dB of parametric amplification of narrow-spectrum 1570-nm signal by using microsecond-long pump pulses at 1064 nm.

Chapter 4 starts with the description of the accepted model of the photorefractive effect in  $\text{LiNbO}_3$  due to Glass et al.[38]. This provides the basis for understanding the control of photorefractive sensitivity by varying stoichiometry and doping. The subsequent sections describe the development and characterization of vapor transport equilibrated near-stoichiometric lithium niobate with significantly reduced MgO-doping concentration (VTEMgLN) compared to 5 mol-% MgO: $\text{LiNbO}_3$ . The resistance of VTEMgLN to PRD and GRIIRA is demonstrated.

Chapter 5 describes the development of a fabrication process for high quality periodic poling of VTEMgLN. A detailed physical picture of the poling process is discussed that allows the parameters most relevant to the domain patterning of MgO-doped material to be identified. Experimental results from measurements of some of the parameters are included. The appropriate modifications to the traditional fabrication procedures are then described along with experimental results on periodic poling featuring high-quality patterns for periods down to 8  $\mu\text{m}$  suitable for first-order QPM of SHG of 575-nm and longer-wavelength radiation and good-quality patterns at 7  $\mu\text{m}$  for SHG of 532-nm radiation. Finally, experimental demonstration of room-temperature stable SHG of up to 3 W at 532 nm in 0.3 mol-% VTEMgLN is described.

Chapter 6 concludes the dissertation.

## Chapter 2

# Model for anneal proton-exchanged waveguides in congruent lithium niobate

The purpose of this chapter is to introduce an accurate model for the fabrication of annealed proton-exchanged waveguides and reverse proton-exchanged waveguides in standard optical-quality congruent lithium niobate. This model can be used to predict the linear optical properties of the waveguide, which determine the phasematching and affect the efficiency of optical-frequency mixing. In addition, accurate predictions of the linear optical properties allow the modeling of the optical performance of more sophisticated integrated devices that may contain tapers, frequency mixing regions, directional couplers, Y-junctions, and segmented waveguide sections. The described model has proven very useful in the design of a variety of devices for optical signal processing and mid-infrared generation over the four years since its development.

### 2.1 Three-wave mixing in an optical waveguide

The theory of optical-frequency mixing in waveguides using the second-order nonlinear polarization is described in [78, 2]. The main definitions and results for mixing of single modes are listed below briefly with detail adequate to provide background for the rest of the chapter. The description of reference [2] is closely followed.

The longitudinal components of the electric and magnetic field in the waveguide can be expressed in terms of the transverse components. The transverse components can be written as a superposition of propagation modes:

$$\mathbf{E}_t(x, y, z) = \sum_{\nu} A_{\nu}(z) e^{-i\beta_{\nu}z} \gamma \hat{E}_{\nu}(x, y) \quad (2.1)$$

$$\mathbf{H}_t(x, y, z) = \sum_{\nu} B_{\nu}(z) e^{-i\beta_{\nu}z} \zeta \hat{H}_{\nu}(x, y) \quad (2.2)$$

where

$$\gamma = \sqrt{\frac{2}{Nc\epsilon_0}}, \quad \zeta(x, y) = \sqrt{2Nc\epsilon_0} \quad (2.3)$$

The quantities  $A_{\nu}(z)$  and  $B_{\nu}(z)$  are the slowly varying amplitudes for the electric and the magnetic field, respectively, for mode  $\nu$  with propagation constant  $\beta_{\nu}$ .  $\hat{E}_{\nu}(x, y)$  and  $\hat{H}_{\nu}(x, y)$  are field modes normalized according to 1.14:

$$\iint \hat{E}^2(x, y) dx dy = 1 \quad (2.4)$$

$$\iint \hat{H}^2(x, y) dx dy = 1 \quad (2.5)$$

Assuming optical fields in the medium exist or are generated at frequencies  $\omega_1$ ,  $\omega_2$  and  $\omega_3$  with  $\omega_3 = \omega_1 + \omega_2$ , the nonlinear polarization at these three frequencies is given by:

$$\mathbf{P}(\omega_1) = \epsilon_0 2d \mathbf{E}(\omega_3) \mathbf{E}^*(\omega_2) \quad (2.6)$$

$$\mathbf{P}(\omega_2) = \epsilon_0 2d \mathbf{E}(\omega_3) \mathbf{E}^*(\omega_1) \quad (2.7)$$

$$\mathbf{P}(\omega_3) = \epsilon_0 2d \mathbf{E}(\omega_1) \mathbf{E}(\omega_2) \quad (2.8)$$

The nonlinear coefficient is constant along the waveguide axis but is allowed to vary in the transverse directions:

$$d(x, y, z) = d_{eff} \hat{d}(x, y) \quad (2.9)$$

where  $d_{eff}$  is the effective nonlinear coefficient obtained by projecting the material nonlinear coefficient tensor onto the proper axes of the interacting fields.

For single-mode interactions, the sums in 2.4 each contain only one term. We can then

use the index  $i=1,2,3$  to label fields at frequencies  $\omega_1$ ,  $\omega_2$  and  $\omega_3$ . The slowly varying amplitudes of these fields obey the following set of coupled equations:

$$\frac{dA_1}{dz} = \kappa_1 \theta^* A_3 A_2^* e^{-i\Delta\beta z} - \frac{\alpha_1}{2} A_1 \quad (2.10)$$

$$\frac{dA_2}{dz} = \kappa_2 \theta^* A_3 A_1^* e^{-i\Delta\beta z} - \frac{\alpha_2}{2} A_2 \quad (2.11)$$

$$\frac{dA_3}{dz} = \kappa_3 \theta A_1 A_2 e^{i\Delta\beta z} - \frac{\alpha_3}{2} A_3 \quad (2.12)$$

The constants  $\kappa_j$  are defined as

$$\kappa_j = -i \sqrt{\frac{2\omega_j^2 d_{eff}^2}{N_1 N_2 N_3 c^3 \epsilon_0}} = -i \sqrt{\frac{8\pi^2 d_{eff}^2}{N_1 N_2 N_3 c \epsilon_0 \lambda_j^2}} \quad (2.13)$$

where  $N_1$ ,  $N_2$  and  $N_3$  are capitalized to signify effective mode indices. The quantity  $\Delta\beta$  in the exponent is the phase mismatch defined by

$$\Delta\beta = \beta_3 - \beta_2 - \beta_1 = 2\pi \left( \frac{N_3}{\lambda_3} - \frac{N_2}{\lambda_2} - \frac{N_1}{\lambda_1} \right) \quad (2.14)$$

The strength of the coupling is controlled by the overlap integral  $\theta$  given by the expression

$$\theta = \int_{-\infty}^{\infty} dx \int_{-\infty}^{\infty} dy \hat{d}(x, y) \hat{E}_1(x, y) \hat{E}_2(x, y) \hat{E}_3^*(x, y) \quad (2.15)$$

The effective area defined in Eq. 1.13 equals the inverse square of the overlap integral ( $A_{eff} = |\theta|^{-2}$ ).

Several solutions of the coupled equations 2.10 under different assumptions are listed below and used in discussions in the following sections of the chapter as well as following chapters. The examples of lossless waveguides ( $\alpha_1 = \alpha_2 = \alpha_3 = 0$ ) are considered first. In the case of sum-frequency generation (SFG) under the approximation of undepleted driving fields  $A_1$  and  $A_2$ , assuming the initial condition  $A_3(0) = 0$ , the power at the sum-frequency  $\omega_3$  after interaction over a length  $L$  is given by

$$P_3(L) = \eta_{mor} P_1(0) P_2(0) L^2 \text{sinc}^2 \left( \frac{\Delta\beta L}{2} \right) \quad (2.16)$$

where  $\eta_{nor}$  [%/Wcm<sup>2</sup>] is the normalized conversion efficiency given by the expression

$$\eta_{nor} = \kappa_3^2 |\theta|^2 = \frac{8\pi^2 d_{eff}^2}{N_1 N_2 N_3 c \epsilon_0 \lambda_3^2} \left| \int_{-\infty}^{\infty} dx \int_{-\infty}^{\infty} dy \hat{d}(x, y) \hat{E}_1(x, y) \hat{E}_2(x, y) \hat{E}_3^*(x, y) \right|^2 \quad (2.17)$$

For the case of second harmonic generation (SHG), the nonlinear polarization at the second harmonic frequency is given by  $\mathbf{P}_{2\omega} = \epsilon_0 d \mathbf{E}_\omega^2$ , making the normalized efficiency four times smaller than the normalized efficiency for SFG. The expressions for SHG power and normalized efficiency are:

$$P_{2\omega}(L) = \eta_{nor}^{SHG} P_\omega^2(0) L^2 \text{sinc}^2 \left( \frac{\Delta\beta L}{2} \right) \quad (2.18)$$

$$\eta_{nor}^{SHG} = \frac{2\pi^2 d_{eff}^2}{N_\omega^2 N_{2\omega} c \epsilon_0 \lambda_{2\omega}^2} |\theta|^2 \equiv \frac{8\pi^2 d_{eff}^2}{N_\omega^2 N_{2\omega} c \epsilon_0 \lambda_\omega^2} |\theta|^2 \quad (2.19)$$

In this case, in the expression 2.15 for  $\theta$ , the indices 1 and 2 refer to the fundamental frequency  $\omega$ , while the index 3 refers to the SH frequency  $2\omega$ .

For the case of difference-frequency mixing (DFM), several different approximations can be considered depending on whether the pump is depleted or not, and whether the focus is on the newly generated frequency or on the amplification of the input signal. Assuming an undepleted pump ( $A_3 = \text{const}$  along the waveguide) and negligible amplification of the input signal ( $A_1 = \text{const}$  along the waveguide), the following expression is obtained for difference-frequency generation (DFG):

$$P_3^{DFG}(L) = \eta_{nor}^{DFG} P_3(0) P_1(0) L^2 \text{sinc}^2 \left( \frac{\Delta\beta L}{2} \right) \quad (2.20)$$

with

$$\eta_{nor}^{DFG} = \kappa_2^2 |\theta|^2 = \frac{8\pi^2 d_{eff}^2}{N_1 N_2 N_3 c \epsilon_0 \lambda_{DFG}^2} |\theta|^2 \quad (2.21)$$

Difference-frequency mixing can also be used for parametric amplification. To describe this case in traditional terms, the index 3 is replaced by  $p$  (pump), 1 is replaced by  $s$  (signal) and 2 is replaced by  $idler$ . The signal is allowed to vary, while the pump is considered undepleted for the simplest solution. Assuming  $A_{idler}(0) = 0$ , the solution is [5]

$$A_p(L) = A_p(0) \quad (2.22)$$

$$A_s(L) = A_s(0)\cosh(gL) \quad (2.23)$$

$$A_{idler}(L) = i\sqrt{\frac{\lambda_s}{\lambda_{idler}} \frac{\sqrt{\eta_{nor}P_p}}{g}} e^{-\frac{\Delta\beta L}{2}} A_s^*(0)\sinh(gL) \quad (2.24)$$

where the gain coefficient is

$$g = \sqrt{\eta_{nor}P_p - \left(\frac{\Delta\beta}{2}\right)^2} \quad (2.25)$$

and the normalized efficiency is defined as

$$\eta_{nor} = \frac{8\pi^2 d_{eff}^2}{N_s N_{idler} N_p c \epsilon_0 \lambda_s \lambda_{idler}} |\theta|^2 \quad (2.26)$$

The power of the amplified signal is

$$P_s(L) = P_s(0)\cosh^2(gL) \quad (2.27)$$

In the high-gain regime,  $\cosh(gL) \approx 0.5e^{gL}$ , and the expression for the gain in dB can be given analytically:

$$Gain[dB] = 10\log_{10} \frac{P_s(L)}{P_s(0)} \approx 4.34gL - 3 \quad (2.28)$$

In the presence of propagation losses, the external conversion efficiency is reduced. In the case of DFG in the small-conversion regime without phase-mismatch, a useful estimate of conversion efficiency for practical purposes is given by[79, 5, 80]:

$$\eta_{lossy}^* \equiv \frac{P_{DFG}^{out}}{P_p^{in} P_s^{in}} = e^{-(\alpha_p + \alpha_s)} \frac{(e^{\Delta\alpha L} - 1)^2}{(\Delta\alpha L)^2} \eta_{nor}^{DFG} L^2 \quad (2.29)$$

where  $P^{out}$  stands for power on the waveguide output just before exit,  $P^{in}$  stands for power coupled into the waveguide input just after entrance, and  $\alpha$  denotes the power loss coefficient in  $\text{cm}^{-1}$ . The labels  $p$ ,  $s$ , and  $DFG$  stand for “pump”, “signal” and “generated DFG” (idler), respectively. The coefficient  $\Delta\alpha$  characterizes the difference in losses between the generating and the generated waves:  $\Delta\alpha = (\alpha_p + \alpha_s - \alpha_{DFG})/2$ , where  $\alpha_{DFG}$  is the power power loss coefficient at the DFG output wavelength.

For device characterization in the laboratory, it is more straightforward to use the following efficiency indicator that is measured directly after accounting for output reflections:

$$\eta_{lossy} \equiv \frac{P_{DFG}^{out}}{P_p^{out} P_s^{out}} = \frac{(e^{\Delta\alpha L} - 1)^2}{(\Delta\alpha L)^2} \eta_{nor}^{DFG} L^2 \quad (2.30)$$

## 2.2 History of proton-exchanged waveguides

Fabrication of proton-exchanged waveguides in lithium niobate was first reported by Jackel et al.[81]. The waveguides were obtained by immersion in hot molten benzoic acid (BA) which served as a proton source. Since then, several weak organic acids have been used[82, 83, 84] as proton sources with similar results. In addition, phosphoric acid[85, 86, 87], water[88], glycerol[89, 90], a solution of  $\text{KHSO}_4$  in glycerol[91, 92, 93, 89], and a solution of  $\text{KHSO}_4$  in a mixture of anhydrous sulphate salts[83] have been used as immersion proton sources. More recently, benzoic acid vapor was used as a proton source at higher temperature[94, 95, 96, 97, 98].

Most waveguides in the early days of proton exchange (PE) were fabricated using BA at temperatures below 249 °C to avoid boiling of the acid. Waveguides prepared this way had a step-like refractive index profile[81] with index increase  $\Delta n \approx 0.12 - 0.14$  and are characterized by instability of the profile[99] and suppressed electro-optic[100, 101, 102] and second-order nonlinear[103, 104, 105] coefficients. The thickness of the step-index layer increased linearly with the square root of time and could be described with the use of an effective diffusion coefficient. Jackel and Rice[99] demonstrated a significant reduction of the effective diffusion coefficient by buffering the BA melt with 3-3.5 mole % lithium benzoate (LB). This kind of buffered exchange produced waveguides that were much more stable and with a somewhat smaller  $\Delta n$  (e.g., 0.11 instead of 0.13). Buffering with 4 mole % led to an abrupt decrease of  $\Delta n$  below 0.3 paralleled by a decrease in the effective diffusion coefficient by an order of magnitude compared to the 3.4- mole % buffered melt and 3 orders of magnitude compared to unbuffered BA. A PE process with 4 mole % LB would be too slow for practical device fabrication. In 1988, Suchoski et al.[106] reported the development of stable annealed proton exchange (APE) channel waveguides with significantly lower losses than PE waveguides and no significant degradation of the electro-optic coefficient. The APE waveguides were fabricated by adding a high-temperature diffusion step (annealing in air, 350 °C, 2-4 hours) after the PE in BA. The APE waveguides had a smaller surface  $\Delta n$

than regular PE waveguides. Loni et al.[107] published an extensive characterization of the effects of buffered melts and annealing on the properties of the waveguides. Bortz et al.[108] performed a depth profiling of the  $d_{33}$  nonlinear coefficient in APE waveguides and determined that at depths beyond the initial PE layer the nonlinearity was almost the same as that of the substrate, while within the PE layer it remained significantly smaller, although a slow recovery was observed with very long annealing. Due to their simple fabrication, stability, and good nonlinear and electro-optic properties, APE waveguides became the platform for the fabrication of a wide variety of integrated-optics devices. Many applications of optical frequency mixing for telecommunications systems were implemented using APE waveguides. The SHG conversion efficiency of these devices for 1.55- $\mu\text{m}$  pump wavelengths reached around 40%/Wcm<sup>2</sup>, so that a 5-cm-long device had an overall efficiency near 1000 %/W, or, in more appropriate units for optical communication systems, 1%/mW. Such devices could be used for -10 dB wavelength conversion using DFG with 10 mW of pump coupled in the waveguide (actually, about twice as much pump power is typically needed on the input in order to compensate for coupling and propagation losses at the pump and the signal).

One limitation of APE waveguides is the asymmetry in depth of their refractive index profile. Due to their surface fabrication, the diffusion is inherently asymmetric and results in profiles that look like a half-bell shape. Since the modes at the shorter wavelengths are smaller, their peak is closer to the surface than is that of the modes at longer wavelengths, leading to sub-optimal mode overlap (see Eq. 1.13 and subsequent discussion). In addition, the mode-field distribution is asymmetric in depth which sets the lower limit in coupling loss to an optical fiber with a symmetric mode. These problems of APE waveguides were addressed by the development of reverse proton exchanged (RPE) buried waveguides. The first RPE waveguides were fabricated by reverse exchange (back-substitution of Li<sup>+</sup> for H<sup>+</sup> in H<sub>x</sub>Li<sub>1-x</sub>NbO<sub>3</sub>) following PE without an annealing step in between[109, 110, 111, 112]. These RPE waveguides were not very useful for nonlinear optics because the guiding was mostly in a region which was part of the original PE waveguide, where the nonlinear coefficient was diminished by the proton exchange. The first study of RPE performed on APE waveguides was published by Korkishko et al.[113], demonstrating planar RPE waveguides in LiNbO<sub>3</sub> and LiTaO<sub>3</sub> and discussing their advantage for coupling into optical fiber in terms of more symmetric mode shapes. Based on this work Parameswaran et al.[24] developed buried channel waveguides by APE followed by RPE. These waveguides

featured SHG mixing efficiency three times higher than channel APE waveguides and a very symmetric mode profile. The most efficient proton exchange waveguides to date, with efficiency of 3.1%/mW have been fabricated by the RPE method.

Some studies focused on understanding the reasons for the formation of the dead layer and developing methods for proton exchange that avoid dead layer generation. These methods were based on using low-acidity melts (e.g., buffered acids) or vapor-phase proton exchange in combination with higher exchange temperature (usually 300-400 °C). Veng et al.[92] developed dilute melt(DM) PE using  $\text{KHSO}_4$  in glycerol buffered with lithium benzoate at 230 °C and succeeded in direct fabrication of PE waveguides with various magnitudes of the surface index increase ranging from 0.01 to 0.12. They measured the nonlinear properties of the waveguides and showed that PE waveguides with  $\Delta n \leq 0.013$  have  $\chi^{(2)}$  values of at least 90% of the original  $\text{LiNbO}_3$  value while waveguides with higher  $\Delta n$  had strongly reduced susceptibility. A subsequent publication [93] described the fabrication method in detail and showed that the fabrication of these lower- $\Delta n$  waveguides required very long exchange times. Even for relatively shallow single-mode waveguides the fabrication time ranged from 120 to 336 hours. El Hadi et al.[114] demonstrated DM PE at 300 °C using a sealed ampule with benzoic acid and lithium benzoate. Using 2.6 % LB they fabricated DM PE waveguides with  $\Delta n \leq 0.015$  that had essentially preserved nonlinear susceptibility while waveguides obtained with 1 % LB had  $\Delta n \approx 0.105 - 0.11$  and nonlinear SHG signal less than 5 % of that of the substrate. By performing etching studies on periodically poled APE waveguides, they demonstrated that the high- $\Delta n$  PE erased the periodic domain structure. Korkishko et al.[83, 115] developed a method of high-temperature PE using a melt of stearic acid buffered with lithium stearate (LS) for temperatures in the range 300-370 °C, making use of the higher boiling point of stearic acid ( $\approx 380$  °C). At these higher temperatures high-quality nonlinear waveguides can be fabricated over convenient time intervals of a few hours.

An alternative way of making high-quality PE waveguides at high temperature is by using vapor-phase proton exchange (VPE)[94, 116, 95, 96, 98, 97]. It has been reported that the VPE method allows the fabrication of waveguides with high  $\Delta n \approx 0.1$ , low propagation losses, undegraded nonlinear optical properties[94, 95] and higher resistance to photorefractive damage than APE waveguides[96]. All demonstrations of VPE so far have used benzoic acid as the vapor source and have utilized a sealed ampule in order to perform the exchange process at temperatures higher than the BA boiling point of 249 °C. Only

planar waveguides with confinement in one dimension have been demonstrated so far in the literature. Results on fabrication of low-loss channel waveguides with good non-linear properties have not been published yet. Solving the technical challenges of uniform exchange along the waveguide may determine in the future the choice of high-temperature PE between VPE and dilute-melt PE.

### 2.3 Phase diagram of PE $\text{LiNbO}_3$

As described in the previous section, the properties of the waveguide layer vary significantly depending on the proton source and fabrication temperature. This is due to a multitude of crystalline phases of the compound  $\text{H}_x\text{Li}_{1-x}\text{NbO}_3$ . Rice [117] reported the following phases in proton-exchanged powders:  $\alpha$  phase for  $x < 0.12$ ,  $\beta$  phase for  $0.56 < x < 0.7$ , and the phase mixtures  $\alpha + \beta$  for  $0.12 < x < 0.56$  and  $\beta + \text{HNbO}_3$  for  $0.7 < x < 1$ . The different crystalline phases are distinguished by their different x-ray diffraction patterns. The  $\alpha$ -phase has the same crystal structure as the pure  $\text{LiNbO}_3$  crystal. Ganshin and Korkishko [118] found that the stresses of planar waveguides fabricated on x- and y-cut substrates lead to slightly biaxial waveguides while waveguides on a z-cut wafer are uniaxial like the substrate. Fedorov and Korkishko [119] discovered that the strains in a proton exchanged monocrystal lead to a phase diagram different from that in powders. A comparison between the equilibrium (powder), and the stressed phase diagrams can be found in [120]. It is determined that the mixed-phase regions  $\alpha + \beta$  and  $\beta + \text{HNbO}_3$  of the equilibrium phase diagram are replaced by several single-crystalline phases in the phase diagram for monocrystals. The following sequence of crystalline phases appears in order of increasing proton concentration:  $\alpha$  for  $x < 0.12$ ,  $\kappa_1$  for  $0.12 < x < 0.34$ ,  $\kappa_2$  for  $0.34 < x < 0.44$ ,  $\beta_1$  for  $0.44 < x < 0.52$ ,  $\beta_2$  and  $\beta_3$  for  $0.52 < x < 0.64$ , and  $\beta_4$  for  $x > 0.64$ . In addition, on y-cut substrates the phase  $\beta_4$  is replaced by a (monoclinic)  $\eta$  phase in the region  $x > 0.64$ . The phase boundaries between the regions described above are somewhat loosely defined because they vary slightly with substrate orientation and temperature due to changing stress conditions.

The most often used dependence of  $\Delta n$  on the replacement ratio  $x$  has been determined by Korkishko and Fedorov [120]. A copy of the corresponding diagram is shown in Fig. 2.1 for the extraordinary (TM) and ordinary (TE) polarized light in PE and APE waveguides on z-cut substrates. This dissertation considers only waveguides fabricated at temperatures

under 350 °C which follow the low-temperature (LT) branch of the  $\Delta n_e(x)$  dependence.

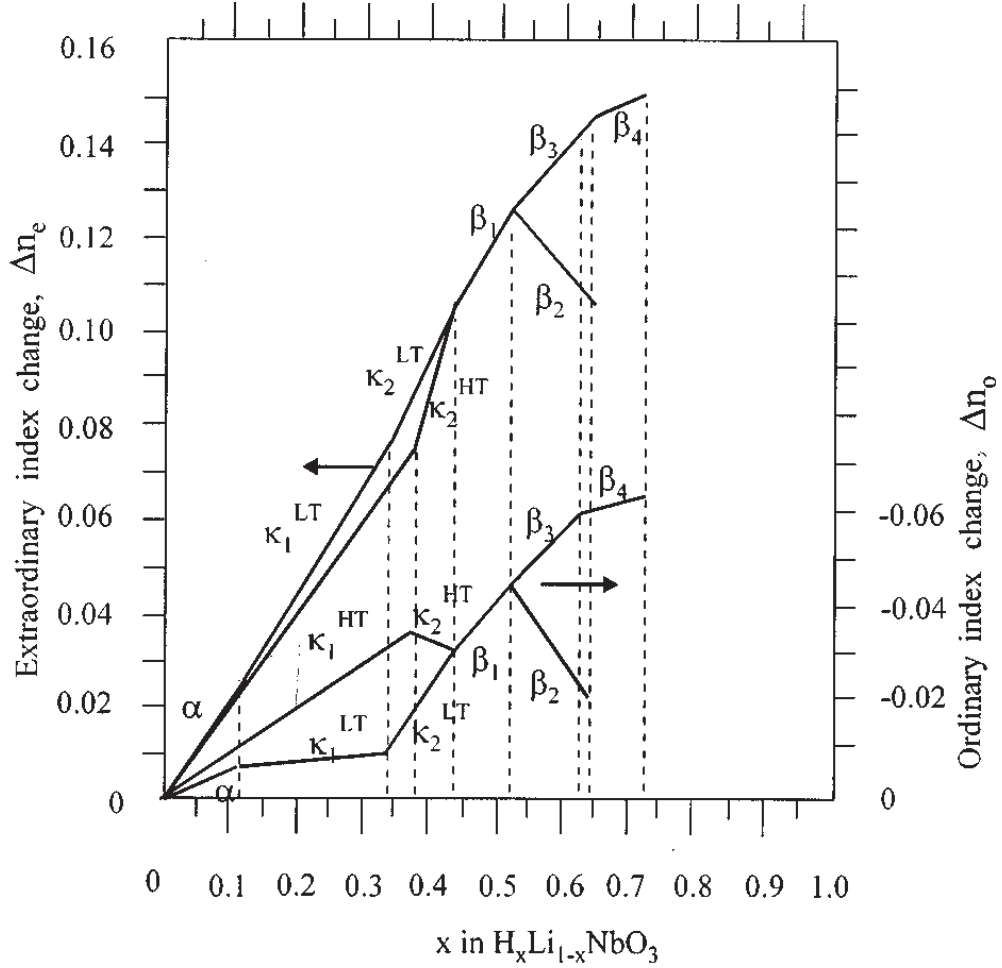


Figure 2.1: Dependence of  $\Delta n_e$  at 633 nm on replacement ratio  $x$  in  $H_xLi_{1-x}NbO_3$ . LT stands for “low temperature” and HT stands for “high temperature”, signifying waveguides annealed below and above 350 °C, respectively.

Besides the existence of multiple phases of  $H_xLi_{1-x}NbO_3$ , the following features of the diagram have relevance for subsequent discussions in this thesis:

- (i) For  $0.105 \leq \Delta n_e \leq 0.125$ , the waveguide can be in any mixture of the  $\beta_1$  and  $\beta_2$  phases, such that measurement of the refractive index alone is not adequate to predict  $x$  accurately.
- (ii) For the LT branch of the  $\Delta n_e(x)$ -dependence, the region  $0 \leq x \leq 0.44$  ( $0 \leq \Delta n_e \leq$

0.105) can be approximated with a single straight line without introducing significant error. Further justification for the adoption of this approximation will be given later.

## 2.4 Previous models of annealed proton-exchanged waveguides

Since the discovery of PE waveguides in 1982[81] and of APE waveguides in 1988[106] several studies of the low-temperature PE process [121, 122, 85, 82, 123, 87] and of the high-temperature annealing process [124, 107, 125, 126, 127, 128, 129, 130, 115, 131] have been published. Most models that were constructed were focused on slab waveguides. Of these, the ones by Veng and Skettrup[129] and Korkishko et al.[130, 115] are most recent and take into account the detailed knowledge of crystal structure that was developed during the 1990's. These models also acknowledge the strong concentration dependence of the effective diffusion coefficient that describes the high-temperature annealing. The only complete model for fabrication of channel APE waveguides including proton diffusion during high-temperature annealing, relationship between proton concentration and refractive index, dispersion of the refractive index and nonlinear optical properties of the waveguides was published by Bortz and Fejer in 1991[126]. This very successful model was used for over a decade in the design of many APE-waveguide devices. Recently (2001), some difficulties surfaced when using model for the design and fabrication of optical integrated circuits combining several components[132]. A more accurate fabrication model was needed. Very recently, a comprehensive methodology for design fabrication of APE waveguides was published[131], but it does not include any data on the dispersion of proton exchanged lithium niobate and lacks precision, since it assumes linear diffusion during high-temperature annealing, which is a poor approximation.

The main weakness of the model [126] is that it fails to incorporate some details of the early stages of annealing and does not deal with the instability of PE waveguides. At the time of development of that model, the detailed crystalline structure and multiple phases of  $H_xLi_{1-x}NbO_3$  had not been yet discovered. The new model described in this chapter addresses the mentioned inadequacies and allows the achievement of good repeatability and higher accuracy in the fabrication of waveguide devices. In addition, the new model includes a more accurate Sellmeier equation that describes the dispersion of  $H_xLi_{1-x}NbO_3$  in most of the transparency range of the material, namely, from 0.45 to 4  $\mu\text{m}$ .

## 2.5 Waveguide characterization techniques

Two optical techniques were used to characterize planar waveguide samples relevant to the development of the model – waveguide-mode spectrum measurement via prism coupling and total proton dose estimate via absorption measurements. The same techniques are used subsequently for process control during channel waveguide fabrication.

### 2.5.1 Refractive-index-profile measurements using prism coupling

A relatively simple nondestructive technique for obtaining the refractive index profile of a planar waveguide is the measurement of the spectrum of guided modes (dark m-line spectroscopy) followed by some procedure that can recover the refractive index distribution from the set of effective mode indices. In the case of a planar isotropic waveguides or pure TE-modes in a planar waveguide, if the relevant refractive index profile is a rectangular step, then the inversion problem has an exact solution if two or mode guided modes exist[133]. This allows the determination of the index and thickness of a uniform (e.g. step-index) waveguide from the effective indices of two or more modes. If more than two modes are guided and the profile is approximately uniform, then a separate estimate of the index and thickness can be made from each pair of modes. Performing statistics on the multiple results for index and thickness allows the assignment of average values to the waveguide parameters and the use of the corresponding standard deviations to estimate approximately how much the profile differs from that of a uniform waveguide. When extra care is taken to make the measurements using a consistent coupling procedure, the product of  $\Delta n$  and the waveguide thickness can be measured with a precision of 0.25-0.5%, depending on the waveguide thickness.

For monotonic graded-index guides, the inverse Wentzel-Kramers-Brillouin (IWKB) procedure [134, 135, 136, 137, 138] produces a good approximation to the actual refractive index profile, especially if the number of guided modes is greater than four. For profiles with steep sections of  $\Delta n(z)$ , more modes may be necessary.

The effective index of each mode depends on the depth distribution of the modal field. If a half-bell-shaped graded index profile (typical of APE waveguides) is considered, modes that propagate mostly in the steeper region of the profile are more widely spaced in effective index than are modes propagating mainly in the less steep tail or top of the profile. In addition, modes are more densely spaced in effective index in thick waveguides than in

thin waveguides simply because thicker waveguides support more modes for the same index increase. The dense mode spacing in the tail of a thick diffused APE waveguide sets a limit on the ability to resolve modes using the prism coupling method when the mode spacing becomes smaller than the characteristic width of the coupling resonance. Deeply diffused waveguides (tail of the profile longer than about 10  $\mu\text{m}$ ) produce an m-line spectrum in  $n_{eff}$ -space consisting of several well defined dark m-lines (corresponding to guided modes with effective indices well above the substrate index) and a region of continuous coupling corresponding to modes with effective indices very close to the substrate index (modes that propagate mainly in the lower index tail of the waveguide profile). For instance, for a well-annealed APE waveguide measured at 633 nm, the continuous coupling region can occupy the range from the substrate index of 2.2025 to 2.2045. On the intensity scan of the prism coupler this effect often has the appearance as if the substrate index were higher than its actual value. Published articles on APE waveguides have not mentioned this effect and have not taken it into account in estimates of the dependence of  $\Delta n_e$  on proton concentration. Performing multiple annealing steps on the same waveguide increases the fraction of protons diffused deep into the substrate. In integrating the area under the IWKB profile, only the part of the refractive index profile ranging from the maximum (surface) index to the effective index of the last detected separate mode is taken into account. This leads to disregarding the portion of the index profile where the modes that occupy the continuous-coupling region of the m-line spectrum propagate. Consequently, assuming a linear relationship between  $\Delta n_e$  and proton concentration, the area under the IWKB profile would decrease with diffusion of the profile deeper into the substrate. If all modes in the tail of the profile could be detected, then the area of the IWKB-profiles would not change with annealing (proton diffusion) in the case where  $\Delta n_e$  is linear with concentration throughout the considered range of concentrations. Because of this effect of continuous coupling of modes propagating in the deepest part of the waveguide, it is not possible, by using prism coupling alone, to distinguish between a linear relationship  $\Delta n(x)$  and a case where a slight (10-15%) deviation from the linear relationship is present. In the model described in this chapter, it is assumed that  $\Delta n_e \propto x$  throughout the range  $0 \leq x \leq 0.44$ . The prism-coupling measurements in this dissertation have been performed using a Metricon 2010 system and the included software for index/thickness estimations according to Ref. [133] and IWKB calculations according to Ref. [136]. Some mode spectra are not possible to fit with the polynomial fit used in [136]. For profiles with such mode spectra, other IWKB procedures have been used [134, 135, 138].

### 2.5.2 Absorption spectroscopy of the OH stretching vibration

Protons incorporated in the LiNbO<sub>3</sub> crystal form OH groups with oxygen ions from the lattice. Even though protons enter the crystal through ion exchange for lithium, the preferred positions for the protons are not the Li lattice sites, but certain locations in or near the oxygen planes[139, 140]. Therefore, in the phases without excessively high proton concentrations (e.g.,  $\alpha$ ,  $\kappa_1$ ,  $\kappa_2$  and pure  $\beta_1$ ), all the protons sit in or very near the oxygen planes and so do the OH bonds. The stretching mode of these bonds leads to strong absorption of light at 2.86  $\mu\text{m}$  polarized parallel to the oxygen planes. Since the oxygen planes are perpendicular to the ferroelectric crystal axis (the  $z$ -axis), the OH stretching vibration leads to absorption of the ordinary wave. The area of the absorption profile is proportional to the integral of the depth-distribution of protons in the substrate:

$$A = \int d\lambda \int_0^t dz \alpha(z, \lambda) \propto \int_0^t C(z) dz \quad (2.31)$$

where  $\alpha$  is the absorption coefficient,  $\lambda$  is the wavelength,  $z$  is the integration variable along the ferroelectric axis,  $t$  is the thickness of the crystal along the same axis and  $C$  is the proton concentration which may be normalized for convenience. Thus a measurement of the absorption peak around 2.86  $\mu\text{m}$  provides means for estimating the total number of protons in the crystal. In order to measure the number of protons in the waveguide, the crystal is first measured before proton exchange and the number of protons estimated for this virgin crystal is later subtracted from the total number of protons measured in the proton-exchanged crystal. Note that for an accurate proton estimate it is preferable that the crystal not contain any of the phases with higher concentration of protons than the  $\beta_1$  phase since these phases exhibit an additional broad unpolarized peak centered near 3.1  $\mu\text{m}$ [139, 99], which would require a separate calibration. With a proper calibration (described in the appendix) and a quiet light source, the total number of protons in the waveguide can be measured with a precision of 0.5-1%. This typically requires a 1.5-hour warm-up of the spectrophotometer lamp, which is a standard practice. The absorption measurements in this dissertation have been performed using a Hitachi 4001 spectrophotometer.

## 2.6 Model for high-temperature proton diffusion

### 2.6.1 Soft anneal

PE waveguides fabricated by immersion in pure BA melt at temperatures around 200 °C have a surface  $\Delta n_e(633nm) \approx 0.13-0.14$ , with higher values obtained at lower temperatures and vice versa. The actual concentration profile of such waveguides is not exactly a step, but closer to a trapezoid, such that the line  $\Delta n_e(z)$  is slanted in the high-index region (Fig. 2.2).

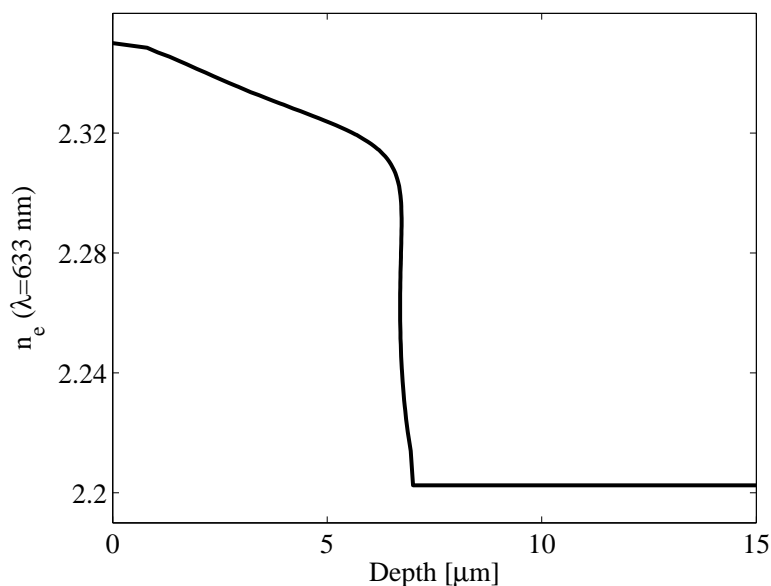


Figure 2.2: Approximate refractive index profile of a waveguide fabricated by vapor-phase proton exchange from  $\text{KHSO}_4$  vapor on a  $z$ -cut substrate. The profile was recovered from the spectrum of TM-mode effective indices using the IWKB procedure due to Chiang[136]. Similar profiles are obtained by immersion in molten unbuffered BA below 200 °C.

It is clear that PE waveguides like the one in Fig.2.2 have  $\beta_3$ -phase  $\text{H}_x\text{Li}_{1-x}\text{NbO}_3$  near the surface and some combination of the  $\beta_2$  and  $\beta_1$  phases underneath the  $\beta_3$  phase. The relative ratio of different phases depends strongly on the composition of the proton source (e.g., fresh benzoic acid melt versus benzoic acid that has been used for PE), on the exchange temperature, and on the depth of the waveguide (shallower waveguides may not form the  $\beta_3$  phase at all, and may have less  $\beta_2$  phase than deeper waveguides). In addition, due to stress and dependence of the phase boundaries on temperature that has not been well

characterized, such multi-phase waveguides are quite unstable and change with time[99]. It would be complicated and inefficient to try to use such a PE waveguide as an initial condition for modeling of the next step (high-temperature diffusion near 300-350 °C) in the fabrication process for APE waveguides. This obstacle is overcome by performing a soft anneal (SA). The waveguide after SA is in a single phase and more stable than a regular PE waveguide.

The idea of SA is to form a waveguide that is in a single crystalline phase, is more stable than a regular PE waveguide, and has a refractive index profile which is rectangular rather than trapezoidal like in Fig.2.2. By observing the early stages of the high-temperature annealing (the first 0-120 minutes at 330 °C) of a slab waveguide, it was found that the proton exchange layer increased very quickly in depth within the first 30 minutes and changed much more slowly after that. During these first 30 minutes the temperature of the sample had not yet reached 330 °C because of the thermal mass of the annealing boat. A similar behavior of fast increase of the waveguide depth with annealing that practically self-terminated was described previously[120] and it was concluded that the expansion led to a uniform waveguide with composition corresponding to the  $\kappa_2$ - $\beta_1$  phase boundary. The study reported in this section is aimed at characterizing this expansion process and using it to design a procedure (soft anneal) that produces a waveguide that can serve as an accurate and reliable initial condition for high-temperature diffusion modeling.

The SA process step is performed on a slab waveguide which may be a “witness” sample that accompanies a channel waveguide device (designed for some application) through all other steps of the fabrication process. After finishing the immersion proton exchange, the sample is cleaned of benzoic acid and heated to a temperature around 210 °C for several hours (this is the SA step). During SA, the protons diffuse deeper into the substrate while maintaining a step-like shape of the concentration profile. The slope at the top of the trapezoidal profile decreases by an order of magnitude, so the profile can be approximated much better with a rectangular step. In addition, the very high concentration phases ( $\beta_2, \beta_3, \beta_4$ ) disappear, because the deepening of the waveguide leads to a reduction of the concentration. The deepening process self-terminates once the crystal structure and proton concentration in the waveguide correspond to the phase boundary between the  $\kappa_2$  and the  $\beta_1$  phase. In such a waveguide all the protons can be accounted for by the OH absorption measurement near 2.86  $\mu\text{m}$  or by the index/thickness calculation [133] from the mode spectrum in the step-profile approximation. The reason why the deepening of the waveguide self-terminates

is that at temperatures around 210 °C the diffusivity of protons in any of the  $\beta$  phases is at least two orders of magnitude higher than the diffusivity in the  $\alpha$ ,  $\kappa_1$  or  $\kappa_2$  phases. It should be pointed out that the effective activation energy for diffusion in the  $\alpha$  phase is around 1.4 eV, while in the  $\beta$  phases it is around 1 eV. This means that with lowering the temperature, the difference in diffusivities grows even larger, so there is an advantage in performing the SA at lower temperature. The temperature range around 210 °C is convenient for one-day soft-annealing of waveguides with PE depths of 1–1.5  $\mu\text{m}$ . Typically, for waveguides proton exchanged in unbuffered BA at temperatures below 200 °C, the waveguide thickness increases during SA between 1.6 and 1.5 times depending on the state of the acid (fresh or multiple-use). The area under the refractive index profile increases by 25-30% during SA.

The choice of SA time and temperature is determined by the depth of the waveguide. Because the process is practically self-terminating, the time needs to be determined only approximately. If the expected depth of the SA waveguide is 1  $\mu\text{m}$ , then the appropriate SA is 10 hours at 212 °C. Since the SA is a diffusion process, for other SA-depths  $d_{SA}$  the time in hours at 212 °C scales as  $10d_{SA}^2$  where  $d_{SA}$  is measured in microns. If a different temperature is used, the ratio of diffusion coefficients is given by the Arrhenius law:

$$\frac{D(T_2)}{D(T_1)} = \exp\left(\frac{E_a}{kT_1} - \frac{E_a}{kT_2}\right) \quad (2.32)$$

where  $T$  stands for Kelvin temperature,  $E_a \approx 1$  eV is the activation energy in the  $\beta_1$  phase, and  $k = 8.617 \times 10^{-5}$  eV/K is the Boltzmann constant.

The evolution of the refractive index profile during SA was studied by performing multiple SA steps on a waveguide proton-exchanged in molten benzoic acid. The acid had been used for other exchanges earlier, such that the formed initial PE waveguide had an average index increase around 0.13 at 633 nm. The waveguide had been stored at room temperature for some months and its  $\Delta n_e$  had decreased to about 0.123. Eight annealing steps were performed. The times, temperatures and results from index/thickness measurements [133] at 633 nm using prism coupling are summarized in Table 2.1. The effective times at 202 °C were calculated using equation 2.32.

The area under the refractive index profile was approximated by the product of the exchange-layer thickness  $d$  and  $\Delta n_e$ . Figure 2.3 shows the evolution of the proton exchanged layer with effective soft-anneal time. Column 0 represents aging at room temperature. The thin continuous horizontal line indicates the location of the  $\kappa_2$ – $\beta_1$  phase boundary according

SA No.	0	1	2	3	4	5	6	7	8
$t$ [h]	$\sim 10^3$	5	5	5	5	10.5	10.5	10.5	12.9
$T$ [°C]	23	202	202	202	202	202	212	222	222
$t_{eff}$	$\sim 10^{-3}$	5	5	5	5	10.5	17.4	28.2	34.6
$\Delta n$	0.1230	0.1121	0.1082	0.1063	0.1048	0.1033	0.1031	0.1019	0.1006
$d$ [ $\mu m$ ]	0.884	1.260	1.329	1.362	1.383	1.404	1.404	1.417	1.427

Table 2.1: Time  $t$ , temperatures  $T$ , thickness  $d$  and  $\Delta n_e$  measurements from SA study

to Korkishko [120].

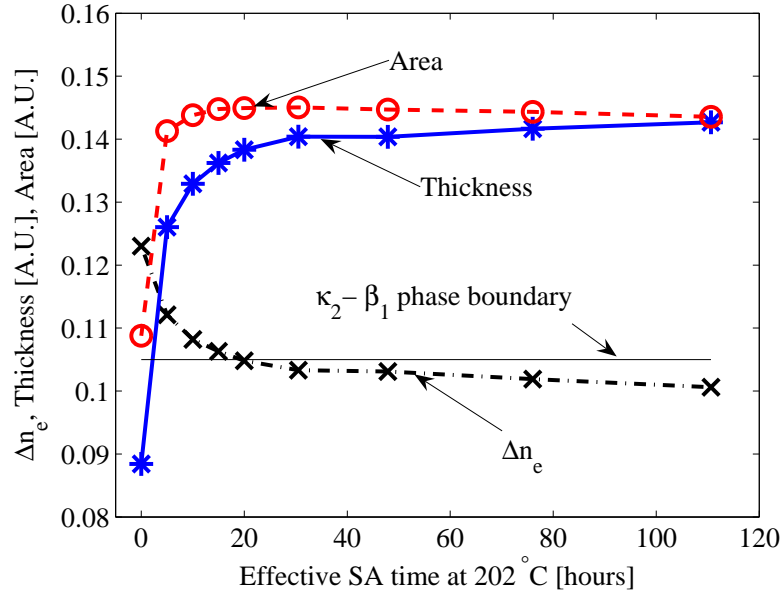


Figure 2.3: Evolution of the  $\Delta n$ , the SA PE layer thickness and their product (the area) with effective SA time at 202 °C.

It is evident that the thickness  $d$  of the layer increases monotonically with SA time, with a very steep increase in the beginning. The index step  $\Delta n_e$  decreases monotonically, with a steep decline in the beginning. The area  $\Delta n_e d$  increases by about 30 % in the beginning, then stays constant while  $\Delta n_e$  slowly decreases from 0.105 to 0.103, and then starts to decline very slowly. This decline for  $t > 40$  h is due to a small number of protons at the boundary between the protonated region and the pure substrate leaking into the substrate via diffusion in the  $\alpha$  crystalline phase. The approximation of a rectangular profile combined with the limited number of modes cannot account for these protons which form a small tail

at the deep end of the index profile. The flat portion of the area curve extends from 20 to 40 hours and  $\Delta n$  between 0.105 and 0.103. This index change corresponds to the waveguide entering the  $\kappa_2$  phase. The flat portion of the area curve is the target of the soft anneal because it is the condition in which all protons can be accounted for by a simple step-profile approximation with high precision. It is clear that to perform the soft anneal properly, one needs to estimate the necessary SA time only approximately.

The long-term stability of the SA waveguides was measured on three samples soft-annealed at 212 °C to different final proton concentrations. The results of measurements performed on three waveguides over a period of 3000 hours are plotted on figure 2.4.

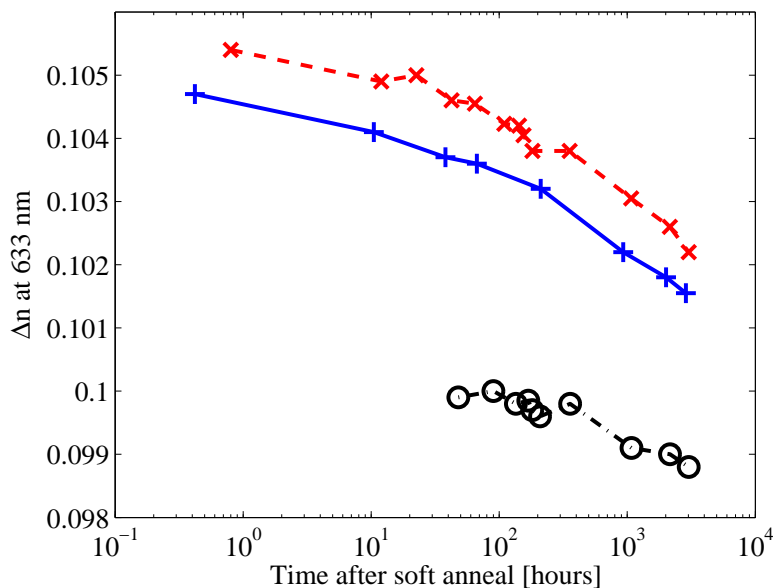


Figure 2.4: Long-term evolution of the  $\Delta n$  of waveguides soft-annealed at 212 °C to different final proton concentrations.

The thickness estimate is not plotted since the thickness was determined to be constant to within the measurement/estimate error of 0.003  $\mu\text{m}$  or  $\sim 0.2\%$ . It is clear that the SA waveguides in the figure are unstable. In addition, the lowest of the three curves is parallel to the other two which means that continuing the SA to lower  $\Delta n_e$  below 0.103 does not improve stability any further. This suggests that the evolution of the refractive index after SA is most likely due to slow release of stress that was generated between the waveguide and the substrate during the fast cooling from 212 °C to room temperature.

More recently, it was found that simply turning off the furnace at the end of the SA at 212 °C and letting it cool to room temperature in about 20 hours with a decay time constant of  $\approx 6$  hours produced SA waveguides that were stable (measurements performed in consecutive days produced the same  $\Delta n_e$ ). This measurement was done only on waveguides with  $\Delta n_e \leq 0.105$ . Multiple soft anneals using this procedure of slow cooling at the end were performed on a PE waveguide. The dependence of the area  $\Delta n_e d$  on the layer index after each such SA is plotted on figure 2.5.

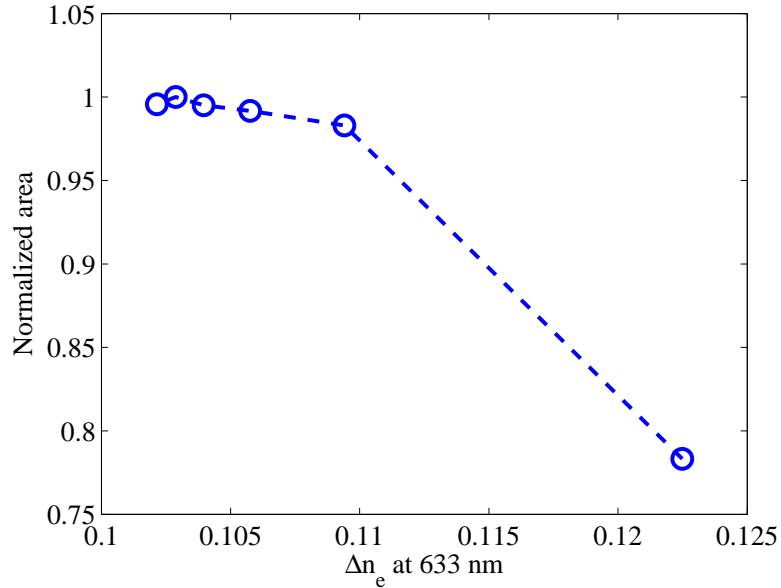


Figure 2.5: Area  $\Delta n_e d$  as a function of waveguide layer index increase  $\Delta n_e$  for a waveguide after multiple soft anneals each with slow cooling at the end

It can be seen that for the case of SA with slow cooling at the end, the maximum area occurs for  $\Delta n_e \approx 0.1025$ . Comparison with figure 2.4 shows that the slow cooling at the end of the SA is equivalent to about 1000 hours of aging of the SA waveguide at room temperature.

It was also determined that lower concentration APE waveguides containing  $\kappa_1$  or  $\kappa_1$  and  $\kappa_2$  besides the underlying  $\alpha$  phase, were also unstable if cooled quickly after the annealing at high temperature (300-350 °C). Placing them in a furnace at 140 °C and turning the furnace off to allow it to cool to  $\approx 30$  °C over a period of 15 hours with a decay time constant of  $\approx 6$  hours rendered the waveguides with  $\Delta n_e$  decreased by 2-2.5% and stable. Performing

a second identical decay from 140 °C to room temperature did not change the waveguides further.

The new findings about stabilizing SA or APE waveguides were not utilized in the model described in this chapter, but they can be used for future refinements. Instead, in the present version of the model it is assumed that the mode spectra of the planar (slab) waveguide are measured using prism coupling at some point in the time interval between 10 and 20 hours after a soft-anneal or high-temperature anneal with fast cooling. If the prism-coupling measurement is done outside of this time interval, the long-term stability curves from figure 2.4 can be used to correct the profile area estimate. The (unstable) SA waveguide with  $\Delta n_e = 0.105$  is used as the initial condition for the following high-temperature diffusion modeling.

### 2.6.2 Assumptions

The following assumptions have been made in the waveguide model:

1. In the concentration range  $0 \leq x \leq 0.44$  that includes the  $\alpha$ ,  $\kappa_1$  and  $\kappa_2$  crystalline phases the increase in refractive index  $\Delta n_e$  is proportional to  $x$ .
2. The effective diffusivity that describes the ion-exchange high-temperature diffusion process is continuous throughout the region  $0 \leq x \leq 0.44$ . This is consistent with the smooth nature of the experimentally observed IWKB profiles of APE waveguides and makes the numerical problem of diffusion modeling less complicated than in the case with diffusivity jumps across phase boundaries.
3. The effective diffusivity  $D = D(x, T)$  depends only on temperature and proton concentration, but not on the history of any particular region of the crystal that is modelled or on the derivatives of the concentration profile. This approximation probably does not hold very well within the SA layer since even after a very long high-temperature anneal the “dead” layer remains different from the substrate below (has suppressed nonlinear coefficient)[108]. It is likely that due to the generated structural defects in the dead layer, the proton diffusivity in it is higher than in the substrate underneath. Some deviations have been observed between RPE experiments on thick waveguides where the depth of the dead layer is substantial (2.4  $\mu\text{m}$ ) and modeling simulations. The differences suggest that the proton diffusivity inside the dead layer is somewhat larger than what the model assumes to be the diffusivity everywhere in the crystal regardless of local history. This effect of history dependence of the diffusivity has not been studied in detail and is not incorporated in the

model.

4. In the temperature range from 300 °C to 350 °C, which is the temperature range where most practical APE waveguides are annealed, the dependence of the diffusivity on temperature follows a simple Arrhenius law (see equation 2.32).

5. The modes of the APE waveguide on a  $z$ -cut substrate can be well approximated as pure TM modes without the need to consider hybrid modes. The  $e$ -polarized wave in the APE waveguide experiences an increase of the refractive index while the  $o$ -polarized wave experiences a decrease and is not guided. Even the virgin substrate is birefringent. The effective index of an  $e$ -polarized TM-mode even in a slab waveguide does depend slightly on the material ordinary material index  $n_o$  because all TM modes have a small longitudinal component of the electric field. This component is disregarded in the modeling of APE waveguides, which is consistent with an approximation of weak guidance. The SA waveguide with  $x=0.44$  has a relatively large  $\Delta n_e$ . For these waveguides a small correction is made for the estimated waveguide thickness by using the “TE-index” feature provided by the software of the Metricon prism coupling system. When using this feature, one TE index is provided by the operator as an approximation for the TE index in both the waveguide and substrate. In the measurements related to this study, the TE index is the average between the TE index of the substrate (2.2865 at 633 nm) and the TE index of the waveguide (2.2530 at 633 nm).

6. Even though TM modes are considered, the scalar wave equation is solved disregarding the vectorial nature of the optical electric field. The longitudinal component of the field along the waveguide axis is disregarded. This approximation works well for weakly guiding waveguides.

Note that this dissertation considers exclusively waveguides fabricated on  $z$ -cut congruent LiNbO<sub>3</sub> substrates. Waveguides on  $x$ -cut substrates experience different stress conditions and would require a separate model for proton diffusion and  $\Delta n$ . Also, waveguides on MgO-doped or stoichiometric substrates will have different amount of vacancies as well as experience different stress, both of which will change the diffusion properties as well as the refractive index.

### 2.6.3 Concentration-dependent diffusion in one dimension

The high-temperature diffusion (annealing) of the waveguides that converts the step-like concentration profile into a deeper half-bell shape is usually performed at temperatures in

the range 310-340 °C. The SA waveguide with  $\Delta n_e = 0.105$  is used as the initial condition for the diffusion modeling. A normalized concentration  $C$  is assigned for the diffusion simulation such that  $C = 1$  when  $\Delta n_e = 0.105$  at 633 nm. This means that  $C = x/0.12$  in  $H_xLi_{1-x}NbO_3$ . With the normalized concentration defined this way, the initial condition for the diffusion simulation becomes a step profile with  $C = 1$  for  $z < d_{SA}$  and  $C = 0$  for  $z > d_{SA}$  where  $z$  is the depth variable and  $d_{SA}$  is the thickness of the soft annealed waveguide.

To determine the dependence  $D(C)$  of the diffusivity on concentration three planar (slab) waveguide samples with SA depths of 0.965, 1.275, 1.99 and 2.38  $\mu m$  were annealed multiple times at 328 °C. After each annealing, the mode spectrum of each sample was measured at 458 nm with the prism coupler and the IWKB approximation for the refractive index profile calculated and recorded. This shorter wavelength was used in order to provide more modes for better profile recovery. The index profiles were converted to normalized concentration profiles by dividing by  $\Delta n_e(C = 1, \lambda = 0.458\mu m) = 0.135$ . After the data of all annealed profiles on each of the samples was collected, many diffusion simulations were tried with different continuous analytic expressions for  $D(C)$ . Since it is well known that the diffusivity at very low concentration (e.g.,  $C < 0.01$ ) is much higher than at higher concentrations (e.g.,  $0.1 < C < 0.8$ ) [125, 126, 129, 115], nonlinear (concentration-dependent) diffusion models were explored, with functional forms for  $D(C)$  that satisfy this condition. Besides the form  $D(C) = \alpha + (1 - \alpha)e^{-\beta C}$  that was used in [126], rational functions were also tried with the general form

$$D(C) = \alpha + \frac{1 - \alpha}{\beta C^p + \gamma} \quad (2.33)$$

In the above functional forms,  $\alpha$ ,  $\beta$  and  $\gamma$  are parameters that were varied to try to obtain best fits for all data with a single set of parameters. The values  $p=0.5, 1, 1.5$  and  $2$  were tried for the power of  $C$  in the denominator of 2.33. The numerical simulations were performed using the efficient semi-implicit algorithm for nonlinear diffusion by Weickert et al.[141]. The forward-time center-space explicit algorithm[142] was also used on several occasions to confirm the accuracy of the semi-implicit code. The diffused concentration profiles produced by the two codes usually agreed within 0.5%. The diffusion simulation for each sample was performed by inputting the experimental anneal times for that particular sample and letting the diffusion code simulate the diffusion process in small steps and record the concentration

profile whenever the simulated diffusion time equals a particular experimental time.

Of all the trial functional forms, only the following one produced good fits for all concentration profiles:

$$D(C) = D_T \left( \alpha + \frac{1 - \alpha}{\beta C + \gamma} \right) \quad (2.34)$$

with  $D_T=0.721$   $\mu\text{m}/\text{hour}$  at  $328$   $^\circ\text{C}$ ,  $\alpha =0.08$  and  $\beta=35$  and  $\gamma=0.065$ . The comparison between IWKB and diffusion simulation profiles is displayed in figure 2.6. The agreement is very good in the displayed range of waveguide SA depths from  $0.965$  to  $1.99$   $\mu\text{m}$ , especially in the concentration range  $C < 0.7$ . For the high-concentration IWKB profiles, the portion of each profile where  $C > 0.6$ , is not usually very accurate due to a polynomial extrapolation done in this part of the profile during the IWKB procedure. It should be noted that for a waveguide with a soft annealed depth of  $2.4$   $\mu\text{m}$ , the agreement between IWKB and simulation profiles is significantly worse, presumably due to the large dead layer with diffusion properties different from the ones assumed in the model.

The parameter  $\gamma$  controlling the diffusivity at very low concentration could be varied within the range  $0.05 \leq \gamma \leq 0.13$  with acceptably small degradation of the agreement between experimental and simulation profiles at the two ends of the interval. The value of  $\gamma$  was further refined to  $0.065$  by using experiments with reverse proton exchange (RPE) on APE waveguides and comparing them with the predictions of the diffusion model.

The temperature dependence of the diffusivity was determined by annealing several samples at different temperatures ranging from  $300$  to  $360$   $^\circ\text{C}$  and simulating the diffusion using the nonlinear diffusivity, Eq. 2.34, and varying only the temperature-dependent pre-factor  $D_T(T)$ . The experimental results are plotted on figure 2.7. Within the explored temperature range, the data are fitted quite adequately with a single exponential with an activation energy of  $1.39 \pm 0.02$  eV.

The RPE process was implemented by immersion of the APE waveguides in a eutectic mixture of  $\text{LiNO}_3$ ,  $\text{KNO}_3$  and  $\text{NaNO}_3$ [113]. A description of the RPE equipment is available in [143]. In RPE, protons leave the crystal from the waveguide surface, replaced by lithium ions from a suitable source. Unlike the overall diffusion rate of annealing, the rate of RPE (how many protons leave the crystal per unit time) depends very strongly on the diffusivity at very low concentrations, and therefore, on  $\gamma$ . This is because during most of the RPE process, the waveguide is buried beneath a reverse-exchanged layer with few or no protons in it. Every proton that is to be reverse-exchanged by lithium must diffuse through the

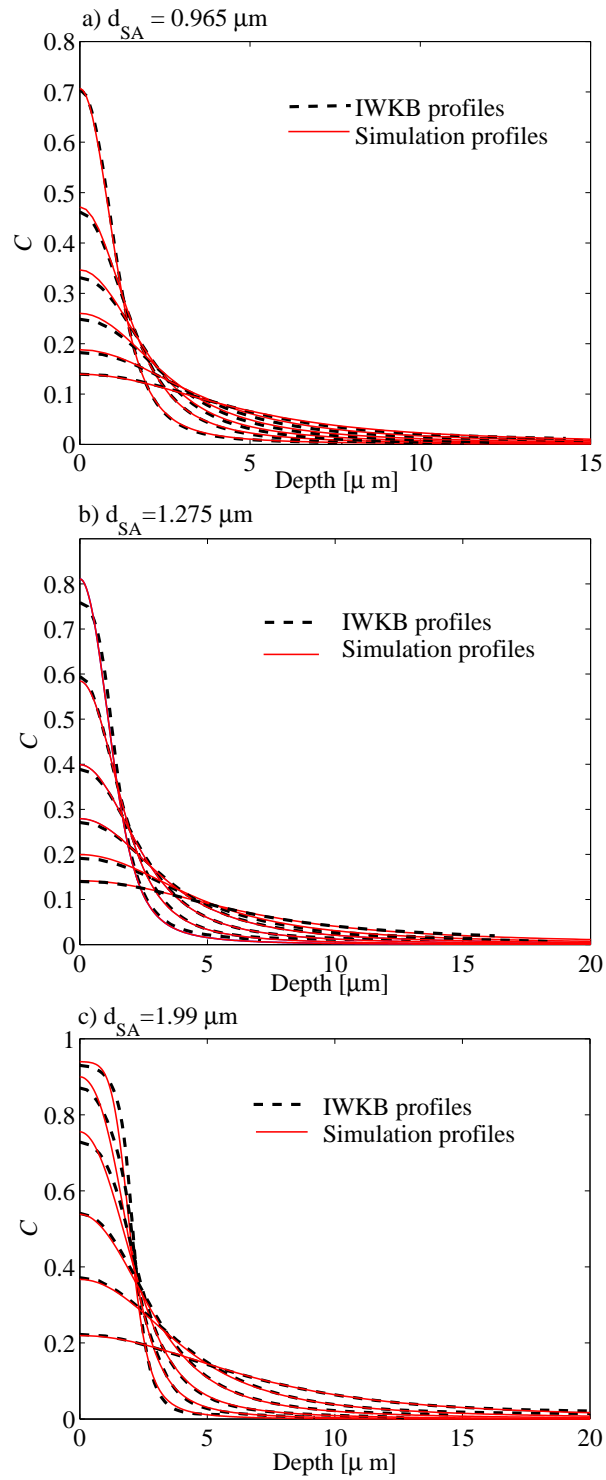


Figure 2.6: Comparison between diffusion simulations and experimental IWKB profiles

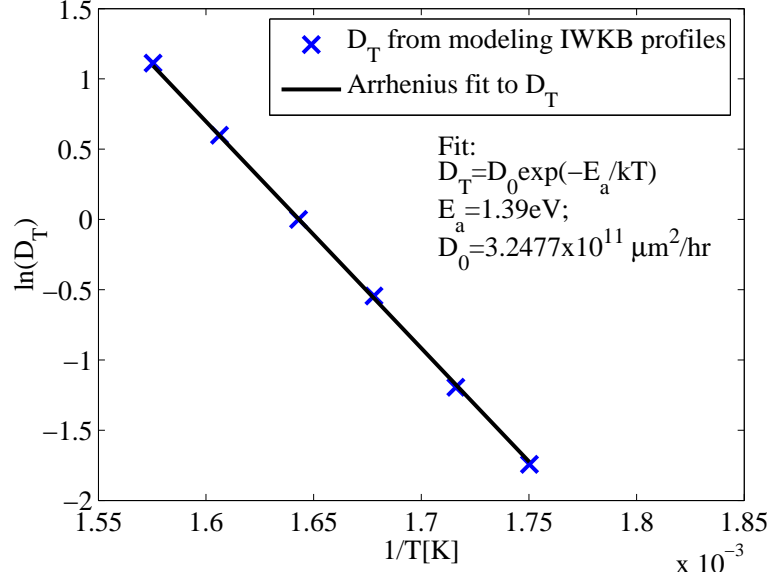


Figure 2.7: Temperature dependence of the diffusion pre-factor

low-concentration layer. Thus, the diffusivity in the low-concentration layer essentially determines the RPE rate in the diffusion-limited regime. It was determined experimentally that aside from the first few minutes of RPE, the exchange process is diffusion limited. The rate of reaction between Li and  $H_xLi_{1-x}NbO_3$  limits the exchange rate only during these first few minutes while the thickness of the low-concentration layer is very small and protons can diffuse through it faster than they can be replaced by Li at the surface.

For RPE simulations, planar waveguide samples with APE waveguides were immersed in the Li-rich melt multiple times for increasing intervals of time. The total number of protons in the waveguides was estimated prior to and after each RPE cycle using the OH absorption measurement. After the end of all RPE processes, an RPE diffusion simulation was performed using the temperature-dependent nonlinear diffusivity. The calculated concentration profiles were integrated to determine the residual proton dose after each simulated RPE cycle. The proton dose is defined as

$$dose = \int_0^{z_{max}} C(z) dz \quad (2.35)$$

and is measured in  $\mu\text{m}$ . The proton dose of a soft annealed waveguide with  $C=1$  is simply

the SA depth  $d_{SA}$ , while if  $C$  is somewhat different than 1, the dose can be estimated as the product  $Cd_{SA}$ .

Typical output profiles of the RPE diffusion simulation are plotted on figure 2.8 starting with the half-bell shaped concentration profile of the initial APE waveguide. Comparing the dose decay after multiple RPE steps with the simulated doses, the coefficient  $\gamma$  could be restricted to the value 0.065. An example plot of the decay of proton dose versus RPE time for one sample is shown in figure 2.9 along with the simulated concentration profile areas. In this particular case, the RPE was performed at 310 °C.

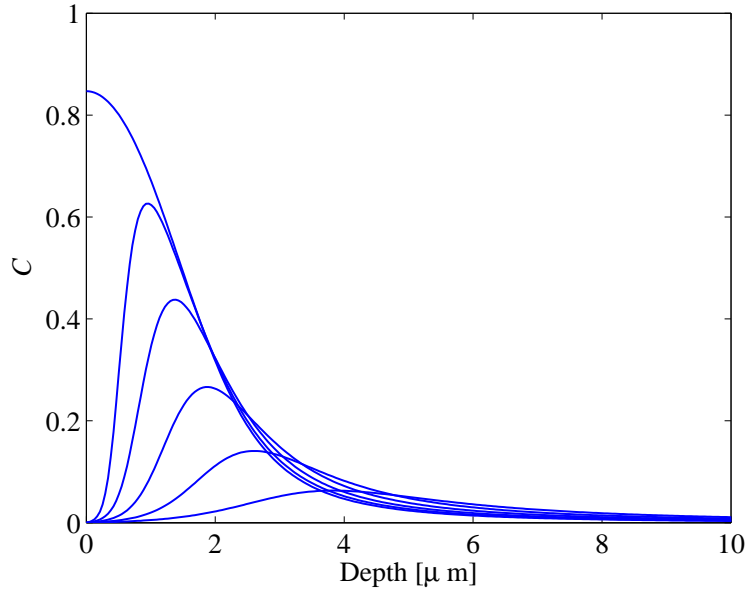


Figure 2.8: Profiles of the normalized concentration generated by an RPE simulation

In summary, the diffusion of protons for annealing and RPE can be simulated accurately for waveguides with soft-annealed depth in the range 1-2  $\mu\text{m}$  by solving the diffusion equation numerically using a nonlinear temperature-dependent diffusion coefficient given by

$$D(C, T) = D_0 e^{-\frac{E_a}{kT}} \left( \alpha + \frac{1 - \alpha}{\beta C + \gamma} \right) \quad (2.36)$$

with all the parameter values defined above. The concentration-dependent rational term actually matches the theoretical concentration dependence for ambipolar ionic diffusion where charge neutrality is to be preserved[144, 129, 115] if the activation energies of the

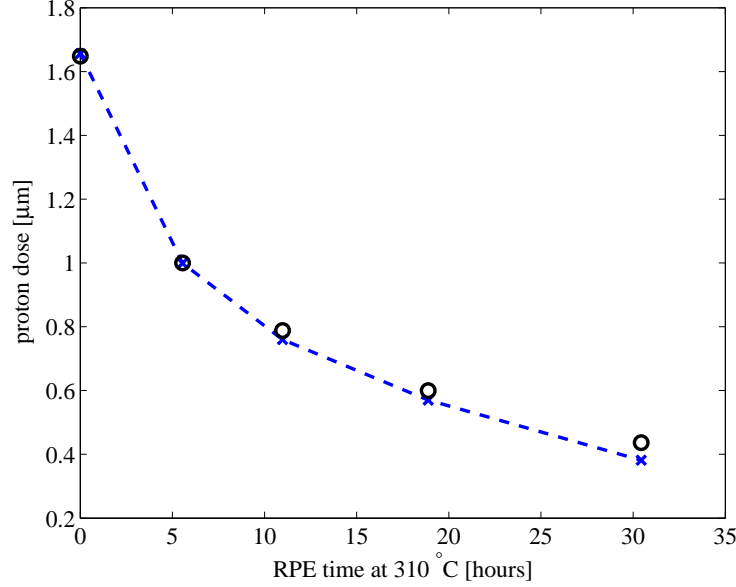


Figure 2.9: Residual proton dose as a function of RPE time at 310 °C. Circles represent experimental data while crosses represent simulation for a waveguide with a SA depth of 1.65  $\mu\text{m}$ .

self-diffusivities of the two interdiffusing ions are equal. In fact, the activation energy for Li-self diffusion in the  $\alpha$  crystalline phase is higher than that for diffusion of protons[129, 115]. In this case, the dependence of the nonlinear diffusivity on concentration is characterized by two activation energies and the parameter  $\beta$  in Eq. 2.36 is temperature dependent. Within the temperature range of interest for device fabrication, it was determined that using a single activation energy provides sufficient accuracy.

The constant additive term  $\alpha$  would be 0 in a single-crystalline-phase ion-exchange diffusion process. The best fits to the experimental data were obtained with  $\alpha=0.08$  rather than 0 probably due to the change in crystalline phase for  $C > 0.27$ , which would be accompanied with a change in the diffusion parameters. The dependence of the diffusion coefficient on concentration is plotted in figure 2.10. It can be seen that the diffusivity changes by two orders of magnitude over the range  $0 \leq C \leq 1$ . Most of the variation occurs within the  $\alpha$  phase  $C \leq 0.27$  which is the phase of maximum importance for APE and RPE waveguides. This is why models of the fabrication process based on linear diffusion (independent of concentration) fail to cover a broad range of fabrication parameters. It is also evident from Fig. 2.10 that the constant additive term  $\alpha$  in Eq. 2.36 contributes a significant fractional

change to the diffusivity only at high concentrations where the crystal is in a different phase with different ion-exchange diffusion parameters.

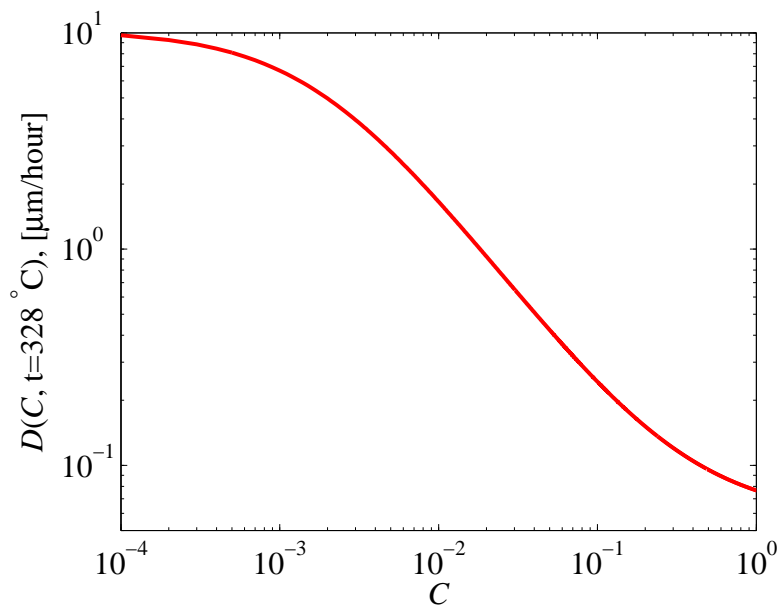


Figure 2.10: Diffusion coefficient at 328 °C versus normalized concentration

## 2.7 Wavelength dispersion of proton-exchanged lithium niobate

Wavelength dispersion data for proton-exchanged lithium niobate was incorporated in the waveguide model by Bortz and Fejer[126]. In that case, the measurements of the refractive index of PE LiNbO<sub>3</sub> were performed on planar PE waveguides after exchange in molten benzoic acid. The refractive index profile of the waveguides was assumed to be a rectangular step-index. As mentioned earlier, a closer approximation to the PE index profile is a trapezoid (see figure 2.2). Using the index/thickness calculation [133] based on measured mode effective indices and approximating a trapezoid with a rectangle leads to an overestimate of the layer  $\Delta n_e$  at short wavelengths and underestimate at long wavelengths. This is because at short wavelengths, the lowest-order modes can be confined in the pointed top part of the trapezoidal index profile, pulling their effective indices up compared to the rectangular profile. If the lowest-order modes have a higher effective index, then the index/thickness

calculation produces an estimate with higher index than the average index of the layer and smaller thickness than the actual thickness.

In this work, an accurate estimate of the dispersion of  $\text{H}_x\text{Li}_{1-x}\text{NbO}_3$  was obtained by measuring the refractive index of SA waveguides which are approximated very well with a rectangular step-profile. Several SA planar waveguides with depths ranging from 1 to 3  $\mu\text{m}$  were measured at wavelengths ranging from 458 to 1550 nm using a prism coupler. The refractive index and thickness were estimated for each wavelength using the index/thickness calculation. Due to a small residual slope at the top of the index profile, the lowest-order mode was skipped in the estimates at the shorter wavelengths if the index/thickness calculation including the lowest-order mode indicated a statistical error in the thickness of more than 1%. In this way, the estimated thickness of each waveguide was the same at all wavelengths.

The experimental measurements of  $\Delta n_e$  are shown in Fig. 2.11 along with a Sellmeier fit and the wavelength dependence used in reference [126] marked on the plot as “Bortz model”. The new dispersion curve is less steep.

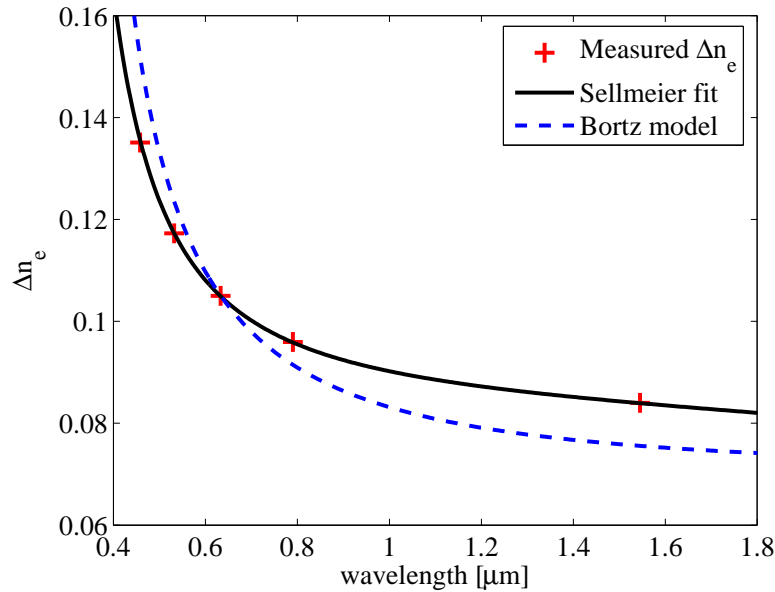


Figure 2.11: Wavelength dependence of  $\Delta n_e$  for SA waveguides with  $C=1$

The curve that fits the experimental data in Fig. 2.11 is given by

$$\Delta n_e(\lambda, C = 1) = \sqrt{a_1 + \frac{a_2}{\lambda^2 - \lambda_0^2} - a_3\lambda^2 - n_e^{sub}(\lambda)} \quad (2.37)$$

where  $a_1=4.945$ ,  $a_2=0.1354$ ,  $a_3=0.0278$ ,  $\lambda_0=0.2324 \mu\text{m}$  and the substrate index is provided by the Sellmeier equation by Jundt[145] with an assumed temperature of  $24.5^\circ\text{C}$ :

$$n_e^{sub}(\lambda) = \sqrt{5.35583 + \frac{0.100473}{\lambda^2 - 0.20692^2} + \frac{100}{\lambda^2 - 11.34927^2} - 0.015344\lambda^2} \quad (2.38)$$

For APE waveguides with  $0 \leq C \leq 1$ , the dispersion is given by

$$\Delta n_e(\lambda, C) = C\Delta n_e(\lambda, 1) \quad (2.39)$$

The assertion in Eq. 2.39 that the dispersion of proton exchanged lithium niobate is independent of concentration was tested by comparing the refractive index profiles of an APE waveguide measured at several wavelengths using a prism coupler and IWKB. The  $\Delta n_e$  profiles were divided by  $\Delta n_e(\lambda, 1)$  from equation 2.37 to reconstruct the corresponding concentration profiles, which are plotted in Fig. 2.12. The concentration profiles recovered from different wavelength measurements lie on top of each other, proving that the dispersion of  $\Delta n_e$  is independent of concentration throughout the region  $0 \leq C \leq 1$ .

## 2.8 Undercutting and diffusion along the crystal y-axis. Model predictions for QPM for channel waveguides.

Channel waveguide optical frequency mixers on z-cut substrates are usually fabricated with the waveguide propagation axis along the crystal  $x$ -axis because in this case the natural walls of the periodic domains used for quasi-phasematching are orthogonal to the waveguide axis for maximum conversion efficiency. After periodic poling, an  $\text{SiO}_2$  layer is sputtered on the wafer surface and channels are formed in it lithographically. The  $\text{SiO}_2$  layer with the channels serves as a stop mask during the proton exchange process, defining the exchange strips that form the channel waveguides.

Besides the properties of planar waveguides on  $z$ -cut substrates, two more characteristics are needed in order to completely predict the fabrication and optical properties of channel waveguides on the same substrates. The first one is the extent of lateral proton exchange

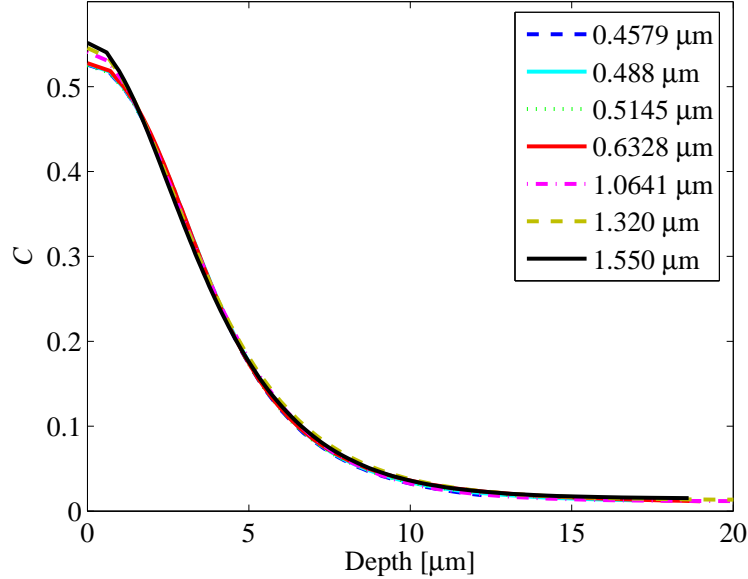


Figure 2.12: APE waveguide concentration recovered from IWKB profiles at different wavelengths

(undercutting) that occurs on either side of the  $\text{SiO}_2$  mask channel during the immersion in benzoic acid. The second unknown property is the diffusivity along the  $y$ -crystal axis.

The undercutting is illustrated in Fig. 2.13. The actual shape of the proton exchanged region has some curved parts at the two edges. The undercutting  $u_{max}$  near the surface was measured by etching deeply exchanged channel waveguides with hydrofluoric acid and measuring their maximum width using a light microscope. Assuming that the undercutting is proportional to the soft-annealed proton exchange depth, it was determined that  $u_{max} \approx (0.45 \pm 0.1)d_{SA}$ . In the modeling, the proton-exchange profile is considered rectangular, and the undercutting is assumed to have a rectangular transverse profile with a width  $u < u_{max}$  (Fig. 2.13).

The high-temperature diffusion along the crystalline  $y$ -axis was not measured directly. An  $x$ -cut wafer was available which allowed planar waveguides to be fabricated that diffuse along the  $x$ -axis. Waveguides on  $x$ -cut substrates experience different stress conditions than waveguides on  $z$ -cut substrates. Therefore, only an approximate estimate of the diffusivity along the  $x$ -axis was sought. It was determined that, within the  $\alpha$  crystalline phase, the effective diffusivity along the  $x$ -axis on  $x$ -cut samples was within the range  $1 \pm 0.4$  times the

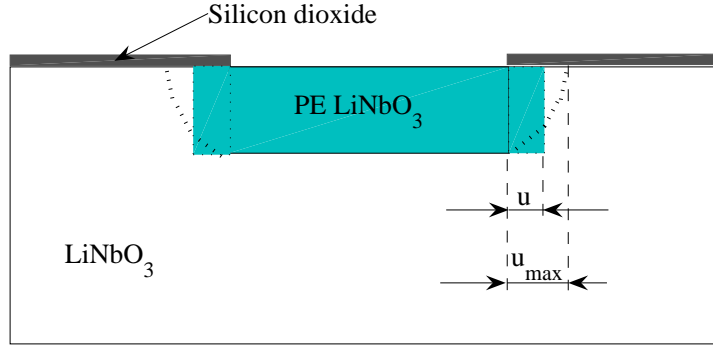


Figure 2.13: Sketch of the transverse cross-section of a PE waveguide with undercutting

diffusivity along the  $z$ -axis on  $z$ -cut substrates.

The phasematched fundamental wavelength of a channel waveguide for SHG can be determined from the dispersion of the mode effective index which can be calculated numerically. From Eq. 1.9, it follows that

$$\lambda_\omega = 2\lambda_{2\omega} = 4L_c(n_{2\omega}^{eff} - n_\omega^{eff}) = 2\Lambda(n_{2\omega}^{eff} - n_\omega^{eff}) \quad (2.40)$$

where  $L_c$  is the coherence length,  $\Lambda = 2L_c$  is the first-order QPM period, and  $n^{eff}$  stands for the effective index of the mode that takes part in the frequency mixing.

The ability to use the model for design and fabrication of waveguide optical frequency mixers was tested by fabricating channel waveguides and comparing them to simulations. The effective index of the of the fundamental mode was calculated as a function of wavelength in the range 0.45-1.6  $\mu\text{m}$ . The resulting mode dispersion curves were used to calculate the phasematching wavelength for each channel waveguide and to compare to experiments. The waveguides were periodically poled with a period of 14.75  $\mu\text{m}$ . Proton exchange was performed in benzoic acid. The soft annealed depth of the witness sample was 1.24  $\mu\text{m}$ . The waveguides were annealed at 330  $^\circ\text{C}$  for 23.75 hours. SHG experiments were performed

using a tunable external-cavity diode laser. The input fundamental wavelength was tuned between 1500 and 1575 nm and signal at the second harmonic was measured at the output. The location of the peak of the SHG tuning curve for each waveguide is plotted in Fig. 2.14 as a circle. The channel width on the horizontal axis denotes the opening in the SiO<sub>2</sub> mask layer. These widths were measured using a light microscope after the lithographic fabrication of the SiO<sub>2</sub> channels. The results of numerical simulations of channel waveguides performed with the help of Xiuping Xie are plotted in Fig. 2.14 as the dashed curve (no undercutting) and the continuous curve (undercutting  $u=0.3d_{SA}$ ). The curve that accounts for undercutting is very close to the experimentally measured phasematching wavelengths.

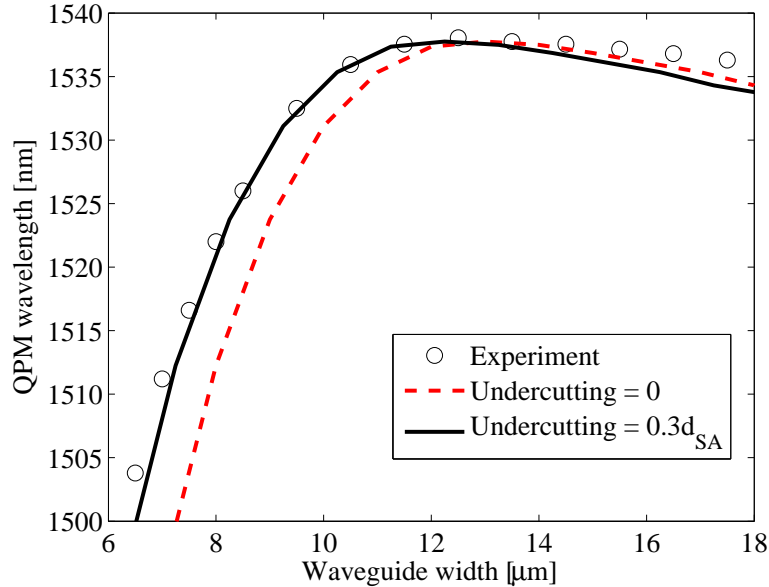


Figure 2.14: Predicted SHG phasematching in APE waveguides

Xiuping Xie[146] reported similar precision in the simulation of RPE waveguides for frequency doubling of 1550 nm with typical deviations of 2 nm between the calculated and experimental phasematching wavelengths.

In addition to predicting the QPM wavelength, the model was found to predict accurately the shape of the mode of APE channel waveguides. Sharpe[147] reported that the mode profiles generated by the model matched very well with his far-field measurements of the output mode of single-mode channel waveguides.

Another test of the model has been performed by simulating directional couplers. The

coupling length of a directional coupler consisting of a pair of closely spaced channel waveguides is given by the expression

$$L_{1/2} = \frac{\lambda}{2(n_s^{eff} - n_a^{eff})}, \quad (2.41)$$

where  $n_s^{eff}$  and  $n_a^{eff}$  are the effective indices of the symmetric and antisymmetric mode of the combined waveguide-pair structure. The coupling length is very sensitive to undercutting and lateral diffusion. In collaboration with Carsten Langrock, couplers based on APE channel waveguides were fabricated and the energy transfer from one channel to the neighboring channel measured as a function of the coupler length to determine  $L_{1/2}$ . Numerical simulations of the couplers were performed in collaboration with Xiuping Xie using the waveguide model in two dimensions. The calculated coupling length matched the coupling length of the tested devices with 3- $\mu\text{m}$  edge-to-edge channel separation with a precision better than 10%. These devices had a coupling length of 1.35 mm.

## 2.9 Full-range Sellmeier equation for proton-exchanged $\text{LiNbO}_3$

Based on the results from section 2.8, the diffusion part of the model can be trusted to predict the concentration profiles of channel waveguides with good precision. This can be used to extend the model to cover the mid-IR portion of the spectrum. Once the concentration profile of channel waveguides is well known, lasers with wavelengths from the known portion of the dispersion curve can be mixed inside a channel waveguide to produce DFG output in the mid-IR. By finding the phasematching peak, the effective index of the DFG mode can be obtained and compared to simulations assuming different material dispersion in the mid-IR.

APE channel waveguide devices were made for difference-frequency generation of 3.3- $\mu\text{m}$  radiation by mixing lasers at 1.064  $\mu\text{m}$  and  $\sim 1.55 \mu\text{m}$ . From the phasematching signal wavelength in the 1.55- $\mu\text{m}$  band, the idler wavelength was found and its effective index extracted from the phasematching condition. By comparing the experimental value with the result of simulations, the refractive index increase at 3.3  $\mu\text{m}$  was estimated to be  $\Delta n_e(3.3 \mu\text{m}, C=1) = 0.068 \pm 0.002$ . Adding this to the experimental values from prism-coupling measurements of APE planar waveguides, a Sellmeier fit was obtained covering the range from 0.45 to 4  $\mu\text{m}$ . The fitting formula is the same as Eq. 2.37 but with slightly different

values for the fitted parameters:  $a_1=4.9586$ ,  $a_2=0.1288$ ,  $a_3=0.0304$  and  $\lambda_0=0.2439$ . This version of the Sellmeier fit does not match the high precision of the previous one in the visible and near-infrared, but properly predicts the phasematching of interactions involving mid-IR generation. The experimental data and the Sellmeier fit are plotted in Fig. 2.15.

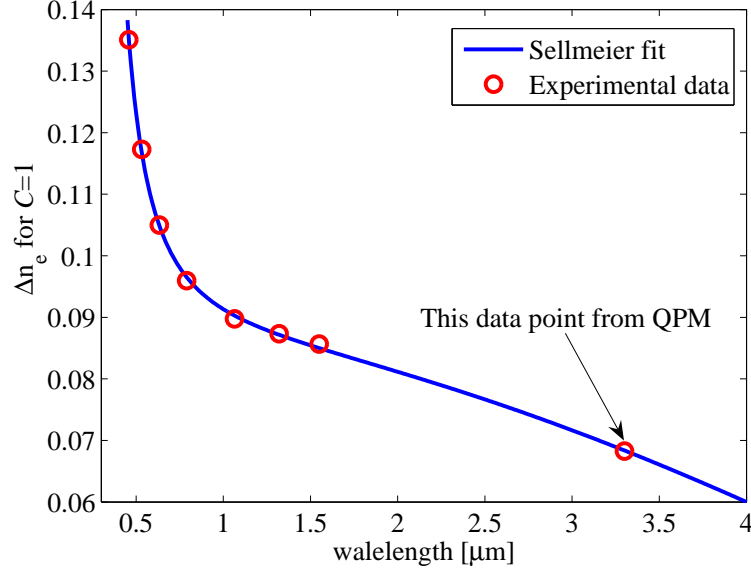


Figure 2.15: Experimental data for  $\Delta n_e(\lambda, C=1)$  and the fitted Sellmeier curve

The full-range Sellmeier equation was used in the design of RPE-waveguide devices for the generation of 4- $\mu\text{m}$  radiation (described in the next chapter) and phasematching was observed within the expected region of the 1.55- $\mu\text{m}$  signal wavelength spectrum.

## 2.10 Propagation losses and mixing efficiency

The propagation losses of APE and RPE channel waveguides have been characterized mostly in the region of 1.55  $\mu\text{m}$ . The Fabry-Perot loss measurement method[148] has been used for its simplicity, precision and reliability. The following general guidelines can be provided based on the accumulated experience:

1. Waveguides containing the  $\kappa_2$  phase are very lossy ( $>5$  dB/cm).
2. RPE waveguides containing the  $\kappa_1$  phase even in small amounts (e.g., peak normalized concentration in the profile of 0.3, most of the profile in  $\alpha$  phase with  $C < 0.25$ ) are relatively lossy (0.4-0.8 dB/cm). APE waveguides can have a thin layer (e.g., 0.5-1  $\mu\text{m}$ ) of  $\kappa_1$  phase

near the surface with maximum concentration  $0.33 \leq C \leq 0.4$  and still have tolerable losses of 0.2 dB/cm. This higher tolerance to the lossy  $\kappa$  phase on APE waveguides is due to the misalignment between the peak of the mode field, which is inside the crystal, and the peak of the concentration profile, which is at the surface. In RPE waveguides the two peaks are aligned and the presence of the  $\kappa_1$  phase leads to high losses.

The losses in the  $\kappa$  phases are most likely due to metastability[149, 150]. For example, if the  $\kappa_1$  phase is metastable at room temperature, it will break up gradually into a mixture of microscopic regions of  $\beta_1$  phase, spread throughout the waveguide region, which is mostly in the  $\alpha$  phase. Because of the large difference in refractive indices between the  $\alpha$  and  $\beta$  phases, the presence of these  $\beta$ -phase regions will cause significant light scattering. Korksihko et al.[150] observed during measurements of the SHG response of different PE LiNbO<sub>3</sub> phases, that the SHG light was not scattered in  $\beta_2$ -phase waveguides that were quickly cooled after the high-temperature annealing. Several months later, the scattering in these waveguides had increased significantly, becoming the same as the scattering in waveguides that were cooled more slowly.

3. In the  $\alpha$  phase, especially when  $C < 0.23$ , both APE and RPE waveguides have low losses (0.1-0.2 dB/cm). For waveguides with very low concentration ( $C < 0.1$ ), the losses are usually dominated by surface scattering because of the reduced mode confinement.

4. Measurements of the SHG output power as a function of pump depletion showed that the losses at the second harmonic near 775 nm are not higher than the losses at 1550 nm. If the losses in the  $\alpha$  phase are caused primarily by surface scattering, the second harmonic could experience lower losses compared to the fundamental, because of the better confinement inside the buried RPE waveguide.

5. The propagation losses in the mid-IR region can vary significantly due to the OH absorption peak. It can cause significant losses (several dB/cm) even at wavelengths relatively far (e.g., 500 cm<sup>-1</sup> away) from the peak center.

6. It is possible that a significant fraction of the low (0.1-0.2 dB/cm) propagation losses at 1.55  $\mu\text{m}$  in RPE waveguides in the  $\alpha$  crystalline phase could be due to absorption caused by the far-reaching wing of same broad component of the the OH absorption peak that we believe is causing the higher propagation losses in the mid-IR region between 2.5 and 4  $\mu\text{m}$ . This conjecture does not contradict the observation that the losses in RPE waveguides at 775 nm are not higher than the losses at 1550 nm. Extrapolation of the absorption losses from the mid-IR to 1550 nm, by assuming that the broad component of the OH peak is

Lorentzian and its width is comparable to that of the combined peak, predicts absorption losses at 1550 nm ranging from 0.05 to 0.5 dB/cm. Future efforts to reduce the waveguide propagation losses at 1550 nm from 0.1 toward 0.01 dB/cm should include careful analysis of this possibility.

The better understanding of the material properties and its incorporation into the modeling allowed the reduction of losses in RPE waveguides from 0.6 to 0.1 dB/cm without sacrificing mixing efficiency, by optimizing the fabrication recipe. Such low losses have been especially useful in the application of PPLN waveguides as mixers for sum-frequency generation for single-photon detection [151, 35] where even moderate propagation losses of 0.4-0.5 dB/cm would prevent the implementation of practical single-photon detectors.

In typical devices with lengths of one to several centimeters, losses greater than a few tenths of a dB/cm can have a significant effect on the externally observed conversion efficiency. For low-loss APE-channel waveguide devices, it was determined that the observed SHG conversion efficiency for frequency doubling of 1.55  $\mu\text{m}$  was between 0.8 and 1 times the efficiency predicted by simulations, assuming that the depth of dead layer equals the soft-annealed depth of the waveguide. The simulations assumed that the region underneath the dead layer had a nonlinear coefficient equal to that of the substrate. The assumption that the dead layer equals the SA depth is consistent with the observation by Korkishko et al.[150] that the nonlinearity of PE LiNbO<sub>3</sub> is strongly reduced in the  $\beta_1$  phase and the finding by Bortz and Fejer[104] that the partial recovery of the dead layer with high-temperature annealing takes times much longer than the typical proton diffusion time for efficient APE waveguide mixers.

Combined with the above observations on losses and mixing efficiency, the numerical model becomes a complete tool for design and optimization of APE and RPE PPLN optical frequency mixers.

## Chapter 3

# Mid-infrared generation and 1.57- $\mu\text{m}$ parametric amplification in reverse proton-exchanged waveguides.

Bright narrow-linewidth sources of tunable mid-IR radiation in the range 3.2 – 3.5  $\mu\text{m}$  can be used for spectroscopic detection and monitoring of methane concentration in the atmosphere. Methane is one of the most important greenhouse gasses, but narrow linewidth tunable light sources with adequate power for quick and sensitive detection of its spectroscopic fingerprint are still lacking. The region near 3  $\mu\text{m}$  is still challenging to cover with quantum-cascade lasers with adequate output power at room temperature.

Single-frequency mid-IR sources could also be used for free-space communications. The Earth's atmosphere is mostly transparent in the wavelength range from 3.5 to 4  $\mu\text{m}$ , which provides a wide spectral region that could be used for transmission of information. With sophisticated optical signal processing available at 1.55  $\mu\text{m}$ , it is of great interest to explore the possibilities for data transmission in the mid-IR combined with optical signal-processing at 1.55  $\mu\text{m}$ . Wavelength conversion between the two specified spectral regions that preserves the data encoding would be necessary. Difference-frequency mixing in a PPLN waveguide has been demonstrated to provide the wavelength conversion between the 1.55- $\mu\text{m}$  and

the 1.32- $\mu\text{m}$  band with the required characteristics [152, 16]. It is worth noting an on-chip directional coupler was used to provide separate single-mode inputs for the pump at 0.71  $\mu\text{m}$  and signal at 1.32 or 1.55  $\mu\text{m}$ . Designing similar APE PPLN devices to perform the same function between  $\sim 1.55$  and  $\sim 3.8$   $\mu\text{m}$  poses greater technical challenges due to the large spread of involved wavelengths (1.1 – 4  $\mu\text{m}$ ), the necessity for single-transverse mode operation, and the unfavorable efficiency scaling of waveguide mixers with increasing wavelength. These challenges are investigated in this chapter. The chapter describes the design and experiments with waveguide devices for difference-frequency mixing involving a pump in the range 0.97 – 1.12  $\mu\text{m}$ , a signal in the range 1.53 – 1.625  $\mu\text{m}$ , and an idler (or DFG) wavelength in the mid-IR range 2.5 – 4  $\mu\text{m}$ . Most of the work involves mixing in which the mid-IR wavelength is near 3.3 or 3.9  $\mu\text{m}$ . In addition, Section 3.4 describes the application of the difference-frequency mixing process in waveguides for practical high-gain optical parametric amplification (OPA).

### 3.1 Brief history of mid-IR DFG in PPLN waveguides

The first use of LiNbO<sub>3</sub> channel waveguides for DFG of mid-IR radiation was reported by Herrmann and Sohler [153] who used birefringent phasematching in a Ti:LiNbO<sub>3</sub> waveguide. They observed 10 nW of mid-IR output with a tuning range from 2.5 to 3  $\mu\text{m}$  and a conversion efficiency  $P_{DFG}/P_s \approx 10^{-4}$  at 50 mW of pump power. The pump wavelength was tunable near 1.5  $\mu\text{m}$ , while the signal wavelength was fixed at 3.39  $\mu\text{m}$ , coming from a He-Ne laser. The length of the waveguide was 4 cm, so that the normalized DFG conversion efficiency was of order  $10^{-2}$  %/Wcm<sup>2</sup>. More recently, the same group reported DFG of 2.8- $\mu\text{m}$  radiation with an efficiency of 105%/W (normalized efficiency of 1.6%/Wcm<sup>2</sup>) by using QPM in an 8-cm long periodically-poled Ti:LiNbO<sub>3</sub> waveguide [154].

Extending the spectral coverage of APE PPLN-waveguide mixers toward the mid-IR started with the work of Lim et al. [155]. They demonstrated the generation of 1.8  $\mu\text{W}$  of 2.1  $\mu\text{m}$  radiation by mixing 160 mW at 0.81  $\mu\text{m}$  with 1 mW at 1.32  $\mu\text{m}$ . The observed normalized DFG efficiency of 4 %/Wcm<sup>2</sup> was 24 times lower than estimated theoretically by mode-overlap calculations.

Mid-IR DFG in APE PPLN waveguides was described for the first time by Bortz [2]. He explored generation of 2.5 – 3  $\mu\text{m}$  radiation by mixing a tunable pump near 0.77  $\mu\text{m}$  with a signal at 1.064  $\mu\text{m}$ . With pump and signal powers of 50 and 100 mW, respectively,

5.5  $\mu\text{W}$  of 2.83- $\mu\text{m}$  output was generated. The observed normalized conversion efficiency of 0.14  $\%/\text{Wcm}^2$  was about 20 – 30 times lower than theoretical predictions by mode-overlap calculations. The PPLN waveguides used by both Bortz and Lim used domain inversion by titanium indiffusion, which is characterized by a limited penetration depth of the domains. This is a disadvantage for mid-IR DFG devices which are usually based on waveguides with large transverse crosssection, including depth.

The highest DFG mid-IR output from proton exchanged waveguides observed prior to the work presented here was reported by Petrov et al. [156], who generated up to 0.14 mW in the range 2.8-3.6  $\mu\text{m}$  by mixing two tunable diode lasers centered around 790 and 1050 nm, respectively, in APE PPLN waveguides. Taking into account the QPM lengths of the DFG devices and the measured conversion efficiency of 1.4-4  $\%/W$ , the normalized experimental DFG conversion efficiency was  $\sim 1\%/W\text{cm}^2$  at 2.82  $\mu\text{m}$  and  $\sim 1.4\%/W\text{cm}^2$  at 3.6  $\mu\text{m}$ . According to the authors, the observed efficiency numbers were  $\sim 4$  times lower than expected. More recently, Bamford and Cook [90] reported a mid-IR tuning range of over 200  $\text{cm}^{-1}$  near 3.3  $\mu\text{m}$  by APE PPLN-waveguide DFG mixing of two tunable lasers with the pump wavelength fixed at 814 nm and the signal tuned from 1050 to 1090 nm.

Furthermore, efficient DFG of 2.3 – 2.45  $\mu\text{m}$  radiation was obtained from a direct-bonded PPLN ridge waveguide [157]. Direct-bonded ridge waveguides do not involve proton exchange and preserve the properties of the substrate. The authors reported a conversion efficiency of 100  $\%/W$  with a 5 cm long device and over 100 nm of DFG bandwidth when using a 0.94  $\mu\text{m}$  pump and a tunable 1.5- $\mu\text{m}$  signal.

### 3.2 Mixing efficiency. Design approach.

To use numerical modeling for optimization of the conversion efficiency of mid-IR DFG, it is necessary to confirm that the results of modeling predictions match well with experiments. It is much easier to obtain reliable experimental data on efficiency by using single-mode devices. Unfortunately, due to the large spectral region (for instance, 1 – 4  $\mu\text{m}$ ) covered by the wavelengths involved in a mid-IR DFG process, a waveguide that supports only one mode at the 1- $\mu\text{m}$  pump, does not support a mode at the mid-IR idler. Waveguides that are mono-mode at the idler usually support more than one mode at the signal and several modes at the pump. A reliable method for coupling the pump and signal into the fundamental mode of the multimode waveguide device would make experiments easier and

the obtained data more trustworthy.

The development of reliable directional couplers requires a stable fabrication recipe, which is based on good understanding of the factors affecting the efficiency. At the beginning of this study, the understanding of mid-IR generation in APE waveguides was not satisfactory, in view of the large discrepancy between expected and experimentally observed efficiencies reported in the literature. It was too early to use the directional-coupler approach [152] for separate optimized coupling of pump and signal. A more satisfactory understanding of APE- and RPE- waveguide mid-IR DFG would be needed before any optimization and standardization of the recipe would be appropriate.

Fortunately, RPE waveguides have a much more symmetric depth profile of the refractive index compared to APE waveguides, allowing the design of an input channel that is single-mode over a wide spectral range. An RPE waveguide single-mode over an octave of bandwidth (from 1550 to 775 nm) was successfully fabricated. This waveguide was not used in practice due to a large asymmetry of the mode at 1550 nm, but it provided an extreme example of this advantage of RPE waveguides.

The approach adopted for developing understanding of mid-IR DFG in RPE waveguides was to use a waveguide section (mode filter, MF) that is mono-mode at 1.064 and 1.55  $\mu\text{m}$  as a single input for efficient coupling of both pump and signal. The MF is followed by an adiabatic taper [5] that slowly changes the mode size to match the fundamental mode of the periodically poled mixing region (Fig. 3.1). The requirement that the single waveguide input be mono-mode at both pump and signal sets limits on the combination of fabrication parameters including the proton-exchanged depth, the annealing temperature and time, and the RPE temperature and time. For instance, with pump and signal at 1.06 and 1.55  $\mu\text{m}$ , respectively, the SA depth is limited to about 2.5  $\mu\text{m}$ . These limitations ultimately lead to misalignment in depth between the idler mode, on the one hand, and the pump and signal modes, on the other. The idler mode tends to grow in size beyond the characteristic depth of the refractive index profile and becomes more and more asymmetric in depth as its wavelength is shifted farther into the mid-IR. The corresponding efficiency rapidly decreases in comparison with the  $\lambda^{-3}$  to  $\lambda^{-4}$  dependence estimated for symmetric waveguides without fabrication restrictions.

The following guidelines were followed in the design of devices described in this chapter:

1. Based on the experience with waveguide frequency mixers for optical signal processing at telecommunication wavelengths, the peak concentration  $C_{max}$  of the RPE waveguides

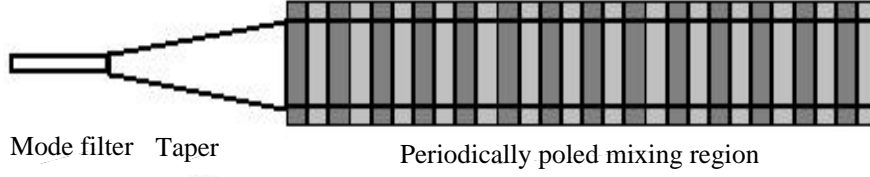


Figure 3.1: Schematic drawing of a PPLN waveguide device for mid-IR DFG

was restricted to the range  $C_{max} < 0.25$  to avoid the excessive losses typical for waveguides containing the  $\kappa$  crystalline phases.

2. To maximize mixing efficiency, a peak proton concentration  $C_{max}$  near the  $\alpha - \kappa$  phase boundary was chosen in order to obtain the best possible confinement of the mid-IR light.

3. The characteristic depth of the proton-concentration profile was varied by adjusting the fabrication process parameters (SA depth, anneal temperature and time, RPE temperature and time), to optimize mode overlap. Propagation losses were not considered in the initial designs.

4. Large channel waveguide widths were used ( $>12 \mu\text{m}$ ), to ensure that the mid-IR idler mode could be well confined and far from cut-off. This choice was made after early experiments [158] on waveguide optical parametric amplification at  $1.6 \mu\text{m}$  with idler at  $3.2 \mu\text{m}$  showed highest gain for waveguide widths of  $14 - 15 \mu\text{m}$  where idler confinement was good. Waveguides with smaller widths down to  $7 \mu\text{m}$  also guided the idler, but the observed gain was smaller.

5. Since DFG efficiency is quadratic with interaction length in the low-gain regime and exponential in the high-gain regime, it was assumed that a device optimized for efficiency should have a long interaction length. Achieving the theoretical efficiency with such devices normally requires non-critical phasematching, especially with respect to the width of the waveguide channel, so that small variations in the width of the fabricated mask do not cause a significant change in the phasematching wavelength. The regime of non-critical phasematching with respect to a parameter  $\xi$  is achieved when

$$\frac{d\lambda_{QPM}}{d\xi} = 0 \quad (3.1)$$

Non-critical phasematching with respect to waveguide width was pursued experimentally

by fabricating waveguides with different widths and tracing the dependence of measured QPM wavelength on waveguide width.

The mode overlap for the case of DFG of 4- $\mu\text{m}$  radiation in a waveguide optimized following the above guidelines is illustrated in Fig. 3.2. The thick black line represents the concentration profile, while the dashed lines represent the normalized fields of the modes. The plot is the result of a one-dimensional (planar waveguide) simulation, using the model described in the previous chapter. The mode fields in the one-dimensional case are normalized such that

$$\int |E|^2 dz = 1 \quad (3.2)$$

Most of the device development described in this chapter was supported by one-dimensional rather than two-dimensional simulations since apart from lateral confinement, all other factors affecting efficiency are related to depth: concentration profile asymmetry in depth, mode asymmetry and misalignment in depth, depth-confinement of the modes, and mode location in depth with respect to the dead layer. One-dimensional simulations take significantly shorter time to compute compared to two-dimensional (channel waveguide) ones. Therefore, a large range of experimental parameters can be explored efficiently.

The plots in Fig. 3.2 illustrate all the issues that restrict the mixing efficiency. Increasing the RPE time would make the profile more symmetric by removing protons from the steeper slope near the waveguide surface, but it would also reduce the peak concentration causing weaker guiding of the idler. Decreasing the annealing time would make the profile more symmetric by steepening the slope on the deep side of the profile, but it would also reduce the total number of protons in the waveguide and again loosen the idler mode (notice that the idler mode at 4  $\mu\text{m}$  extends beyond the characteristic depth of the concentration profile). Making the SA depth larger would help make the profile more symmetric, but it would also lead to a thicker dead layer as well as problems with making a single-mode MF-taper input. The plots also illustrate the advantages of RPE-waveguide-profiles over the half-bell shaped APE profiles. The more symmetric depth distribution allows better alignment of the modes in depth. In addition, burying of the waveguide by RPE has two more advantages. One advantage is the pushing of the modes beyond the depth of the dead layer for higher mixing efficiency. The other advantage is the reduction of the propagation losses that are due to surface scattering.

Using the waveguide model in two dimensions to simulate channel waveguides, the DFG efficiency was calculated for the cases of 3.2- and 3.9- $\mu\text{m}$  generation. In the numerical

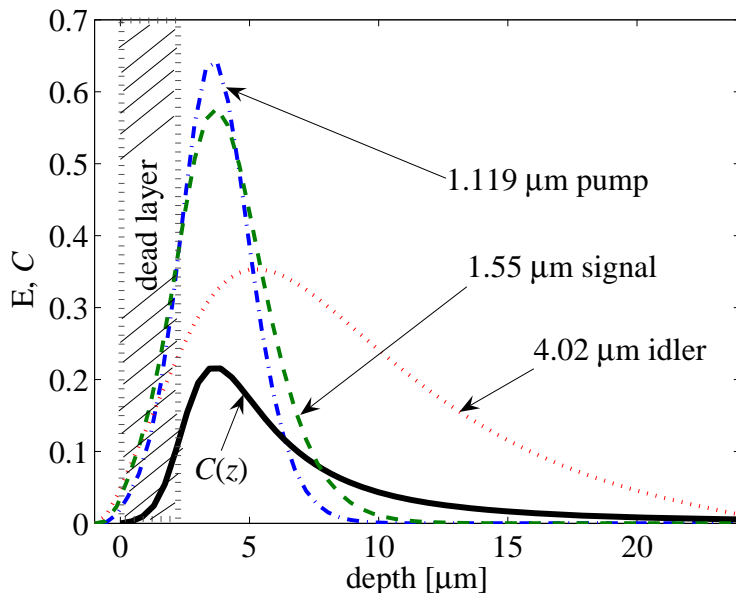


Figure 3.2: Mode overlap for DFG of 4- $\mu\text{m}$  radiation in a planar RPE waveguide. On the ordinate axis,  $E$  stands for the normalized mode field, while  $C$  stands for the normalized proton concentration.

simulations, a surface dead layer with  $\chi^{(2)}=0$  was assumed to occupy a thickness equal to the SA depth of the waveguide, while the rest of the waveguide cross-section was assumed to have undegraded nonlinear optical properties. The width of the dead layer equaled the sum of mask channel width and the undercutting on each side. Channel width and fabrication process parameters were varied between different simulations. The best normalized efficiency for the generation of 3.2  $\mu\text{m}$  and 3.9  $\mu\text{m}$  with an input signal near 1.57  $\mu\text{m}$  were 7 and 1.85 %/Wcm<sup>2</sup>, respectively. If a simple scaling with wavelength were to be extracted from these two numbers alone, it would be between  $\eta_{norm}^{DFG} \propto \lambda_{DFG}^{-6}$  and  $\eta_{norm}^{DFG} \propto \lambda_{DFG}^{-7}$ .

### 3.3 Experimental results on mid-IR generation

Mid-IR generation in the range 3.9 – 4.05  $\mu\text{m}$  was explored experimentally by fabricating devices with depth concentration profiles close to that in Fig. 3.2. The first chip of waveguide devices had a soft-annealed depth of 2.45  $\mu\text{m}$ , a high-temperature annealing of 30.1 hours at 340  $^{\circ}\text{C}$  and a reverse proton exchange of 19.75 hours at 312  $^{\circ}\text{C}$ . The final proton dose in the witness sample after RPE was 1.34  $\mu\text{m}$ , with a concentration profile

closely matching that of Fig. 3.2. The channel waveguides were 52-mm long. The lengths of the mode-filter, the taper and the periodically poled mixing region of each waveguide were 1.5 mm, 4.5 mm and 46 mm, respectively. Three mode-filter widths were used: 2, 2.25 and 2.5  $\mu\text{m}$ . The width of each taper increased quadratically along its length, starting from the mode filter width and finishing with the width of the mixing region. The mixing regions were fixed-width waveguides. The set of widths used for mixing regions included 15, 16, 17, 18, 20 and 21  $\mu\text{m}$ . The propagation losses of the waveguides at 1.55  $\mu\text{m}$ , measured by the Fabry-Perot method [148], were 0.1-0.2 dB/cm, except for some defective channels.

A single-mode continuous-wave fiber laser at 1119.1 nm, built by Supriyo Sinha, was used as the pump in all experiments with mid-IR DFG in the range 3.8–4.1  $\mu\text{m}$ . The signal was provided by an external-cavity diode laser, tunable from 1530 to 1575 nm, passing through an erbium-doped fiber amplifier (EDFA). The gain bandwidth of the EDFA was roughly covering the range 1530-1570 nm. The two input lasers were collimated using fiber collimators and combined in free space with properly coated mirrors. They were focused into the waveguide input using an aspheric lens with an effective focal length of 15 mm. For efficiency measurements, the output of the waveguide was angle-polished to suppress Fabry-Perot effects. The mid-IR DFG output signal was collimated with an uncoated aspheric ZnSe lens. This lens had a diameter of 25.4 mm and an effective focal length of 28 mm. The mid-IR idler was separated from the pump and signal by a Ge filter. The detection was performed using a pyroelectric detector and a lock-in amplifier. The input signal beam was chopped at 300 Hz. Higher chopping frequency would reduce the responsivity of the pyroelectric detector. The detector was calibrated at 1119.1 nm and at 1550 nm by comparing with a standard powermeter (Newport model 818-IR). The responsivity was the same at 1119.1 and 1550 nm within 5–10%. The responsivity in the range 3-4  $\mu\text{m}$  was assumed to be similar.

Up to 60 mW of signal were used inside the waveguide. The coupled pump power was  $\sim 3$  mW. All three mode filter widths ensured mono-mode signal. The pump appeared mono-mode for the narrowest mode filter, but not for the wider ones. Even though the wider mode filters were multimode at the pump wavelength, with proper mode-matching for the fundamental mode on the input they could still be used for relatively stable pump coupling, since they only supported 3 modes, with the higher-order modes much larger in diameter than the fundamental mode. The location of the phasematching peak was measured for all waveguide widths by detecting the maximum mid-IR signal. The location was

determined with a measurement error of  $\sim 0.6$  nm due to instability of the signal polarization caused by the EDFA. The estimated conversion efficiency was  $20 \pm 7\%$ W. A plot of the phasematching signal wavelength versus the mask channel width is shown in Fig. 3.3. Non-critical phasematching is observed at a width of  $17 \mu\text{m}$ .

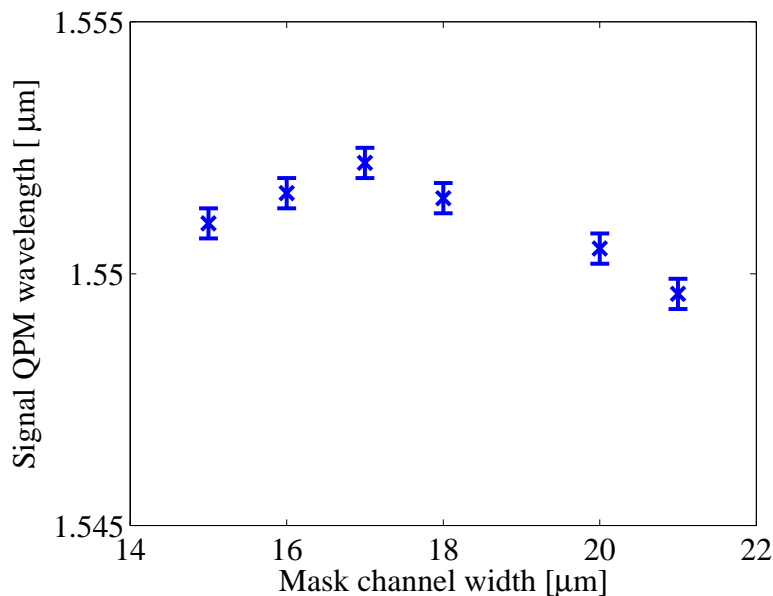


Figure 3.3: Phasematching signal wavelength versus waveguide width

Channel-waveguide numerical simulations were performed and compared with the above experimental results. It was assumed that the dead-layer depth was equal to the soft-annealed depth. The non-critical width from simulations matched the experimentally observed value when the diffusion coefficient along the crystalline  $y$ -axis was assumed to be 0.6 times that along the  $z$ -axis. The predicted normalized mixing efficiency varied from  $1.5 \text{ \%}/\text{W}\cdot\text{cm}^2$  for a channel width of  $15 \mu\text{m}$  to  $1.85 \text{ \%}/\text{W}\cdot\text{cm}^2$  for a channel width of  $20 \mu\text{m}$ , where the efficiency passed through a maximum. Assuming a lossless waveguide with a 4.6-cm-long mixing region, the expected overall conversion efficiency would be in the range  $32\text{--}39 \text{ \%}/\text{W}$ , about 75 % higher than the observed range. If the assumption that the nonlinear coefficient is undegraded beneath the dead layer is correct, the difference between experimental and theoretical efficiency could be attributed to losses of  $1.1 \pm 0.3 \text{ dB}/\text{cm}$  at the mid-IR wavelength. The actual mid-IR losses may be somewhat smaller if the nonlinear coefficient is partially reduced at depths larger than the dead layer, where the waveguide is

in the  $\alpha$  crystalline phase.

For a more precise estimate of the losses near 4  $\mu\text{m}$ , new chips were designed. The waveguide widths ranged from 13 to 20  $\mu\text{m}$ . For each channel width, three waveguides were fabricated with different lengths of the mixing region. One waveguide had a full-length mixing section, 46-mm long, another had a half-length section, 23-mm long, located near the output of the waveguide, and the third had a half-length section located near the input of the waveguide, right after the taper (see Fig. 3.1). Two chips, C3 and C6, were fabricated and tested, with soft-annealed depths of  $\sim 2.41$  and  $\sim 2.39$   $\mu\text{m}$ , respectively. The two samples were annealed for 30 hours at 340  $^{\circ}\text{C}$ . RPE was performed at 312  $^{\circ}\text{C}$  for 18.75 hours and 19 hours, respectively. The final proton doses were 1.33  $\mu\text{m}$  for sample C3 and 1.30  $\mu\text{m}$  for sample C6. The QPM periods were 25.85 and 26.0  $\mu\text{m}$ , respectively. With the pump at 1119.1 nm, the signal QPM wavelength in chip C3 ranged between 1557 and 1562 nm, while in chip C6 it ranged between 1565 and 1567 nm. The mid-IR idler wavelengths were near 3.95 and 3.92  $\mu\text{m}$ , respectively. In both chips, the full-length QPM sections produced significantly more DFG output than the half-length sections, indicating that device performance was not dominated by losses. In chip C3, the output mid-IR power, produced by the QPM half-length sections located near the input, was on average 60% of that produced by the half-length sections located near the output. The signal losses, measured at 1550 nm using the Fabry-Perot method, were  $0.13 \pm 0.06$  dB/cm in chip C3 and  $0.1 \pm 0.04$  in chip C6, except for some defective waveguides which were not included in the analysis. The spread for each number indicates the range of data, rather than standard deviation. The losses at the pump were assumed to be the same as the losses at the signal. The pump and signal losses also affect the DFG output, so they need to be taken into account. The pump and signal have more power in the sections located near the input than in the sections located near the output, due to the 0.13 dB/cm power loss along a waveguide. Since the offset in position between the the different half-length sections was 2.3 cm, the both pump and signal would have on average 0.3 dB less power in the sections near the output than in the sections near the input. The nonlinear polarization, proportional to the product of pump and signal electric fields, would be reduced by  $0.3/2 + 0.3/2$  dB in a half-length section near the output compared to a half-length section near the input. The DFG power, proportional to the square of the nonlinear polarization at phasematching, would be  $0.3 + 0.3 = 0.6$  dB smaller in the case without losses. This difference is to be added to the observed difference of 2.2 dB, in order to determine the idler losses alone. Therefore,

the losses at the idler are  $(2.2+0.3+0.3)$  dB divided by the longitudinal spacing of 2.3 cm between the two types of sections, or 1.2 dB/cm. In a similar way, the losses in chip C6 are estimated at 0.7 dB/cm, since output DFG power generated by half-length QPM sections located near the input is  $\sim 75\%$  of that produced by sections located near the output, and the pump and signal losses were  $\sim 0.1$  dB/cm. The following conclusions can be made:

1. The losses in the mid-IR are significantly higher than the losses near  $1.55 \mu\text{m}$ .
2. The higher losses in chip C3 correlate with a slightly higher peak proton concentration. The estimated peak concentration in chip C3 was in the range  $\sim 0.21\text{--}0.22$ , while it was  $\sim 0.20\text{--}0.21$  in chip C6.
3. The higher losses in chip C3 also correlate with a slightly shallower waveguide burying. The waveguides in chip C6 were buried slightly deeper with the longer RPE. The difference is small, though, and not likely to cause a significant difference in propagation losses. So far, no special experiments have been performed to determine whether losses due to surface scattering have a major contribution in the observed high losses in the mid-IR.

Waveguides from chip C6 were also used for DFG mixing efficiency measurements using the same pair of lasers described above. The observed efficiency range was  $12\text{--}25\%/W\text{-cm}^2$  for waveguide widths between 15 and 21  $\mu\text{m}$ . The measurement error was comparable to the difference in efficiency between different devices. The efficiency was highest for the waveguides with widths of 16 and 17  $\mu\text{m}$ , where the non-critical width was located.

A waveguide from chip C6 with a width of 14  $\mu\text{m}$  and a full-length QPM section, was used for generation of mW-level mid-IR radiation. In order to obtain high mid-IR power, the output of the 1119.1-nm pump laser was passed through a fiber amplifier, delivering up to 160 mW of output power. The dependence of DFG-output power on signal power coupled in the waveguide with a fixed pump of 114 mW inside the waveguide is plotted in Fig. 3.4. The observed efficiency is  $\sim 6\%/W$ . The linear relation between signal and idler, characteristic for the low-conversion regime, is confirmed. At the maximum DFG power of 5.7 mW, over 20 mW of pump had been converted to signal and idler.

A similar plot for the dependence of mid-IR DFG power on pump power for a fixed signal of 936 mW coupled inside the waveguide, is plotted in Fig. 3.5. With pump power near 100 mW and several hundred milliwatts of signal, some red, green and orange light was observed on the output of the waveguide due to parasitic SHG of the signal, SHG of the pump, and SFG between the pump and the signal, respectively. These small amounts of visible parasitic light caused observable shifting and distortion of the QPM tuning curve

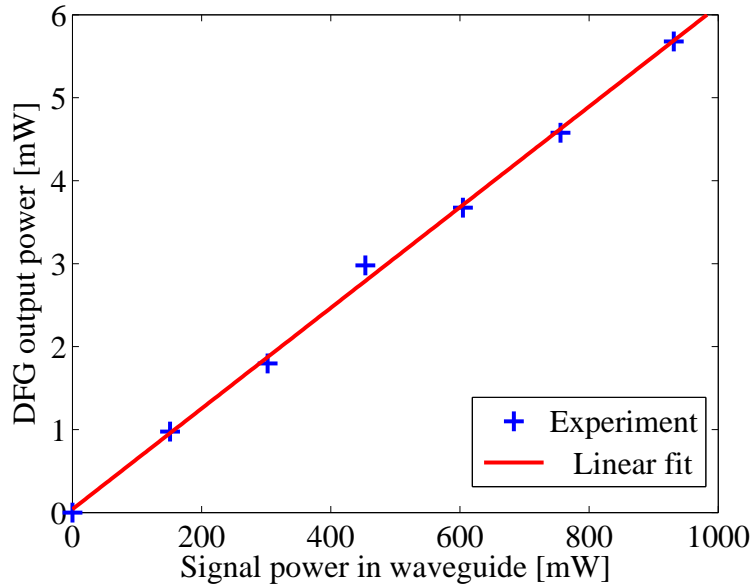


Figure 3.4: DFG power versus signal power for a pump power of 114 mW coupled in the waveguide

at room temperature presumably due to the photorefractive effect. The measurement time was limited to 10-20 seconds per point, to avoid significant photorefractive damage to the waveguide.

To observe higher DFG output power, the power of the pump laser was briefly increased 239 mW by heating the fiber amplifier and increasing the current of its pump diodes. With  $\sim 170$  mW of coupled pump power and  $\sim 900$  mW of signal, 8.1 mW were generated at 4  $\mu\text{m}$ .

The observed efficiency in the high-power experiments was 2–4 times smaller than the efficiency estimated during the preliminary measurements without the fiber amplifier at the pump wavelength. The two most likely reasons for the discrepancy are multimode pump coupling and photorefractive effects. The low-power experiments were performed using a different fiber collimator for the pump beam and a different focusing lens on the waveguide input, producing a smaller pump spot-size. During the high-power experiments, the pump exiting the PPLN waveguide appeared multimode. This means that a significant portion of the pump power was coupled into higher-order modes. Normalizing to the total multimode-pump output power would reduce the estimated efficiency, since a portion of the power

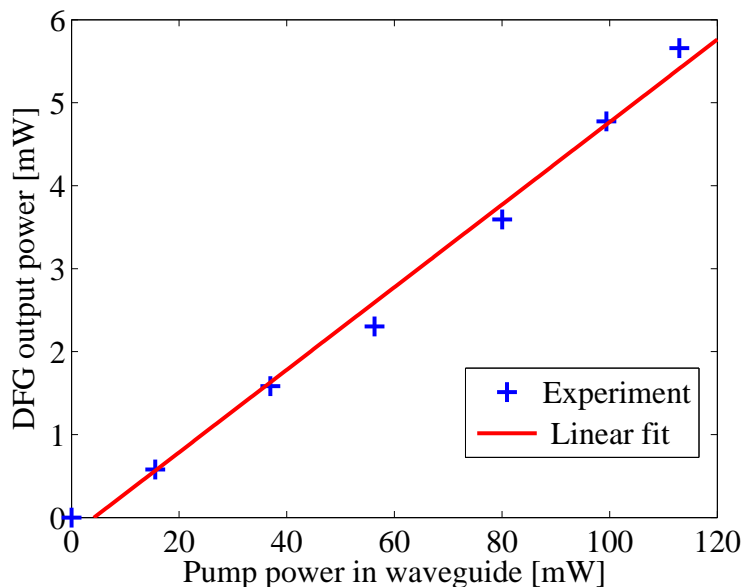


Figure 3.5: DFG power versus pump power for a fixed signal of 936 mW coupled in the waveguide

does not contribute to the nonlinear interaction. The broadening of the tuning curve due to photorefractive effects is the second reason for reduced efficiency in the milliwatt-DFG-level experiments. For example, two tuning curves for the signal, taken at the beginning of a DFG-measurement on one waveguide and after generation of 2–5 mW of mid-IR for a few minutes, are shown on Fig. 3.6. The absolute efficiency in each of the tuning curves has not been measured accurately, so only the shape is of interest. The second tuning curve (the dashed line) is clearly asymmetric and will correlate with a reduced efficiency compared to an ideal  $\text{sinc}^2$  tuning curve. Even though some care was taken to reduce photorefractive effects, they may have contributed up to 20–30 % reduction of efficiency by broadening the tuning curve and reducing its peak efficiency value. More than 30 % of efficiency reduction could not be attributed to photorefractive effects, since they would have led to significant deviation of from the linear dependence of DFG-output power on pump and on signal power. Small effects on the efficiency could be missed in experiments that use shorter measurements at higher power, which is a naturally done to avoid photorefractive effects. Both the longer measurements at small power levels and the shorter measurements at high power levels may be subject to the same “tolerable levels” of photorefractive effects

accepted during the measurements, leading to similar efficiency reduction in a range of power levels. Higher temperature measurements were not performed, since it had been discovered that the waveguide losses in the mid-IR increase with temperature (described later in this section).

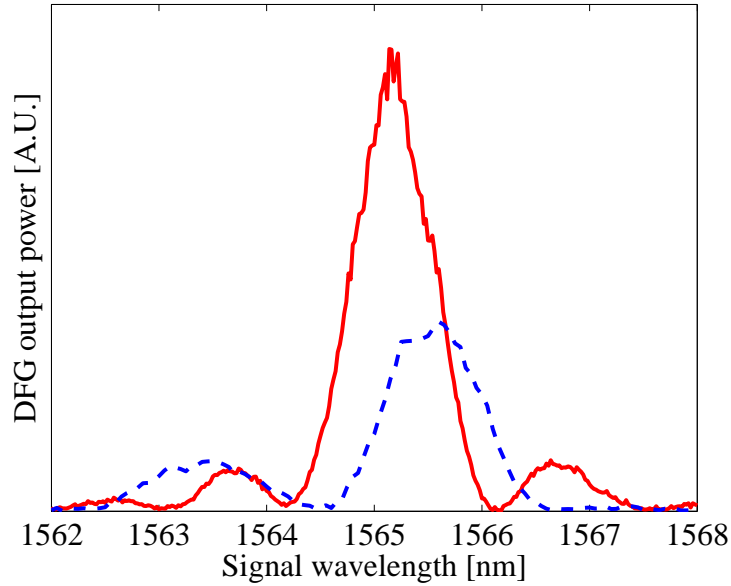


Figure 3.6: DFG tuning curves taken at different times of the experiment

Similar experiments were performed for the generation of mid-IR radiation with a wavelength in the range 3.2-3.45  $\mu\text{m}$ . The waveguide chip (C4) contained channel devices with widths ranging from 14 to 20  $\mu\text{m}$ , QPM periods of 25.65, 25.80 and 25.95  $\mu\text{m}$ . The soft-annealed depth of the sample was 2.4  $\mu\text{m}$ . It was annealed for 30 hours at 340  $^{\circ}\text{C}$ . After RPE of 18.8 hours at 312  $^{\circ}\text{C}$ , the final proton dose was  $1.348 \pm 0.01 \mu\text{m}$ . Using a 1064-nm laser as the pump and an amplified tunable diode laser near 1550 nm as the signal, DFG near 3.3  $\mu\text{m}$  was explored. The observed efficiency was lower than that near 4  $\mu\text{m}$ , opposite to the wavelength scaling described earlier. The difference is attributed to propagation losses in the mid-IR, which increase as the DFG output wavelength approaches the  $\text{OH}^-$  absorption peak. By comparing the theoretical expectations with the experimental efficiencies, the losses at 3.3  $\mu\text{m}$  were estimated to be  $\sim 6 \text{ dB/cm}$ .

For mW-level DFG, pump powers of several hundred milliwatts were used. In order to

reduce photorefractive effects, the experiments were performed at 70 °C. The signal phase-matching wavelength was  $\sim 1543$  nm for a QPM period of 25.80  $\mu\text{m}$  and  $\sim 1567$  nm for a QPM period of 25.95  $\mu\text{m}$ . The corresponding mid-IR idler wavelengths were 3.43 and 3.31  $\mu\text{m}$ , respectively. The highest efficiency was observed with the narrowest waveguide width (14  $\mu\text{m}$  for this interaction), which was also non-critical. The efficiency at elevated temperatures was smaller compared to room temperature, and the tuning curves were wider. This was attributed to increased propagation losses, since the tuning curves did not have structure (as typically seen during significant photorefractive damage), but appeared Lorentzian, which is typical in the loss-limited regime. In addition, the normalized efficiency of generation of 3.43  $\mu\text{m}$  was 20-25% higher than that for generation of 3.31  $\mu\text{m}$ . This can indeed be the case if the mid-IR losses are caused by the  $\text{OH}^-$  absorption peak centered near 2.86  $\mu\text{m}$ .

An example of generation of 3.428  $\mu\text{m}$  in a 6-cm-long device is shown on Fig. 3.7. The observed efficiency is 2.5 %/W. The curve deviates from a straight line at high pump powers due to photorefractive effects. With nearly 1 W of pump in the waveguide, the parasitic second harmonic at 532 nm causes photorefractive effects that are significant even at 70 °C. Note that at each pump power increase, the initial DFG-output followed the linear dependence on pump power, but at pump levels in the waveguide of 500 mW or more it quickly dropped to the smaller power levels, shown in the figure.

In an identical experiment with higher signal power and a different QPM period, 14 mW were generated at 3.3  $\mu\text{m}$  with 0.92 W of pump and 0.25-0.3 W of signal in the waveguide. This amount of DFG radiation in the wavelength range 3-4  $\mu\text{m}$  is 2 orders of magnitude higher than previously reported power levels generated by DFG in proton exchanged waveguides [156]. The power level could not be sustained above 10 mW for more than a minute due to photorefractive effects.

Future optimizations of mid-IR efficiency should focus on the reduction of the mid-IR losses. One possibility is to consider reducing the final peak concentration of the proton concentration profile below  $C = 0.2$ .

### 3.4 Parametric amplification in RPE waveguides

Difference-frequency mixing in a waveguide allows high conversion efficiency at low and intermediate pump power. It can provide energy-efficient optical parametric preamplification

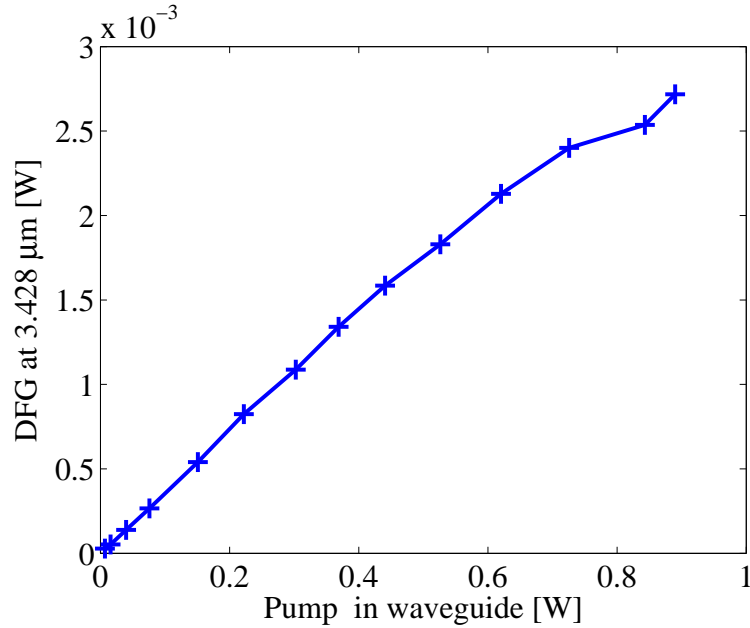


Figure 3.7: DFG output power at 3428 nm versus pump power coupled in the waveguide

for high-power pulse generation in the 1.55- $\mu\text{m}$  band for remote sensing applications. In particular, measurements of the Doppler frequency shift of laser pulses reflected from inhomogeneities and aerosol particles in the atmosphere could be used for accurate estimates of the wind velocity. In order to achieve a precision of 1 m/s, the spectral bandwidth of the pulses should be of order 1 MHz or narrower. This sets a limit on the pulse length, which must be of order 0.5  $\mu\text{s}$  or higher.

One way to achieve the necessary pulse energies of 100 mJ to 1 J with the specified narrow linewidth is to use a continuous-wave distributed feedback laser at  $\sim 1.55 \mu\text{m}$  with output power of 10-20 mW and amplify it parametrically by using a high-power laser near 1  $\mu\text{m}$  as the pump. The required power gain is 70-80 dB. One approach to achieve this gain is divide it between two amplifier stages. The first stage is a low-power preamplifier, the second stage is a power amplifier[159]. The preamplifier provides substantial gain at low pump power, so that most of the available pump power can be saved for use in the power amplifier, from which it can be extracted efficiently.

APE and RPE waveguides were designed and characterized in order to determine their applicability as a preamplifier for the described remote-sensing laser system. Due to the depth asymmetry of APE waveguides, designing a single mode-filter for both pump and

signal presented a challenge when the two input interacting wavelengths were widely different. Using the numerical model of Chapter 2, a narrow range of fabrication parameters for single-mode operation at both input wavelengths was determined. The soft annealed depth was limited to about 1.3  $\mu\text{m}$ , which limited the confinement of the 3- $\mu\text{m}$  idler and the conversion efficiency. Using contact photolithography, the narrowest reproducibly achievable waveguide width was limited to 1.25  $\mu\text{m}$ . Narrowing the mask width in the mode filter region allowed the reduction of the total number of protons in the mode-filter channel and the number of propagating modes. With soft annealed depths in the range 1.15–1.3  $\mu\text{m}$ , the maximum mode-filter width for a single-mode operation at the pump wavelength was  $\sim 2$   $\mu\text{m}$ . The mode size of the signal in such mode filters was large (15–20  $\mu\text{m}$ ), so that a very long taper would be necessary for adiabatic conversion to the tightly confined ( $\sim 3$   $\mu\text{m}$  in depth) mode in the mixing region. Considering the above limitations and using modeling to determine the QPM period, APE PPLN waveguides with widths between 10 to 18  $\mu\text{m}$  were fabricated. The waveguides were proton exchanged in benzoic acid at 161  $^{\circ}\text{C}$  for 22.5 hours to a SA depth of 1.27  $\mu\text{m}$  and annealed at 332.8  $^{\circ}\text{C}$  for 21.4 hours. The total device length was 52 mm, with 46 mm of poling, 2-mm-long linear tapers on input and output and a 2-mm-long mode-filter on the input. The propagation losses in the mode filters were estimated using the Fabry-Perot fringe contrast[148], by testing single-mode waveguides without tapers. Significant difference was observed between narrow single-mode waveguides without tapers and wide multimode waveguides with tapers. The narrow single-mode waveguides had losses of 0.16, 0.10, and 0.07 dB/cm, for waveguide widths of 1.5, 1.75, and 2  $\mu\text{m}$ , respectively. The apparent losses in the tapered waveguides varied significantly. The insertion losses of the tapers were estimated at  $2.5 \pm 0.5$ ,  $1.8 \pm 0.4$  and  $1.2 \pm 0.3$  dB/taper. Such taper performance would not be satisfactory for a good device design.

Phasematching was obtained with a period of 23.9  $\mu\text{m}$ , for signal wavelengths ranging from 1596 to 1617 nm at waveguide widths between 12 and 18  $\mu\text{m}$ . Waveguides narrower than 12  $\mu\text{m}$  did not support a guided mode at the 3.1  $\mu\text{m}$  idler. Using 200-ns input pump pulses with peak power of  $100 \pm 40$  W, a maximum gain of 10 dB was obtained at a signal wavelength of 1617 nm and a waveguide widths of 16  $\mu\text{m}$ . The amplified signal at a gain of 10 dB was 7.3 mW. With over 25 W of pump inside the waveguide, the gain was in the unsaturated regime. Assuming perfect QPM and a lossless waveguide, the normalized conversion efficiency was estimated at  $0.6\%/W\text{-cm}^2$  using Eq. 2.23. This value is several times smaller than the expected range of 2-4  $\%/W\text{-cm}^2$ , based on modeling. The difference

could be attributed to significant idler losses near  $3.1\ \mu\text{m}$ , which reduce the gain, and to the sub-optimal tapers.

At high pump powers, reduced transmission of the signal was observed toward the end of each pump pulse, even without phase-matching. The change could be attributed to green-induced infrared absorption at the signal wavelength, caused by the parasitic SHG of the pump. This effect, also observed in RPE waveguides, set the limits on the gain and the pulse length.

Reverse proton exchanged waveguides were fabricated by proton exchange at  $185\ ^\circ\text{C}$  for 18.75 hours (soft-annealed depth of  $2.27\ \mu\text{m}$ ), followed by annealing at  $333\ ^\circ\text{C}$  for 15.67 hours and RPE at  $310.5\ ^\circ\text{C}$  for 17.53 hours. The final proton dose in the witness sample was  $1.08\ \mu\text{m}$ . The waveguides had mode filter widths of 2, 2.5 and  $3\ \mu\text{m}$ , 2-mm-long linear tapers, and mixing region widths ranging from 7 to  $18\ \mu\text{m}$ . The non-tapered single-mode waveguides had losses of  $0.13\ \text{dB/cm}$ . The taper insertion losses were  $1\pm 0.2$ ,  $0.4\pm 0.1$  and  $0.35\pm 0.1\ \text{dB/cm}$ , respectively, for the 2-, 2.5- and  $3\text{-}\mu\text{m}$ -wide mode-filters. The signal phasematching wavelengths for the three periods in the sample are plotted in Fig. 3.8 as a function of the mask channel width of the waveguides. Up to  $21.5\ \text{dB}$  of gain was observed with  $20\text{-}\mu\text{J}$ ,  $200\text{-ns}$  input pump pulses, for a waveguide width of  $14\ \mu\text{m}$ . This result suggested a conversion efficiency of  $\sim 1.5\ \%/W\text{-cm}^2$ , more than twice that of the APE waveguides. It was significantly lower than the expected  $10\text{-}12\ \%/W\text{-cm}^2$ , based on numerical modeling.

Even with the lower-than-expected efficiency, the observed gain of  $\sim 4.5\ \text{dB/cm}$  would be enough to reach the gain saturation regime in a 6-cm long amplifier with  $20\text{-mW}$  input signal. The most severe limitation of the first generation of devices for parametric amplification was the pump-induced reduction of the signal transmission. To address the problem, it was assumed that the effect was due to green-induced infrared absorption. The following design improvements were introduced in order to make a new set of waveguides that would meet the performance criteria for the optical preamplifier:

1. The high-temperature annealing was increased significantly, such that the effective diffusion length would increase by a factor of 1.5. The increase of the waveguide cross-section would increase the area of the fundamental mode of the pump by a factor of 1.5-2, reducing the efficiency of parasitic second-harmonic generation.

2. The broader index distribution of the new waveguide would confine the mid-IR idler

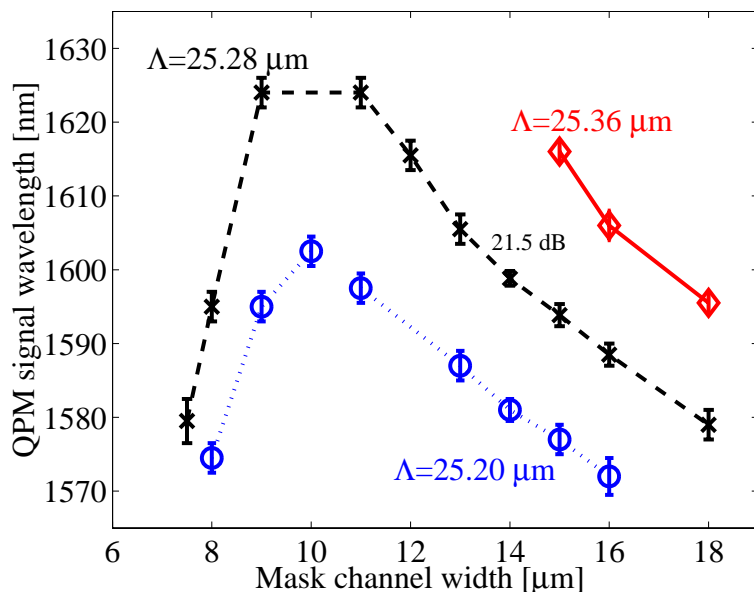


Figure 3.8: Signal phasematching wavelength of RPE waveguide OPAs versus mask channel width

no worse than the original design, since the idler mode was larger than the characteristic transverse dimensions of the original design. The DFG mixing efficiency was actually slightly improved, since the modes penetrated deeper below the dead layer due to the longer diffusion time.

3. Longer tapers were used in the improved design, with quadratic increase of channel width along the length of the taper. The quadratic widening lead to a more adiabatic change of the mode size along the taper. As a result, the insertion losses of the tapers were reduced to levels that were undetectable by the Fabry-Perot loss measurements, e.g, no more than 0.05 dB/taper. The better tapers improved coupling into the fundamental mode and eliminated coupling into higher order modes, which only contribute to parasitic processes, but not to the useful amplification process.

A periodically poled lithium niobate wafer was proton-exchanged in benzoic acid with  $\sim 0.5$  mol-% lithium benzoate at  $182^\circ\text{C}$  for 25.6 hours. The soft-annealed depth of proton exchange was  $2.4 \mu\text{m}$ . The waveguides were annealed at  $339.5^\circ\text{C}$  for 26.1 hours and reverse-proton exchanged at  $313^\circ\text{C}$  for 15 hours. The final proton dose was  $1.34 \mu\text{m}$ . The channel waveguides incorporated a 1.2-mm-long input mode-filter, 4.5-mm-long input and output

tapers, and a 56.7-mm-long periodically-poled mixing region. The channel width of the the mixing region varied between 13 and 17  $\mu\text{m}$  in a series of different waveguides. The propagation losses at 1.55  $\mu\text{m}$  ranged between 0.11 and 0.2 dB/cm for all three mode-filter widths used (2.75, 3 and 3.25 mm). All three mode-filter designs were single-mode at 1.55  $\mu\text{m}$ , while only the narrowest (2.75  $\mu\text{m}$ ) was single-mode at 1.064 mm. The 3- $\mu\text{m}$ -wide mode-filter was found to perform well even though it supported three pump modes. The higher order modes were much larger in size than the fundamental and good input mode-matching was adequate to ensure single-mode coupling. After characterization of the propagation losses, the output end of the waveguide chip was polished at 8 degrees with respect to the normal plane to the waveguide to suppress parametric oscillations.

Approximately 0.4 mW of the 0.68 mW coming from the L-band tunable laser were coupled into the waveguide. Figure 3.9 shows the room-temperature phasematching and gain observed for 0.5- $\mu\text{s}$  pump pulses with input energy of 7  $\mu\text{J}$ .

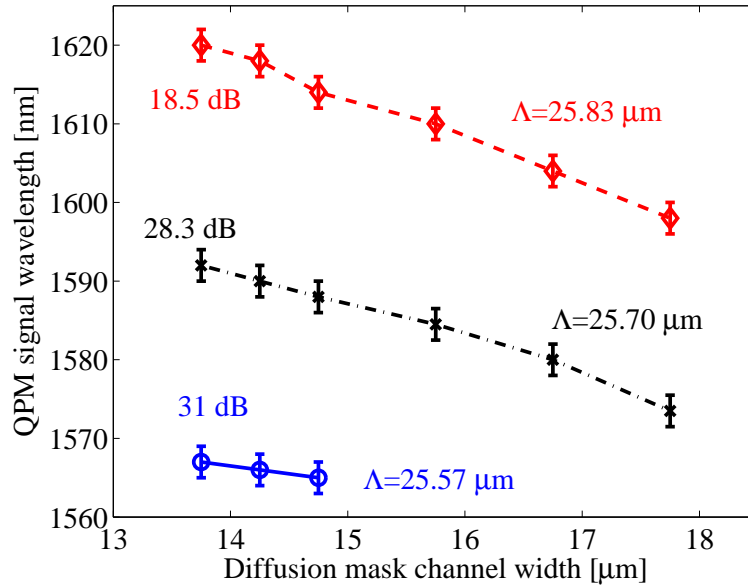


Figure 3.9: Signal phasematching wavelength and peak gain of RPE waveguide OPAs versus channel width

Non-critical phasematching with respect to waveguide width may occur for a mask channel width narrower than 13.75 mm. Assuming a lossless waveguide, the maximum observed gain of 31 dB corresponds to a normalized mixing efficiency of 9 %/W-cm<sup>2</sup>, close

to the numerically predicted value of 12 %/Wcm<sup>2</sup>. In addition, for a fixed waveguide width, the gain decreases as the signal wavelength increases. The efficiency of amplifying 1620 nm is half of that for amplifying 1567 nm. This is contrary to theoretical expectations disregarding losses, that suggest that the mixing efficiency for 1620-nm amplification should be 20-30% higher, due to a better confinement of the idler. The likely explanation for this experimental observation is that the wings of the OH<sup>-</sup> absorption peak (centered at 2.86 μm), significantly affect the 3101-nm idler in the case of 1620 nm amplification, reducing the efficiency. In the case of 1567-nm amplification, the idler is at 3316-nm and is much less absorbed. In the high-gain regime, the losses at the idler have a relatively small effect on the observed gain. For instance, if the gain without loss would be 40 dB and the idler losses are 10 dB, then the gain in the presence of idler loss would be 35 dB. This means that normalized conversion efficiency numbers extracted from gain only have a meaning if full analysis of the gain is performed, including estimates of the idler losses. Pump and signal losses are also important, but it is assumed here that they are much smaller than the idler losses.

For higher gain than 30 dB and longer pulses, higher pump-pulse energy was used. In order to suppress photorefractive effects in the waveguides, the operating temperature of the frequency mixer would have to be increased.

The dependence of signal QPM wavelength on temperature, measured between 20 and 110 °C, is shown in Fig. 3.10. The the pump is at 1064 nm, and the QPM period is 25.57 μm.

The fitting curve is given by the equation:

$$\lambda_s^{QPM} = \lambda_0 + 0.367(t - t_0) + 0.00194(t - t_0)^2, \quad (3.3)$$

where  $\lambda_0=1567.44$  nm and  $t_0=25$  °C. Over the 90-degree range in temperature, the QPM wavelength changes by 46 nm ( $\sim 200$  cm<sup>-1</sup>).

For the high-energy experiment, a waveguide with a period of 15.57 μm and channel width of 15 μm was used at a temperature of 60 °C. This placed the QPM wavelength around 1568 nm, on the lower side of the tuning range of the signal laser. The unamplified signal power was 0.4 mW. The 1-μs pump pulses were near flat-top, but had sloped sides, so the amplified signal pulses were slightly shorter (0.83 μs). The gain in dB as a function of the square root of pump power coupled in the waveguide is shown in Fig. 3.11. The

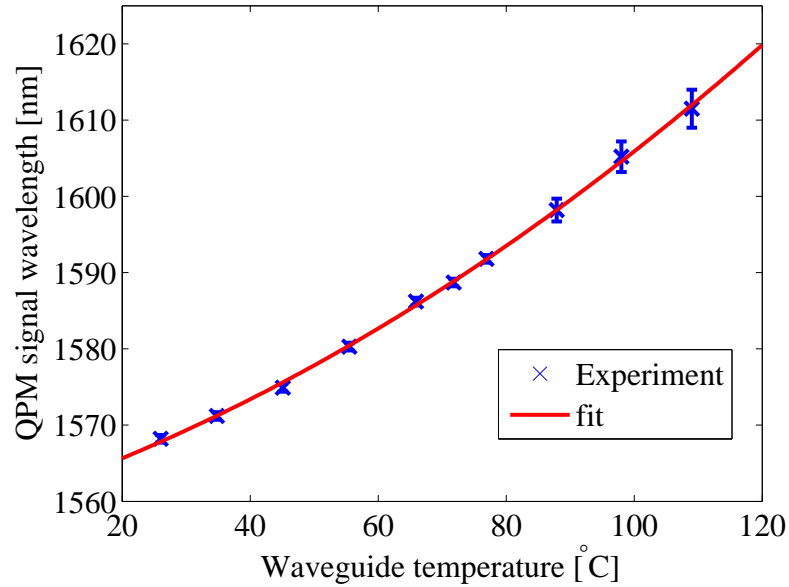


Figure 3.10: Temperature tuning of the phasematching signal wavelength of a waveguide OPA

gain starts to saturate beyond 40 dB when the signal energy becomes over  $3 \mu\text{J}$ . The  $5 \mu\text{J}$  of pump already converted to signal, represent over 20 % of the coupled pump energy at that point. A maximum gain of 45 dB was observed, with  $70 \mu\text{J}$  of pump on the waveguide input and  $31 \mu\text{J}$  coupled inside the waveguide. The input pulse energy was not increased further, in order to avoid input-surface damage.

The improved waveguide OPA design satisfied the requirements for the waveguide pre-amplifier for remote sensing, with capability to provide pulses with energy approaching  $10 \mu\text{J}$  and pulse lengths of order  $0.8 \mu\text{s}$ . Green-induced infrared absorption was not a problem in this design at the power levels of operation.

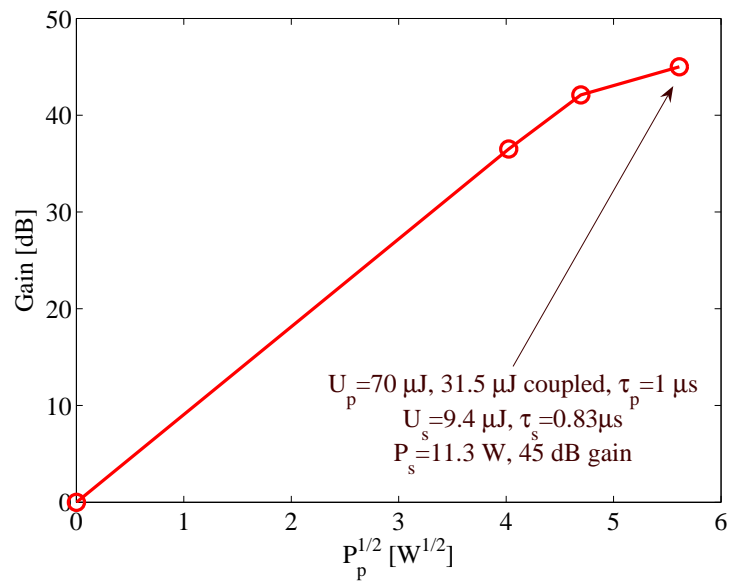


Figure 3.11: Gain of the waveguide OPA versus square root of peak pump power in the pulse

## Chapter 4

# Vapor-transport equilibrated near-stoichiometric lithium niobate

This chapter describes the fabrication and material properties of lightly MgO-doped vapor-transport equilibrated (VTE) lithium niobate (LN) that is resistant to photorefractive damage (PRD) and green-induced infrared absorption (GRIIRA). A brief description of the accepted model of the photorefractive effect in lithium niobate is given first, to provide a basis for understanding PRD-reduction by stoichiometry control.

### 4.1 Photorefractive effect in lithium niobate

Consider a uniaxial ferroelectric crystal, such as  $\text{LiNbO}_3$ , illuminated by a visible laser beam propagating in a direction orthogonal to the ferroelectric  $z$  axis. If the crystal is photorefractively sensitive, its interaction with the light will cause photorefractive damage to the crystal with a resulting distortion of the beam. The physical mechanism is described below.

According to the currently accepted model [38, 160], the photorefractive effect in LN starts with photoelectron generation, followed by charge separation that leads to the formation of a space charge field (SCF). The SCF causes refractive index change via the electro-optic effect. The photoelectrons responsible for the formation of the SCF are generated by the absorption of visible-light photons at impurities, such as Fe, and possibly, at intrinsic defects. Due to the asymmetric local potential near the absorbing impurities, the photoelectrons are ejected asymmetrically along the  $c$ -axis of the uniaxial crystal, leading to

a nonzero net current (photogalvanic current). Taking the crystal conductivity into account, the current density in the medium under illumination can be found from the constitutive relation:

$$\mathbf{j} = \sigma \mathbf{E} + \kappa I \hat{\mathbf{z}} \quad (4.1)$$

where  $\sigma$  is the conductivity,  $\kappa$  is the Glass coefficient that determines the photogalvanic sensitivity of the material,  $I$  is the light intensity and  $\hat{\mathbf{z}}$  is the unit vector of the ferroelectric axis of the crystal. The first term in Eq. 4.1 represents the drift current density, and the second term represents the photogalvanic current density,  $\mathbf{j}_{pg}$ . The conductivity can be represented as the following sum:

$$\sigma = \sigma_d + \sigma_{ph} \quad (4.2)$$

where  $\sigma_d$  is the dark conductivity, and  $\sigma_{ph}$  is the photoconductivity, present due to the illumination. The resulting charge separation leads to the formation of the SCF. Steady state with  $\mathbf{j} = 0$  can be reached when the drift current driven by the SCF balances the photogalvanic current. The steady-state space-charge field,  $E_{SC} \hat{\mathbf{z}}$ , is therefore inversely proportional to the crystal conductivity [38, 160]:

$$E_{SC} = -\frac{j_{pg}}{\sigma_d + \sigma_{ph}} \quad (4.3)$$

The SCF is usually reduced at higher crystal temperatures, since the resulting increase in hopping mobility enhances both  $\sigma_d$  and  $\sigma_{ph}$ . This is the traditional method for reducing the photorefractive effect in congruent lithium niobate (CLN).

In the simplest case of optical absorption that is linear with light intensity and carrier lifetime that is independent of intensity, the photogalvanic current ( $\mathbf{j}_{pg} = \kappa I \hat{\mathbf{z}}$ ) and the photoconductivity ( $\sigma_{ph} = \beta I$ , where  $\beta$  is the specific photoconductivity) are both proportional to the intensity. In the limit of high intensity, the photoconductivity dominates the dark conductivity and the space-charge field saturates:

$$E_{SC} = -\frac{\kappa I}{\sigma_d + \beta I} \xrightarrow{\beta I \gg \sigma_d} E_{SSC} \equiv -\frac{\kappa}{\beta}, \quad (4.4)$$

where  $E_{SSC}$  is the saturated space-charge field. Note that the photogalvanic current in CLN grows slightly super-linearly with intensity, so the SSF does not truly saturate [161]. It is therefore worth mentioning that the ‘‘high intensity’’ characterization of CLN and SLN samples, described in this chapter, uses laser beam intensities of order  $10^4$  W/cm<sup>2</sup>.

If the space-charge field is parallel to the ferroelectric crystal axis, the change in the extraordinary refractive index generated by the SSF  $E_{SC}$  via the electro-optic effect is given by

$$\Delta n_e = -\frac{1}{2}n_e^3 r_{33} E_{SC} \quad (4.5)$$

A common situation with intense laser beams is that the space-charge field in the center of the beam quickly reaches saturation, while the space-charge field in the periphery is lower. This causes a nonuniform distribution of  $\Delta n_e$  across the beam, with most of the change occurring in the region of the periphery where  $\sigma_{ph} \approx \sigma_d$ . The space-charge field in optical grade congruent LN is about 1.5 kV/mm when ordinary-polarized green light (514 nm) with intensity of  $\sim 10^4$  W/cm<sup>2</sup> propagates orthogonal to the c-axis. This would lead to a phase difference of  $\pi$  between the bright region of the beam and the dark periphery after only 1.1 mm of propagation, leading to defocusing of the beam along the c-axis. The characteristic time for the new beam pattern to appear is the dielectric relaxation time, which is inversely proportional to conductivity, and therefore, inversely proportional to the light intensity. For green-light intensity of order  $\sim 10^4$  W/cm<sup>2</sup>, the pattern appears within a few seconds. If we want to limit the photorefractive phase difference to  $\pi/10$  in a 1-cm-long LN crystal, the saturated space charge field  $E_{SSC}$  must be no larger than 15 V/mm.

## 4.2 PRD-suppression via doping and stoichiometry control

In order to eliminate the PRD in lithium niobate, the ratio  $\kappa/\beta$  should be significantly reduced. In the simplest case, the carriers contributing to both the photogalvanic current and the photoconductivity are generated by absorption at the same defects, so that it is not possible to improve the ratio  $\kappa/\beta$  by reducing the density of this defect, e.g. Fe. The specific photoconductivity  $\beta$  can be raised by lowering the density or the effective cross-section of the dominant traps for photocarriers, thereby increasing the carrier lifetime and thus the photoconductivity. For example, the photoconductivity in LiTaO<sub>3</sub>, a crystal similar to LiNbO<sub>3</sub>, has been shown to increase in crystals with compositions approaching stoichiometric, in correlation with the decrease in the density of Ta antisites [48, 49]. This correlation suggests proportionality between antisite density and trap density.

A common approach for solving the PRD problem in LiNbO<sub>3</sub> is to increase the photoconductivity by eliminating the Nb<sub>Li</sub><sup>4+</sup> antisites. One established implementation [44, 45]

involves doping of the congruent crystal with an ion ( $\text{Mg}^{2+}$ ,  $\text{Zn}^{2+}$ , or  $\text{In}^{3+}$  [162]) that displaces the  $\text{Nb}_{\text{Li}}^{4+}$  from the lithium sites. Measurements of the  $E_{SSC}$  generated by 514-nm light in two different samples of commercial optical grade 5 mol-% MgO:LN (Yamaju Ceramics) show identical results of 2.6 V/mm in both cases. In addition, the GRIIRA of 5% MgO:LN is significantly reduced compared to CLN [43]. GRIIRA and PRD seem to be affected in the same way when the crystal composition is changed with the purpose of reducing PRD.

The second way to increase the photoconductivity is to remove the antisites by producing near stoichiometric crystals with Li to Nb concentration ratio very close to 50:50 [48, 49]. When the antisites are associated with the dominant trapping defect, the carrier lifetime is approximately proportional to  $1/x$ , where

$$x = 0.5 - \frac{[\text{Li}]}{[\text{Li}] + [\text{Nb}]} \quad (4.6)$$

is the deviation from the stoichiometric composition. Clearly, most of the increase in carrier lifetime occurs when  $x$  approaches very close to 0. This is the requirement for suppression of PRD. Gopalan et al. [62] showed that the coercive field of  $\text{LiTaO}_3$  is proportional to  $x$ . The linear dependence of the coercive field on  $x$  provides a relatively easy way of estimating  $x$  by measuring the coercive field. The photoconductivity is expected to depend on  $x$  as

$$\sigma_{ph} = \frac{\sigma_{ph}^{congr}}{1 - \frac{\Delta - x}{\Delta + r\Delta_s}} \quad (4.7)$$

where  $\sigma_{ph}^{congr}$  is the photoconductivity of CLN,  $\Delta$  is the Li-deficiency of the congruent crystal,  $\Delta_s$  is a constant representing a small concentration of traps other than Nb antisites, that would limit the photoconductivity of a stoichiometric crystal with  $x = 0$ , and  $r$  is their trapping efficiency relative to that of the Nb antisites. Note that Eq. 4.7 is only valid inside the region  $0 \leq x \leq \Delta$ .

### 4.3 PRD-suppression in lightly-MgO-doped SLN

The above model explains very well the elimination of PRD by stoichiometry control in lithium tantalate [49]. On the other hand, near-stoichiometric lithium niobate (SLN) does

not conform to the model very well. Non-doped SLN can be either more or less photorefractive than CLN, depending on the SLN fabrication method [163, 164, 165]. The only reported non-doped SLN that is less photorefractive than CLN, is grown from a top-seeded solution (TSS) [163]. None of the non-doped compositions, however, has low enough photorefractive response to be used in practical applications involving high-intensity visible light.

Combining near-stoichiometric composition with 1 mol-% MgO-doping allows to suppress PRD and GRIIRA in crystals grown by the double-crucible Czochralski method [47]. It was recently demonstrated that near-stoichiometric crystals, obtained by vapor-transport equilibration of 1 mol-% MgO-doped CLN crystals, are resistant to PRD [166]. A more careful examination showed that unlike non-doped VTE-SLN, the 1 mol-% MgO-doped VTE crystals had light-scattering centers after the VTE process. Investigation of VTE of crystals with 1-mol-% and lower doping levels is described in the rest of the chapter.

#### 4.4 Fabrication method

VTE of LN [56, 61, 58] consists of enclosing CLN samples in a crucible with Li-rich two-phase pre-reacted LN powder and heating them to temperatures in the range 1000-1150 °C, adequate for significant vapor transport of Li<sub>2</sub>O and solid-state diffusion of Li into the crystal. The two crystalline phases in the powder are the LiNbO<sub>3</sub> phase and the Li<sub>3</sub>NbO<sub>4</sub> phase. The Li<sub>2</sub>O chemical potential of the powder is independent of powder composition throughout the two-phase region (Li:Nb ratio between 50:50 and 75:25), making the VTE process insensitive to powder composition [56]. In the present studies, a reacted mixture of approximately 60% Li<sub>2</sub>O and 40% Nb<sub>2</sub>O<sub>5</sub> is used as the Li source. All samples are cleaned with diluted solutions (10-15%) of hydrochloric and nitric acid and rinsed with acetone and 2-propanol prior to VTE. For the equilibration process, some samples are mounted on a small platinum fixture above the powder, while others are buried in the powder. The samples buried in the powder usually require shorter VTE time. During VTE, the weight of the samples increases as a result of the Li indiffusion. The weight gain saturates when a sample is equilibrated. For buried 0.5-mm thick samples, the typical time required for weight-gain saturation (and suppression of the PRD) is approximately 200, 350 and 600 hours at 1050 °C for 1, 0.5, and 0.3 mol-% MgO:LN, respectively. Qualitative observations suggest that for samples equilibrated above the powder, the saturation time increases with the total volume of the samples due to inadequate evaporation rate from the powder, i.e. the

kinetics are evaporation-rate limited rather than diffusion limited. When the total sample volume is small, the saturation time is similar to that for the buried samples. Higher temperature allows for shorter VTE time. After VTE, the large ( $+z$  and  $-z$ ) surfaces of the samples are polished to remove any low-quality layers formed on the surface during VTE. It was found that the polishing of a VTE MgO-doped sample makes periodic poling much less challenging.

The effects of VTE temperature and MgO-doping concentration on the formation of scattering centers were explored. It was found that higher VTE temperature and higher MgO-doping levels lead to more prominent and more concentrated scattering defects. The observed concentration of scattering defects was higher in the 1 mol-% and 0.5 mol-% MgO:SLN processed at higher temperature. Therefore, the temperature range 1090 to 1030 °C was chosen for the equilibration of samples to be used in optical experiments. Using an optical microscope it was also observed that compared to the 1 mol-%-doped samples, crystals with 0.5 mol-% doping developed fewer and finer scattering centers during VTE, while 0.3 mol-%-doped crystals did not form any. After equilibration of a full 76-mm-diameter 0.5-% MgO-doped wafer for 115 hours at 1080, 50 hours at 1065 and 30 hours at 1050 °C, scattering defects were only observed in a 0.5-cm-wide band around the periphery of the wafer, while the photorefractive effect was suppressed throughout. It was found that using a lower VTE temperature ( $\leq 1050$  °C) in combination with a timely termination of the VTE process allowed the obtaining of scattering-free 0.5 mol-% MgO-doped material resistant to PRD.

When the VTE time is very long, the powder sinters and sometimes the buried samples with lower MgO doping (especially 0.3 mol-%-doped and non-doped) develop twins during the process. Therefore, the VTE process for the buried 0.3 mol-% samples is usually split into 2–4 cycles, stirring the powder between cycles to avoid significant sintering. Besides decreasing the VTE time, burying the samples in the powder helps maintain the flatness of large area samples during VTE.

## 4.5 Material characterization

### 4.5.1 Photorefractive properties

The experimental setup and procedure for measurement of the saturated space-charge field are described in Ref. [49]. A schematic diagram of the used fixture and illumination

arrangement is shown in Fig. 4.1. An argon-laser beam with optical power of  $\sim 0.7$  W at 514 nm is focused into a spot with a diameter of  $\sim 80$   $\mu\text{m}$ , propagating along the c-axis of the z-cut sample. The  $+z$  and the  $-z$  faces of the sample are contacted with LiCl liquid electrodes. The fixture containing the electrodes is made of quartz, with small holes that allow wire contacts to be inserted into the LiCl-water solution. Rubber o-rings or wax can be used to seal the two sides of the crystal electrically. The photogalvanic current and photoconductive current are measured using a picoammeter.

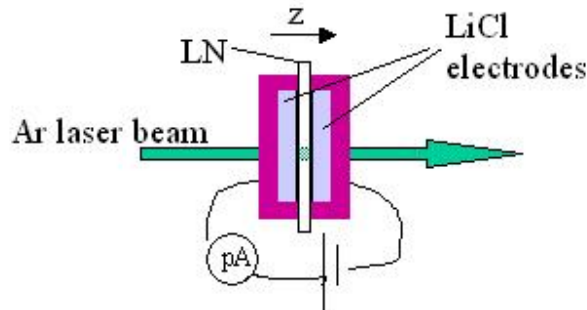


Figure 4.1: A schematic diagram of the photocurrent measurement

To measure the photoconductivity, voltage is applied along the c-axis in addition to the laser beam, and the resulting current is measured. The photoconductive current can be determined by subtracting the photogalvanic current and the dark current from the total current, measured when both the voltage and the light beam are present. The photogalvanic current is measured when only the light beam is present, while the dark current is measured when only the voltage is present. The photoconductivity is determined by dividing the photoconductive current by the applied electric field. The photocurrents have been assumed proportional to the optical intensity and electric field at the laser power and voltages (10-100 V) applied. This assumption was tested and confirmed on two MgO-doped VTE crystals.

Note that for experimental convenience with z-cut wafers, the photogalvanic current and photoconductivity generated only by ordinary-polarized light were measured. In the most often used quasi-phasematching scheme in LN, all optical fields have extraordinary polarization in order to take advantage of the largest component of the tensor of the second-order nonlinear susceptibility. The described measurement of the saturated space-charge field provides quantitative information about the photorefractive damage caused by an

ordinary-polarized beam. The measured space-charge field is used only as a qualitative indicator for low or high resistance to PRD for any other polarization. Assuming that the photogalvanic effect and the photoconductivity depend on polarization only weakly, the SCF measured with ordinary polarization would provide a good estimate of the photorefractive sensitivity to light with any polarization. To confirm the SCF-based conclusions for extraordinarily polarized light, a beam-fanning experiment can be performed, in which an extraordinarily polarized green beam propagates along the  $x$  crystalline axis as in a typical quasi-phaseshifted second harmonic generation scheme. If significant photorefractive effect is present, the beam will be distorted after a short exposure time.

A study was performed of the dependence of the SCF on the stoichiometry of the crystal after VTE, using six MgO:LN samples with a doping level of 1 mol-%. Different samples were heat-treated for different time intervals above the lithium-rich powder. The weight gain during VTE, the photoconductivity, and the saturated space-charge field were measured and compared to expectations based on the described model. The results for the specific photoconductivity  $\beta$  from Eq. 4.4 are presented in Fig. 4.2. The horizontal extent of the plus signs representing the experimental points is comparable to the experimental error of the weight gain measurement. The dash-dotted line represents a typical theoretical expectation for the dependence of the photoconductivity on the weight gain according to Eq. 4.7, where the weight gain equals  $\Delta - x$ , with  $\Delta = 1.174$  mol-% determined from the weight gain saturation. The constant  $r\Delta s$  is assumed to be 0.001 mol-%. The values of the constants were picked somewhat arbitrarily, serving merely to illustrate the qualitative agreement of the experimental results with the assumed physical picture.

The deviation of the rightmost data point from the functional form of Eq. 4.7 may be related to the development of scattering centers after the saturation of the crystal with  $\text{Li}_2\text{O}$ . These defects will have a different composition than the stoichiometric crystal, possibly allowing for additional weight gain beyond what is necessary for the displacement of all antisites. In addition, the measured photoconductivity data represent averaged values over the crystal thickness. This may have an effect on all data points in Fig. 4.2. Since the surface layer of the crystals was not polished before the measurements, error due to different surface layers may have been incorporated. In addition, Eq. 4.4 accounts for the MgO-doping simply by a change of the expected saturated weight gain  $\Delta$ . Such an assumption may be an oversimplification of the detailed physical picture.

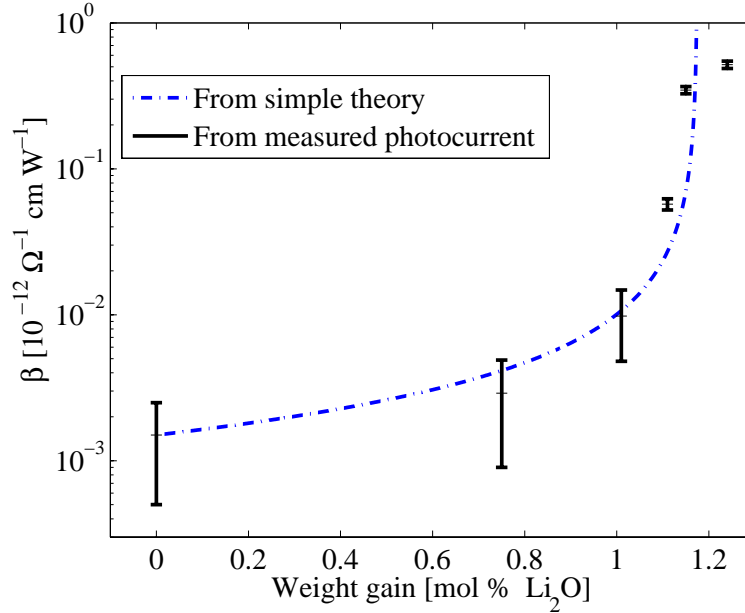


Figure 4.2: Specific photoconductivity versus VTE weight gain

The results for the saturated SCF are presented in Fig. 4.3. Unlike the case of VTE-lithium tantalate [49], significant changes of the photogalvanic current were observed in non-doped and lightly MgO-doped LN, as a function of the VTE time and the resulting crystal composition. The photogalvanic current in MgO:LN decreased by more than 2 orders of magnitude for the sample with the largest weight gain. Furukawa et al. [167] observed a similar reduction in photogalvanic current, but with increasing MgO-doping level of TSS-grown SLN. The dash-dotted curve in Fig. 4.3 represents a theoretical curve with the parameters used for the photoconductivity plot from Fig. 4.2, assuming that the photogalvanic current does not change with weight gain. The circles represent the calculations with the same values for the photoconductivity, but with the photogalvanic current changing with weight gain, as measured.

The origin of the change in photogalvanic current with stoichiometry after VTE has not been investigated, but it is likely to be complex. In some 1- and 0.5-% samples that underwent longer VTE processing, the photogalvanic current even changed sign. Typically, the photogalvanic current has the same sign as the pyroelectric current spike observed during the initial heating of the sample at the beginning of the laser beam exposure. If the

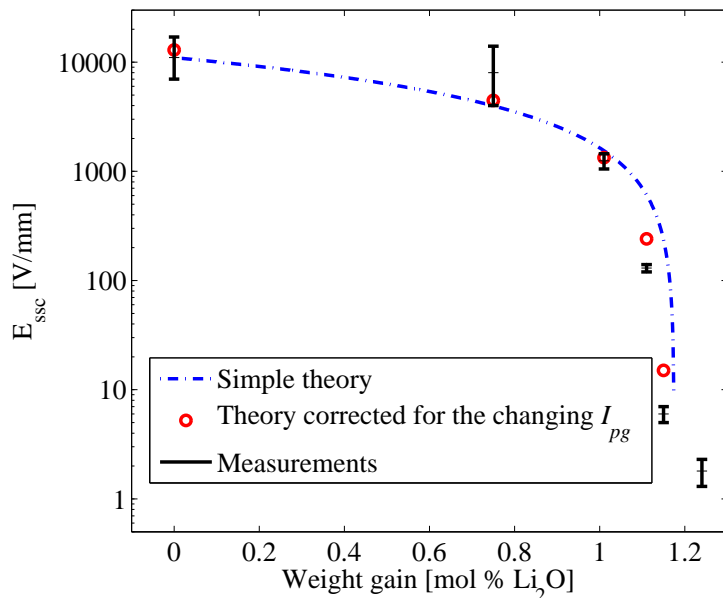


Figure 4.3: Saturated space-charge field versus VTE weight gain

photogalvanic current can change sign with changing crystal stoichiometry in MgO-doped crystals, there may be two kinds of crystal defects that have contributions of opposite signs to the photogalvanic current, and as the relative density of these defects changes with VTE processing, the net photogalvanic current changes accordingly. Note that the photogalvanic current, generated by 514-nm green light, can be adjusted to vanish in 1- and 0.5-% MgO:SLN with an appropriate VTE process.

In a similar way to the case of 1 mol-% MgO-doped crystals, the saturated space-charge field of 0.5 mol-% MgO:LN dropped to  $0 \pm 0.1$  V/mm after equilibration for 125 hours at 1090 °C, followed by 35 hours at 1070 °C, and 48 hours at 1050 °C (a total of  $\sim 210$  hours, equivalent to  $\sim 350$  hours at 1050 °C). Equivalent hours for VTE at any temperature can be calculated using the Arrhenius law with an activation energy of 2.8 eV.

The saturated space-charge field of 0.3-% MgO:LN also decreased as the samples were enriched in Li<sub>2</sub>O via VTE. The value of  $E_{SSC}$  stabilized to some minimum after  $\sim 600$ – $700$  hours at 1050 °C. For a sample equilibrated above the powder, the observed minimum value of the  $E_{SSC}$  was 10 V/mm after a total of  $\sim 700$  hours. With further VTE, a slow increase of the photogalvanic current was observed in parallel with a slow increase in the

photoconductivity, such that the value of  $E_{SSC}$  remained between 10 and 11 V/mm even after 1100 hours at 1050 °C. The sample acquired a faint yellow color indicating increased absorption in the blue region of the spectrum. For samples equilibrated in the powder, values of  $E_{SSC}$  as low as 1 V/mm were measured. For example, a sample with  $E_{SSC} = 1.6$  V/mm had undergone two VTE-treatments: VTE 1, consisting of 98 hours at 1080 °C, 43 hours at 1065 °C, and 29 hours at 1050 °C, followed by VTE 2, consisting of 119 hours at 1090 °C, 41 hours at 1070 °C, and 52 hours at 1050 °C. The low saturated space-charge field proved repeatable (1-2 V/mm) with repeating approximately the same sequence of VTE-steps. The samples acquired very faint coloration. Scattering defects were not seen with an optical microscope.

A qualitative measurement of the PRD-resistance of VTE-0.3 mol-% MgO:SLN was performed by polishing two opposite edges of the z-cut wafer and sending a beam from an argon laser along the x-crystalline axis. A CLN sample was prepared and measured the same way for comparison. The beam exiting the crystal was projected onto a dark screen and the beam pattern on the screen was photographed. Images of the experimental results are shown in Fig. 4.4.

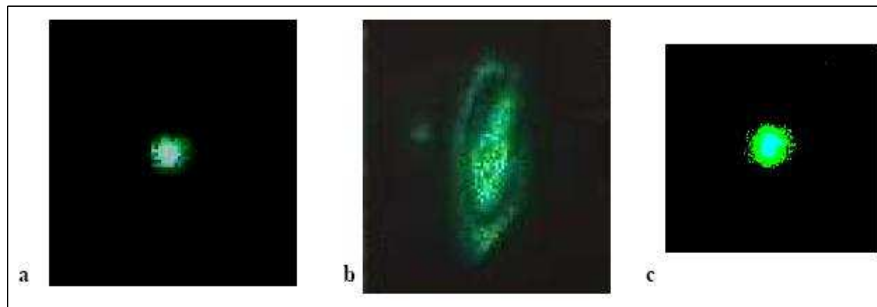


Figure 4.4: A beam-fanning comparison between CLN and VTE- 0.3 mol-% MgO:SLN. A projection of the laser beam on a dark screen after passing through a 12-mm long crystal is imaged. a)- CLN, P=90 mW, beginning of exposure; b) CLN, P=90 mW, 3 s after beginning of exposure; c) 0.3% MgO:SLN, P=600 mW, 600 s after beginning of exposure.

By comparing images a) and b), it is seen that in CLN photorefractive effect distorts the beam within seconds at 90 mW of laser beam power. In the MgO-doped VTE-SLN sample, no beam fanning was observed at the maximum available power of 600 mW (image c)).

Experiments with VTE of non-doped LN showed that crystals equilibrated at higher VTE temperature (for instance, 1100 °) had higher photogalvanic current and saturated space-charge field than congruent crystals. Typical values of  $E_{SSC}$  ranged from 2000 to 3000 V/mm, with higher values corresponding to higher VTE temperature. All samples were equilibrated until no additional weight gain was occurring at the particular equilibration temperature. Some samples equilibrated at lower temperature had lower  $E_{SSC}$  than CLN. The lowest saturated space-charge field measured in non-doped VTE-SLN was 1000 V/mm, for a sample equilibrated at 1000 °C. At such lower temperature, the equilibration times become prohibitively long, over 1000 hours. The same samples had the lowest coercive field, 900-1000 V/mm, of all non-doped VTE-SLN samples, indicating that their composition was closest to stoichiometric ( $x \approx \Delta/20$ ). The lower coercive field obtained with lower VTE temperature is consistent with observations by Polgár et al.[52] that the Li-rich phase boundary is curved, and moves toward stoichiometry at lower temperatures. Some SLN grown by the TSS-method using a  $K_2O$  flux, was closer to stoichiometric, with a coercive field of 200 V/mm [51].

#### 4.5.2 Material absorption

The faint-yellow appearance of VTE crystals was investigated using transmission measurements. Normally, crystals with higher MgO-content obtained more prominent yellow appearance after VTE than crystals with lower MgO-content. The transmission spectra of two 1 mol-% MgO-doped samples were measured, to determine the amount of absorption causing the light yellowish color after VTE. The first sample was congruent. The second sample was cut from the same wafer as the first, but after that it was vapor-transport equilibrated and polished. The spectrophotometer beam propagated across the thin dimension of the  $z$ -cut samples, along the  $c$ -axis. Absorption of ordinary-polarized light was measured. Fig. 4.5 shows the comparison of the transmission of 1-% MgO: CLN and VTE-1-% MgO:SLN. The spectral linewidth of the spectrophotometer was fixed at 1 nm for both scans. The samples were 1 and 0.9-mm thick, respectively. The transmission of the SLN sample is slightly smaller than that of the CLN sample in the blue and violet portion of the visible spectrum. The maximum difference of  $\sim 0.5$  % occurs at 400 nm, amounting to an absorption coefficient difference of  $\sim 0.05$   $\text{cm}^{-1}$ . At 500 nm the difference is within the measurement error of  $\pm 0.2\%$  ( $0.02$   $\text{cm}^{-1}$ ).

The estimated extinction on the blue side of the visible spectrum seems significant.

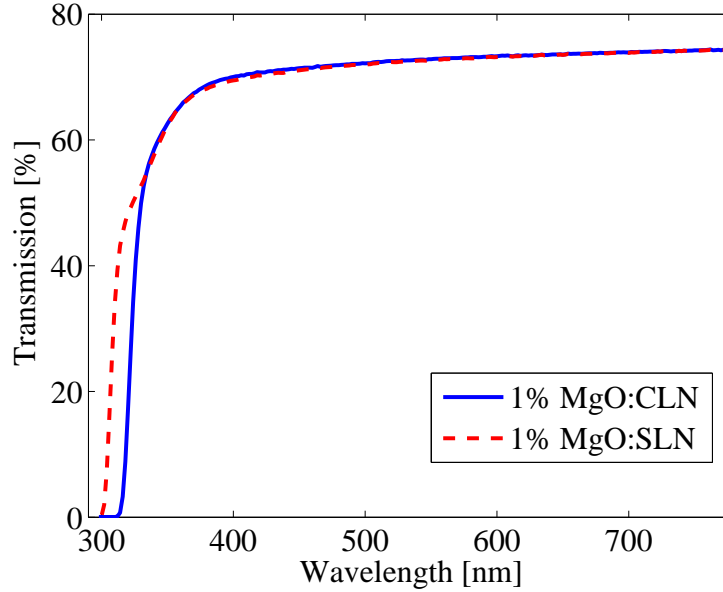


Figure 4.5: Optical transmission spectra of 1 mol-% MgO:CLN and VTE-MgO:SLN

On the other hand, intense focused Watt-level laser beams can propagate through the crystal without damaging it thermally, as will be shown in the next chapter. This apparent paradox is due to the transient nature of this absorption. With the help of the photocurrent measurements, described in the previous subsection, it was determined that the absorption in VTE-MgO:SLN was bleached over time periods of minutes to seconds when the green-light intensity was of order  $10^4$ – $10^5$  W/cm<sup>2</sup>. This conclusion was made by observing the magnitude of the pyroelectric spike occurring at the beginning of laser exposure, when the exposed area of the crystal was heated to a higher temperature by the absorbed light. This spike was reduced significantly after seconds to minutes of exposure of the same crystal location.

The absorption band edge in the SLN sample is blue-shifted by 14 nm compared to the CLN one. This advantage may be exploited for UV generation if a method is developed to remove the absorption shoulder in the UV, caused by crystal defects. A way to affect the absorption of CLN in the visible and UV by electrochemical oxidation has been recently published [168]. Preliminary experiments performed with the help of Romain Gaume confirmed the feasibility of the method for manipulating the absorption of CLN and

SLN, although the method seemed more effective in CLN, where the large number of Li vacancies improved the high-temperature ionic diffusivity and conductivity, utilized in the electrochemical oxidation process.

Volodymir Kondilenko used photothermal common-path interferometry [169] to make measurements of the absorption of intense extraordinary-polarized light at 1064 nm and 514 nm in VTE-SLN. In addition, measurements of the green-induced infrared absorption at 1064 nm caused by a 514 nm pump were made. The measured sample was the 0.3-mol-% MgO:SLN crystal used in the experiment from Fig. 4.4 c). It had a very low saturated space-charge field of 1.6 V/mm. The results were qualitative and showed that the absorption of 0.3% MgO:CLN at 514 nm and 1064 nm was comparable to that of 5 mol-% MgO:CLN from Yamaju Ceramics. The GRIIRA measurement did not detect any increase in the infrared absorption at 1064 nm when a 0.5-W green pump with a diameter of 47  $\mu\text{m}$  was present. Any GRIIRA effects must have been below the noise limit, equal to  $\sim 3\%$  of the infrared absorption at 1064 nm. The absolute values of the absorption and GRIIRA coefficients were not measured due to the lack of a calibrated sample. Only measurements relative to a high-quality 5 mol-% MgO:CLN sample were made.

### 4.5.3 Dispersion of the extraordinary refractive index of SLN

The extraordinary refractive index of 1-%, 0.3-% and non-doped VTE-SLN was measured at several wavelengths between 457.9 and 1550 nm using a prism coupler. The values of the prism ordinary and extraordinary index at different wavelengths, used in the computer program that calculates the propagation constant based on the incidence angle, were adjusted such that measurements of the ordinary and extraordinary index of CLN follow the Sellmeier equation by D. Jundt [145]. The results of the SLN measurements are shown in Fig. 4.6, along with the Sellmeier fitting curve.

It is seen that the extraordinary refractive index of VTE-SLN does not depend on the MgO-doping concentration. In fact, a VTE experiment was made with 5 mol-% MgO:LN, and after the weight gain saturated, that crystal had the same refractive index at 633 nm as VTE-SLN with low or no doping. For the Sellmeier fit, one representative data point was calculated at each wavelength as an average of the measurements of the different SLN crystals, which agreed within 0.0005. The continuous Sellmeier curve that fits the

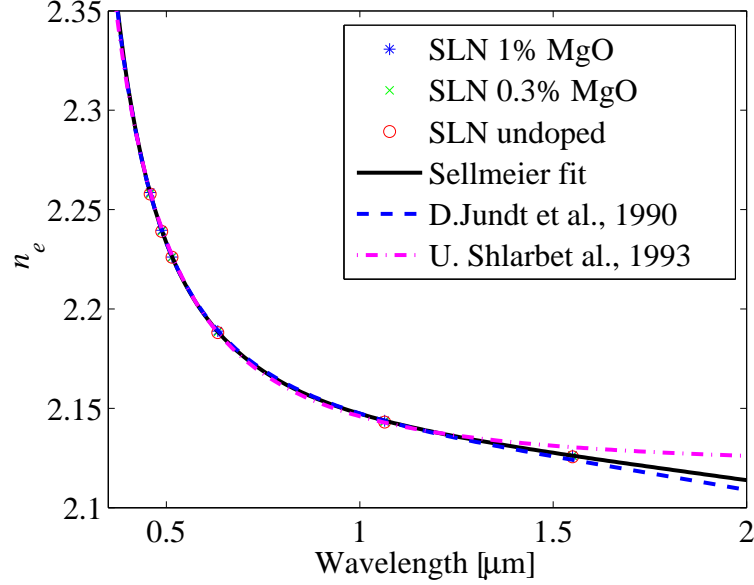


Figure 4.6: Dispersion of the extraordinary refractive index,  $n_e$ , of VTE-SLN

experimental data is given by the equation

$$n_e(\lambda) = \sqrt{4.5355 + \frac{0.09349}{\lambda^2 - 0.2137^2} - 0.02273\lambda^2} \quad (4.8)$$

where  $\lambda$  is measured in micrometers. The fit line lies between the curves from two earlier Sellmeier equations [59, 170] in the region beyond 1.3  $\mu\text{m}$ . The earlier equations were fits to data extending only to 1.064 and 1.2  $\mu\text{m}$ , respectively. The dashed line represents the Sellmeier equation of VTE-SLN by D. Jundt et al.[59], calculated at room temperature. The dash-dotted line represents the Sellmeier equation by U. Schlarb and K. Betzler [170] for SLN with  $\text{Li}_2\text{O}$ -molar concentration of 49.85 %.

The above material characterizations of VTE-SLN show that it is a promising material for frequency-conversion of intense laser beams, including the visible region of the spectrum. The measured dispersion of the extraordinary index of MgO-doped SLN is adequate the design of QPM structures for optical frequency mixing in which all interacting beams are polarized along the ferroelectric axis of the crystal. Some experiments with periodic poling of VTE-MgO:SLN and second harmonic generation of intense green light are described in the next chapter.

## Chapter 5

# Periodic poling of MgO-doped near-stoichiometric LiNbO<sub>3</sub> and high-power green light generation at room temperature

In this chapter, periodic poling of vapor transport equilibrated LiNbO<sub>3</sub> with low MgO doping ( $\leq 0.5$  mol-%) is described. An efficient process for periodic poling with LiCl-solution electrodes at room temperature, using baked photoresist as a patterned dielectric on one crystal surface, is developed for periods as short as 9.6 microns for 0.5 mol-% and 7 microns for 0.3 mol-% MgO-doped VTE:LN. For the same period, the quality of periodic poling improves as the MgO concentration is lowered.

Second harmonic generation of 532-nm radiation in periodically poled lightly-MgO-doped VTE-SLN has been reported [171] at a power level of 120  $\mu$ W, which is not enough to verify significant resistance to PRD. More recently, Chen et al. [172] described SHG of 43 mW of 400-nm violet light by third-order QPM in periodically poled 1.8 mol-% MgO-doped VTE SLN with a period of 7.8  $\mu$ m.

Stable single-pass room-temperature SHG of Watt-level continuous-wave 532-nm radiation in periodically poled VTE-SLN with 0.3 mol-% of MgO-doping is described at the end of this chapter.

## 5.1 Electric-field poling

The experiments on periodic poling of VTE-MgO:SLN, described in this chapter, use electric-field poling, and more specifically, the full-cover electrode (FCE) method [173, 73]. The method is applicable primarily to  $z$ -cut substrates. One of the large surfaces is unpatterned, while on the other, a patterned dielectric coating is deposited. A top view of a typical periodic pattern for poling is shown on the diagram in Fig. 5.1. The crystal axes are shown on the diagram as well. In all experiments in this chapter, the pattern was deposited on the  $+z$  surface of the  $\text{LiNbO}_3$  wafer.

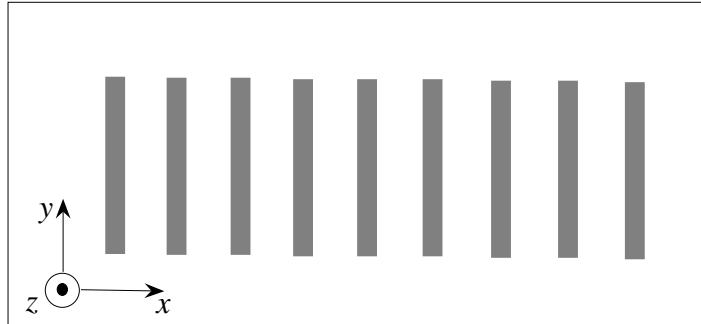


Figure 5.1: Top view of a typical periodic pattern used for poling

The gray periodic strips in the top-view diagram represent openings (trenches) in the dielectric coating. A full-cover electrode, such as a metallic coating or a liquid electrolyte electrode, located on top of the dielectric coating, can contact the surface of the crystal through these trenches. Domain inversion occurs when voltage higher than the product of the coercive field and the sample thickness, and with polarity opposite to the crystal spontaneous polarization, is applied between the electrodes on the two sides of the wafer.

The domain inversion does not occur at once, but starts at one of the two large surfaces with the nucleation of an inverted micro-domain, which then penetrates the sample thickness

[173, 63, 174, 175]. During the penetration phase, the domain shape is needle-like, with a pointed apex on one side and a base on the other (the nucleation side). The typical aspect ratio between the diameter of the base and the domain length (the needle height) is of order 1:100. The natural shape of the base is hexagonal or triangular. The sides of the hexagon or triangle are parallel to the crystalline  $y$ -axis.

The kinetics of domain inversion are complex and involve a variety of domain-propagation modes and domain shapes depending on poling conditions, such as applied electric field, crystal conductivity, electrode material, and temperature. Representative descriptions and models of domain kinetics can be found in the following references [176, 177, 178, 179, 180].

In this section, a simplified model of the domain kinetics is presented as a set of observations, to provide the basis for development of a process for periodic poling. Only the most essential properties, relevant to periodic poling of MgO:SLN, are described. The following characteristics were used in the development of a process for periodic poling of  $z$ -cut MgO:SLN:

1. Domain switching starts with the nucleation of micro-domains on the  $+z$  or  $-z$  surface of the wafer. The micro-domains penetrate the thickness of the wafer, less than 0.5 mm in the experiments described in this chapter, and then expand in the  $x$  and  $y$  dimensions.

2. Unrestricted domains (without any dielectric pattern) that fully penetrate the substrate assume a hexagonal shape after growth under spatially uniform electric field of the proper polarity to the ferroelectric axis. If adequate measures are taken to prevent neighboring domains from merging during the application of the electric field, the approximate size of the domain could be calculated by using knowledge of the average domain-wall velocity as a function of applied field.

3. Domain walls tend to be vertical. This is due to the large surface charge that would be formed at a non-vertical domain wall, due to the large spontaneous polarization of the crystal. Such charge would create a large electric field causing domain switching in the neighborhood of the wall until it becomes vertical. This tendency of domain walls to stay vertical makes periodic poling of bulk samples (hundreds of microns to millimeters thick) possible. The same uncompensated surface charge forces micro-domains to assume a needle-like shape. Slanted domain walls may occur at high temperature, when the electrical conductivity of the crystal is high enough to allow screening of the surface charge.

4. Nucleation of micro-domains only occurs on the  $+z$  or  $-z$  surface, and not in the

bulk.

5. The mechanism of domain-wall motion involves formation on the crystal surface of tiny sub-micron domains, connected to the existing domain wall [181]. These tiny domains merge to form a new wall, that is shifted with respect to the original wall. The sub-micron domains only occur in the neighborhood of existing switched domains. They need not penetrate the full thickness of the substrate due to their sub-micron size. Therefore, the newly formed domain wall need not be vertical during the application of the electric field, as sub-micron domains continuously form and move the domain wall near one or both crystal surfaces. After the external field is switched off, the domain wall shifts as necessary to become vertical.

6. The domain-wall velocity can be limited by the rate of nucleation of sub-micron domains in the wall neighborhood, or by bulk pinning sites. Note that in the case without bulk pinning sites, the domain will not expand in the bulk compared to the two surfaces, since, as postulated above, domain wall motion occurs through nucleation and merging of sub-micron domains on the surface.

7. When two domains merge under uniform spatial distribution of the electric field (no patterned dielectric), very high domain-wall velocities can be observed, due to reshaping of the total domain wall of the two domains. This situation is to be avoided during periodic poling, since it leads to poor quality of the periodic pattern.

8. Near the edges of patterned electrode, the local electric field can be much higher than the average field in the bulk, which is approximately equal to the ratio of the applied voltage and the sample thickness. The field enhancement at the edges of electrodes is due to fringe-field effects [174, 73]. It is one reason why on periodic patterns with orientation as in Fig. 5.1, the velocity of domain expansion along the electrode is orders of magnitude higher than in the perpendicular direction (along the crystalline  $x$ -axis). For short-period QPM gratings with large lateral extent (for large-aperture frequency mixing), the velocity along the electrode must be two orders of magnitude higher than the velocity of the domain wall along the  $x$ -axis. The fringe fields only penetrate to depths comparable to the electrode period. If the nucleation characteristics of the  $+z$  and  $-z$  surface are comparable under uniform poling conditions, then during patterned poling, the initial nucleation always occurs at the tips of the periodic electrodes on the patterned surface due to the large fringe fields.

9. Obtaining a high-quality periodic pattern is significantly less challenging when aided by self-termination of the poling process [174]. Self-termination is the stopping of the process

of domain inversion caused by uncompensated surface charge trapped under the dielectric layer during poling. The trapped uncompensated charge is the source of electric field. If the charge is on average evenly distributed across the surface, it will create a uniform electric field opposite to the external field, causing the domain inversion to slow down or stop.

10. Assuming that the lithium niobate substrate is much thicker than the poling period, the electric-field conditions near the unpatterned surface are similar to the conditions realized during uniform poling without a patterned dielectric. Since the thickness of the patterned dielectric is usually of order 0.01 of the thickness of the substrate, the electric field near the unpatterned surface is approximately  $(1 - 0.01\epsilon_{LN}/\epsilon_{diel})$  times the field present in the case of uniform poling without a dielectric film. The quantities  $\epsilon_{LN}$  and  $\epsilon_{diel}$  are the dielectric constants of the crystal and the dielectric coating, respectively. The dielectric constant of  $\text{LiNbO}_3$  is  $\sim 30$ , so a well-baked photoresist with  $3 \leq \epsilon_{diel} \leq 10$  may help decrease the field near the unpatterned face by 3–10%

11. The patterned dielectric plays two major roles: surface-charge trapping and fringe-field enhancement. Besides aiding self-termination, surface-charge trapping ensures that domains don't merge at the patterned surface during the application of the external field. The fringe-field enhancement is highest at the pointed edge of the electrode, where the initial nucleation usually occurs. After that, the fringe fields at all locations along the electrode help increase the rate of submicron nucleation, aiding the fast domain growth along the trench. At the same time, the surface charge trapped under the dielectric, prevents the sub-micron domains from merging in the space between two electrodes, stopping the domain-wall movement at the patterned surface.

12. If the charge trapping under the dielectric coating is efficient, merging of domains nucleated at separate neighboring electrodes will be prevented at the patterned surface. At that point, such undesirable merging can only occur at the unpatterned surface and may then propagate up throughout the thickness of the wafer. This is assumed to be the main mechanism of defect formation that limits short-period periodic poling with full thickness penetration. As mentioned earlier, the domain-wall velocity near the unpatterned surface can be determined from experimental data of domain-wall velocity during uniform poling. If charge trapping at the patterned surface is uniform, the amount of trapped surface charge per unit area can be related to the duty cycle of the inverted domains during poling. In this way, the electric field near the unpatterned surface can be calculated as a function of the domain duty-cycle by subtracting the field generated by the surface charge from the

external field. Using information on the domain-wall velocity as a function of the local field, the rate of domain-wall movement can be calculated [174, 64] and an appropriate waveform of the applied voltage designed.

13. In order for the above waveform design process to work, uniform trapping of the surface charge has to occur. Figure 5.2 compares schematically the cases of the field generated by a plane of trapped charge and the field generated by a limited area of trapped charge. It is assumed that the patterned dielectric is on the original  $+z$  surface, and after some domain inversion that has grown slightly beyond the area of each contact opening of the patterned electrode, negative charge has been trapped under the dielectric film in the immediate surroundings of each trench. A localized area of trapped surface charge

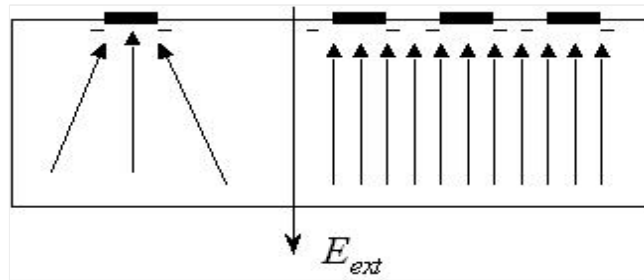


Figure 5.2: Schematic comparison of self-termination field caused by uniform planar trapped-charge distribution (right) and localized or non-uniform charge distribution (left). The thick black lines represent the contact electrodes on the patterned side. Near the unpatterned surface, the density of electric field lines generated by the trapped charge is significantly reduced in the case of localized trapped charge, indicating smaller self-termination field

should have a characteristic diameter at least comparable to the wafer thickness, in order for the self-termination field to be significant near to unpatterned surface. In all varieties of PRD-resistant MgO-doped  $\text{LNbO}_3$ , the nucleation-site density at room temperature is not uniform across the sample and therefore the periodic poling occurs in patches. In order to achieve self-termination, it is necessary to obtain conditions in which the characteristic time for expansion of the patch of periodic poling to a diameter comparable to the wafer thickness, is shorter than the time necessary for the domain wall near the unpatterned surface to propagate a distance equal to half the period. Increase of the nucleation-site density and the rate of formation of submicron domains for fast domain growth along the contact

electrode can therefore promote self-termination.

## 5.2 Domain-wall velocity and nucleation-site density in 0.3 mol-% MgO:SLN

Two of the material parameters that play an important role in the kinetics of periodic poling are the dependences of the domain-wall velocity and the nucleation-site density on the electric field. Measurements of the domain-wall velocity as a function of applied field were made using the method developed by Miller [174]. After initial formation of domains that penetrate the full sample thickness by using a voltage pulse, the crystal was etched in hydrofluoric acid to reveal the locations of each domain wall. Single pulses of electric field were applied afterwards with measured voltage and pulse length. After each pulse, the sample was etched and the distance between the new and the old location of the domain wall was measured using an optical microscope. In this way, the domain-wall velocity was measured at several values of the electric field. The results are plotted in Fig. 5.3.

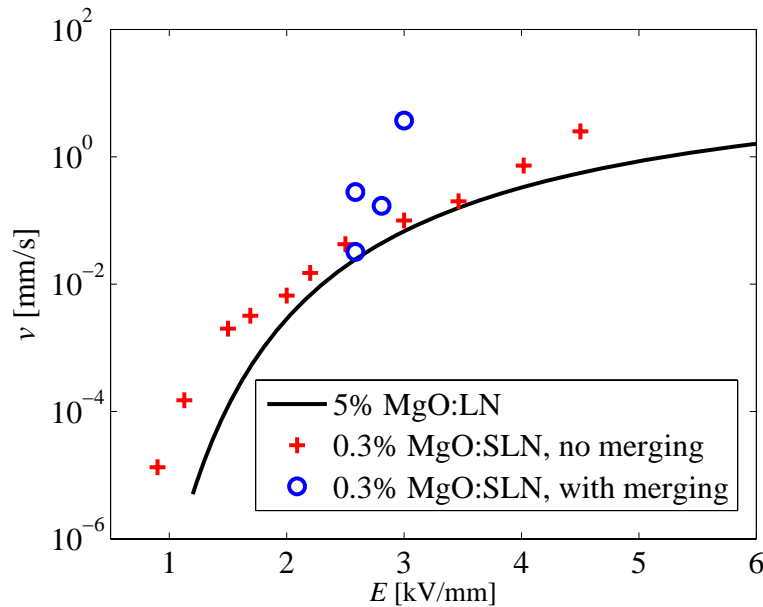


Figure 5.3: Domain-wall velocity of VTE- 0.3 mol-% MgO:SLN versus applied field. The solid line represents the similar dependence in 5 mol-% MgO:LN [64]

The experimental data is limited, but it is clear that the domain-wall velocity in 0.3

mol-% MgO:SLN is similar to that in 5 mol% MgO:LN at the same applied fields, except for the region below 2 kV/mm, where it appears an order of magnitude higher. High slope of the  $v(E)$  dependence is desirable for better self-termination [174, 64], so electric fields in the range 1-1.5 kV/mm were the focus of initial experiments with periodic poling of MgO:SLN. The advantage of the high slope is not enough for obtaining short-period patterns if adequate nucleation density is not secured first.

A qualitative estimate of the dependence of nucleation-site density on the applied field under conditions similar to the poling with liquid electrolyte electrodes was obtained by measuring the number of nuclei per mm along the edge of a uniform electrode with area of several square millimeters. The electrode consisted of a piece of paper soaked with saturated solution of LiCl. On the other (bottom) side of the sample, a larger-area electrode was used, to simulate the poling conditions with unpatterned electrode. The fringe fields near the edge of the top electrode ensured that nucleation occurs at the edge only, for the moderate voltages used. The actual field at the electrode edge was not calculated, so the nucleation data are plotted versus the field inside the area covered by the electrode, equal to the ratio of the applied voltage and the sample thickness. The experimental data are shown in Fig. 5.4. The nucleation density per unit length, measured along the  $y$ -crystalline axis, seems to increase approximately linearly with voltage within the range of fields relevant to periodic poling of 0.3 mol-% MgO:SLN.

While the linear nucleation density increases by a factor of 8 between 1.5 and 8 kV/mm, the domain-wall velocity increases by more than 3 orders of magnitude within this range. From Fig. 5.3, the domain-wall velocity for voltages above 2.5 kV/mm is over 10  $\mu\text{m/s}$ . It will be difficult to obtain domain patterns with periods for visible light generation (e.g., 10  $\mu\text{m}$  for yellow, 7  $\mu\text{m}$  for green, 4–5  $\mu\text{m}$  for blue) if the domain-wall velocity is so high, unless the nucleation density is high. The best results on periodic poling of 0.3 mol-% MgO:SLN for visible light generation were obtained with fields in the range 1.5-2.5 kV/mm.

### 5.3 Other properties relevant to poling

The periodic poling, described in this chapter, used hard-baked photoresist (PR) as the dielectric. A schematic vertical cross-section of the periodic pattern in the PR is shown in Fig. 5.5. For this crystal orientation, the top is covered with the positive electrode, while the bottom is covered with the negative electrode. The poling period is  $\Lambda$ . After

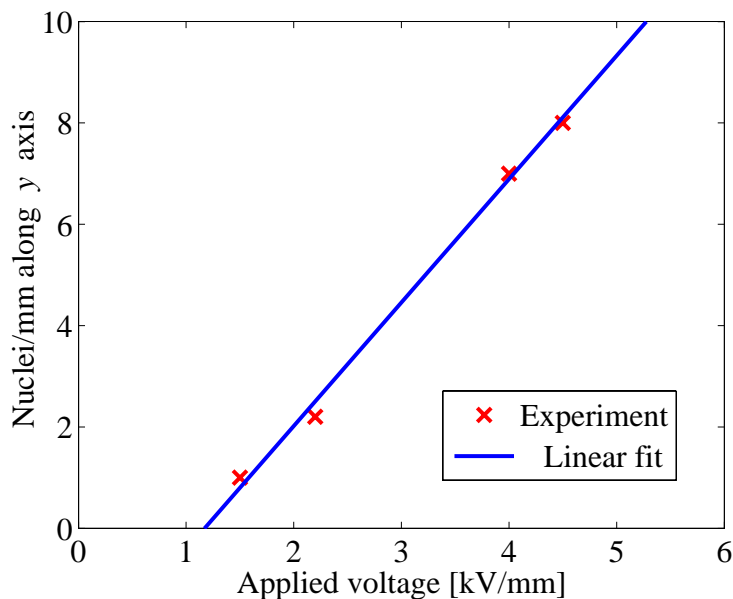


Figure 5.4: Nucleation-site density in 0.3 mol-%MgO:SLN versus voltage normalized to the sample thickness

photolithography, the trenches in the photoresist have a slope that is different from 90 degrees, so the width  $w_b$  at the bottom is smaller than the width  $w_t$  at the top.

For high fringe fields, the patterned dielectric should be thicker than a third of the period and should have a low dielectric constant, and the trenches should be as narrow as possible [73]. In addition, the trench walls should be as close to vertical as possible.

Low electrical conductivity is required of the patterned dielectric for efficient trapping of the surface charge. Hard-baking the PR lowers its dielectric constant and the electrical conductivity [174]. It was determined in the present study that the typical hard-bake (105 °C, 3 hours) that is adequate for high-quality periodic poling of non-doped CLN does not provide enough insulation for poling of MgO-doped crystals. In addition, the usual hard-bake leads to photoresist “reflow”, which lowers the slope  $\theta$  of the trenches and reduces the fringe fields.

To provide adequate insulation and adequate fringe fields, a hard-bake recipe was developed that preserved the high slope of the trenches while significantly reducing the conductivity of the photoresist. The patterned photoresist was first baked at 75 °C for 2 hours and at 95 °C for 2 hours, to evaporate solvents. After that, the resist was baked at 130 °C

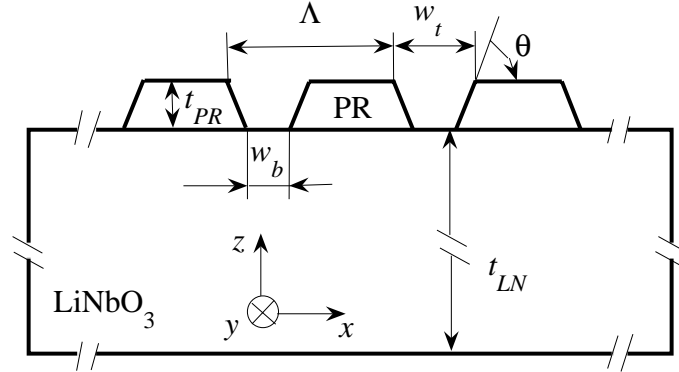


Figure 5.5: A schematic of the photoresist pattern for periodic poling

for 15-18 hours. After the hard bake, the thickness of the photoresist was typically 3–3.5  $\mu\text{m}$ . The long bake ensured cross-linking of the photoresist that suppresses conductivity. The relatively low temperature prevented the reflow. Note that at temperatures below 128  $^{\circ}\text{C}$  cross-linking may not occur.

The bottom width of the trench,  $w_b$  was typically 1  $\mu\text{m}$ , which is the lowest readily reproducible width. The maximum slope  $\theta$  that could be obtained was about 70 degrees.

Although the FCE method for periodic poling provides significant flexibility in the control of the fringe fields by modifying the geometric and material parameters of the patterned dielectric, it provides limited fringe-fields, unless dry etching is used to fabricate trenches with vertical walls. Therefore, the FCE method only works for long-period poling of 5 mol-% MgO-doped CLN, since this material requires very high fringe fields at room temperature for adequate nucleation density. On the other hand, the lightly-doped SLN, which requires lower fringe-fields for nucleation, can be periodically poled using the FCE method, as described in the next section.

## 5.4 Pulsed periodic poling

Short-period poling in 5 mol-% MgO:LN is usually performed by using a combination of metal electrodes, high temperature, and trains of short pulses of electric field [67, 68, 65, 66]. These methods of periodic poling use patterned electrodes that cover only the contact area, rather than the whole wafer. With these electrodes, higher fringe-fields are possible.

The trains of short pulses are easy to implement in combination with the FCE method without any changes in the necessary equipment for domain patterning. In the the poling experiments described in this work, a full-cover electrode consisting of saturated solution of LiCl in water was used at room temperature.

After a short pulse, newly inverted domains tend to switch back to the original orientation, unless a stabilization field is applied to prevent this back-switching. Partial back-switching, attributed to inverted domains shrinking in size, is desirable, as it helps prevent fully inverted domains from growing too large while other domains are still in the initial phases of poling. This partial back-switching is an advantage of poling with a train of short pulses compared to poling with a single long pulse. With pulse trains, increasing the repetition rate can reduce the back-switching effect. It was found experimentally that pulses with duration of  $\sim 0.1$  ms and peak electric fields of  $\sim 2$  kV/mm produce the best results in periodic poling of 0.3 mol-% MgO:SLN. The optimum repetition rate was 1-2 kHz. After each pulse, there is some back-switching current. To prevent complete back-switching, a stabilization-field plateau is added after the pulse. The plateau field is several times lower than the field of the poling pulse.

It was found experimentally that the plateau promotes undesirable merging of domains, so a dip-to-zero was added between the pulse and the plateau to prevent merging. A dip-to-zero as short as 50  $\mu$ s helped avoid the merging. Without the plateau, poling took too long and occurred in patches, such that in some areas the domain duty cycle grew to 90%, while in others poling had not occurred at all. A sketch of the typical voltage waveform is shown in Fig. 5.6.

## 5.5 Results of periodic poling with LiCl electrodes

Using the short-pulse-trains described above, high-quality domain patterning for periods suitable for second-harmonic generation of yellow and green light was obtained. To ensure proper domain duty cycle, the appropriate amount of charge, equal to the product of the

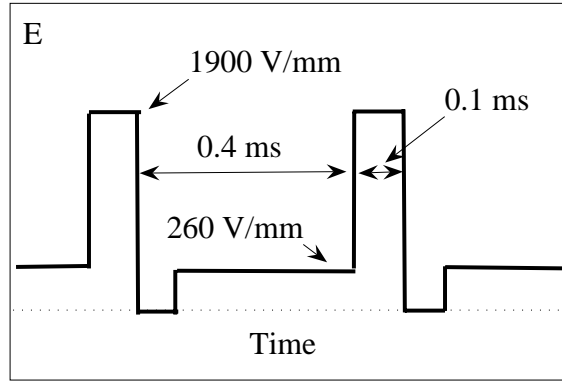


Figure 5.6: Typical voltage waveform used in short-pulse poling of MgO:SLN

area of poled domains and twice the spontaneous polarization, has to be transferred across the wafer. The charge was calculated in advance and the pulse train was stopped when the appropriate charge was delivered. The maximum length of the pulse train was limited to 10 s by the computer hardware. For long poling periods, such as 15  $\mu\text{m}$ , the self-termination of periodic poling was nearly complete, so that there was no need to manually interrupt the pulse train. For short periods (7-9  $\mu\text{m}$ ), the self-termination was only partial, such that the poling current decreased 3-5 times after the appropriate amount of charge had been delivered. Terminating the pulse train at that point helped prevent excessive domain duty cycle.

Some photos of periodic domain patterning revealed by chemical etching with hydrofluoric acid are included in figures 5.7, 5.8 and 5.9.

The periodic poling in 0.3 mol-% MgO:SLN with period of 9.6  $\mu\text{m}$  (Fig. 5.7) has a duty cycle of 50 %, ideal for maximum-efficiency SHG of yellow light near 589 nm. The poling with a similar period on 0.5 mol-% MgO:SLN also has high quality, although the duty cycle is larger than 50 % (Fig. 5.8). Similar poling is obtained in 0.3 mol-% MgO:SLN with a period of 8.3  $\mu\text{m}$ . The domain pattern in Fig. 5.9 has a period of 7  $\mu\text{m}$  and some irregularity of the domain structure is present, that would decrease conversion efficiency by

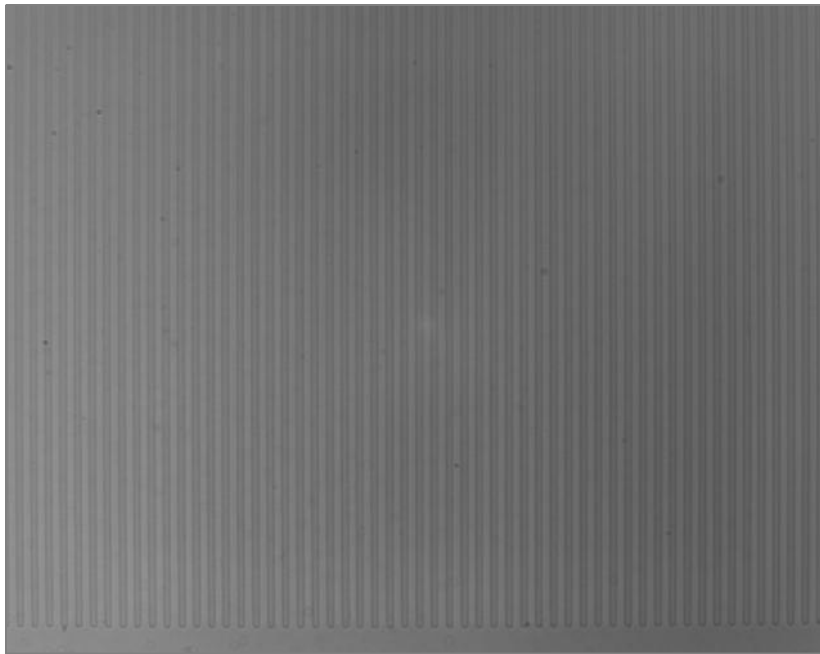


Figure 5.7: Domain pattern with period of  $9.6 \mu\text{m}$  in 0.28-mm thick 0.3-mol-% MgO:SLN. The  $-z$  face is shown, which was the unpatterned side during poling.

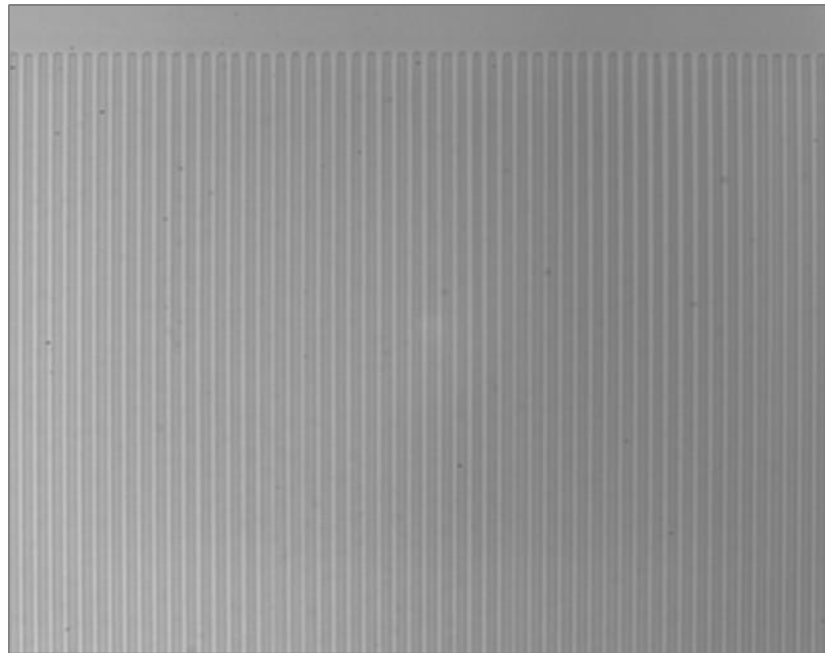


Figure 5.8: Domain pattern with period of  $9.7 \mu\text{m}$  in 0.28-mm thick 0.5-mol-% MgO:SLN

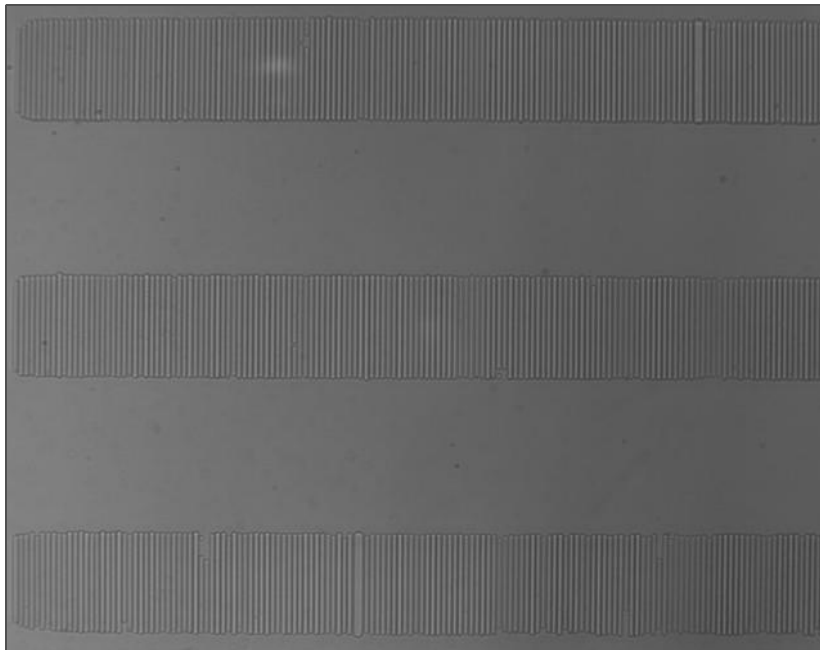


Figure 5.9: Domain pattern with period of  $7\ \mu\text{m}$  in 0.28-mm thick 0.3-mol-% MgO:SLN

20–30 %. The width of each of the three QPM gratings in the picture is 130  $\mu\text{m}$ . More recently, periodic poling with a period of 7  $\mu\text{m}$  was obtained in wider gratings with lateral extent of 400  $\mu\text{m}$ , allowing easy alignment of the laser beam for SHG. The experiments on SHG of 532-nm radiation are described in the next section.

## 5.6 SHG of high-power CW green radiation in PPMgSLN near room temperature

Stable generation of 1.3 W at 532 nm by SHG in a 15-mm-long periodically-poled VTE-MgO:SLN crystal was demonstrated recently [75]. It was determined that annealing the sample in air at  $\sim 340$  °C for 20 hours improved the power-handling ability of the crystal, apparently by reducing the residual absorption in the green, and thus the attendant thermal focusing and phase mismatch. Before annealing, the maximum green power was limited to 0.4 W with a tightly focused beam and to 0.9 W with a less-tightly focused beam. After annealing, the green output power was limited by the by the low-quality periodic pattern and the available pump laser power (10.5 W). In this section, experiments with improved periodic poling and a higher-power laser are described. The maximum power available from the CW laser was 14 W.

The SHG experiment was performed in collaboration with Karel Urbanek. The two crystals used in the experiment had periods ranging from 6.95 to 7.15  $\mu\text{m}$ . One crystal was 17-mm long, while the other was 12-mm long. The crystals had no anti-reflection coatings. The power losses due to reflections were about 14 % per surface. The focusing was chosen within the range between optimum focusing and confocal focusing. According to the Sellmeier equation (Eq. 4.8), room-temperature phase-matching was expected at a period of 7.09  $\mu\text{m}$ . Phase-matching was observed at 28 °C at a period of 7.06  $\mu\text{m}$  and at 18 °C at a period of 7.08  $\mu\text{m}$ .

In the 17-mm-long crystal, as the pump power was gradually increased, stable operation at green power levels reaching 3 W inside the crystal was observed. At a green power level of 3.4 W, the crystal output facet cracked. The cracking occurred after the phasematching temperature was adjusted for maximum green power, not during the increasing of the fundamental pump power. The trace of the crack appeared to be caused by thermal self-focusing. The local heating seemed to be due to absorption related to the green beam, since no damage was observed at the full 14 W of pump without high-intensity green light (e.g.,

at crystal temperatures away from phasematching).

With the shorter crystal, an input lens with shorter focal length was used, to ensure that the beam focusing was near optimum (the crystal length being between 2 and 5.6 times the confocal parameter). In this case, the lower-power results were recorded before the crystal cracked. The results of green output power versus laser power are shown on Fig. 5.10. The green power was stable at all pump power levels up to the point of crystal cracking.

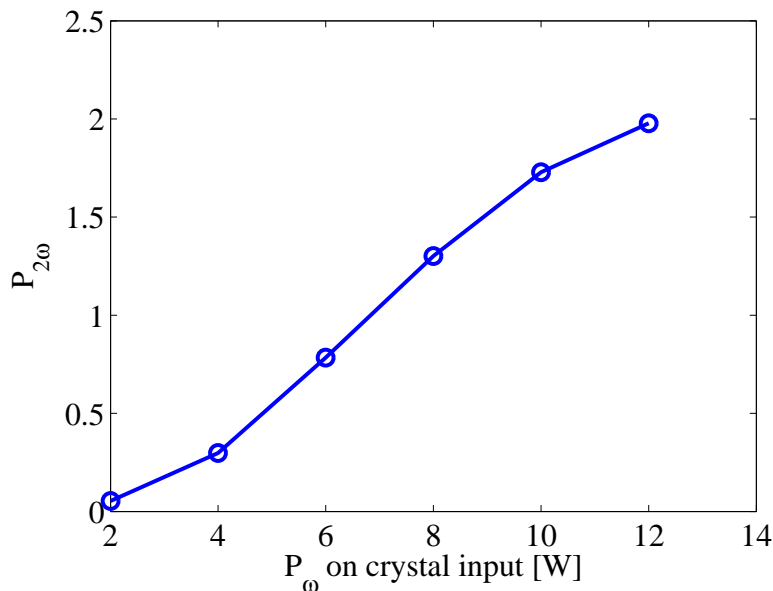


Figure 5.10: SHG power inside the crystal at 532 nm versus input pump power

There is clear deviation from the quadratic dependence characteristic for SHG in the low-conversion limit. At the maximum green power of 2 W, only about 20% of the pump power in the crystal has been converted to green. Therefore, most of the deviation from the quadratic dependence is due to thermal dephasing, causing non-uniform QPM along the beam. After stable generation of 2-W of 532-nm radiation for 4 hours, the pump power was increased from 12 to 14 W. The crystal temperature had to be reduced to compensate for the local heating caused by the laser beam. As soon as the green power level reached  $\sim 2.5$  W, the crystal cracked.

From the above experiments, it is clear that the maximum power in the crystal is limited by absorption related to the green intensity. The absorption may be either absorption of the green itself, or GRIIRA. The saturated space-charge field of the substrate, from which

## 5.6. SHG OF HIGH-POWER CW GREEN RADIATION IN PPMGSLN NEAR ROOM TEMPERATURE

the crystals were cut, was 10 V/mm. Although this value is low enough to avoid significant PRD, it is larger than the lowest values of  $\sim 1$  V/mm, obtained for 0.3 mol-% MgO:SLN. This indicates that there may be some residual antisites. Therefore, some residual GRIIRA may be present. Further studies should focus on experiments with samples with lower space-charge field that presumably have smaller GRIIRA. In addition, measurements of GRIIRA and green absorption should clarify which of the two was larger at green power levels of 2.5–3.5 W and residual pump in the crystal of 6.5–7.5 W. Reduction of the absorption in the green part of the spectrum may be possible with longer annealing in air, annealing in oxygen, or electrochemical oxidization of the crystal.

# Chapter 6

## Conclusion

### 6.1 Summary of contributions

This dissertation has described a powerful tool for the design of nonlinear optical integrated circuits based on annealed proton-exchanged and reverse proton-exchanged waveguides in lithium niobate. The developed model has been used extensively for waveguide design not only within the research group, but also by scientists in other research organizations. The model provides accurate prediction of the concentration-dependent diffusion of protons in  $\text{LiNbO}_3$ , and contains accurate information about the dispersion of the proton-exchanged material, allowing calculations of phase-matching and efficiency to be made for most of the transparency region of  $\text{LiNbO}_3$ .

Using the model, RPE waveguides for difference-frequency generation were developed and used to generate several-milliwatt-level, single-frequency, tunable radiation near 3.3 and 4  $\mu\text{m}$ . This is the highest power level generated in the region using waveguide DFG. In addition, 4  $\mu\text{m}$  is the longest wavelength generated using waveguide DFG. The reasons for discrepancy between expected and observed efficiency have been recognized as the excessive losses at the mid-IR wavelength, due to the tails of the O–H stretch at 2.8  $\mu\text{m}$ . Measurements of the losses were performed that proved the predictions. The demonstrated power levels are already attractive for applications such as environmental monitoring of methane and free-space communications in the atmospheric transparency region between 3.5 and 4  $\mu\text{m}$ . A waveguide was designed that used the difference-frequency mixing process to provide 45 dB of parametric amplification at 1.5  $\mu\text{m}$  for low pump-pulse energy. Output pulses at 1.57  $\mu\text{m}$  with near 1- $\mu\text{s}$  duration and up to 10  $\mu\text{J}$  of energy were demonstrated.

Significant problems in waveguide performance were solved merely by implementing several small changes in the waveguide design. The success of this approach relied on the good understanding of the waveguide based on the fabrication model and the observed performance of the first-generation device.

In addition, the waveguide model has been used in the design of low-loss high-efficiency RPE-waveguide devices. The usefulness of these devices was demonstrated through collaborations with researchers within the nation and abroad, who used the frequency-conversion devices in a variety of applications. Frequency conversion in low-loss waveguides was a significant contribution toward a demonstration of a quantum key-distribution system at  $1.55\ \mu\text{m}$  [182] using single-photon detection [35] based on high efficiency up-conversion [151] of  $1.5\text{-}\mu\text{m}$  photons to enable photon counting at  $0.71\ \mu\text{m}$  with a silicon avalanche photodiode. Additional demonstrations included a nonlinear intensity discriminator for optical code-division multiple access systems [34, 183, 184], highly efficient SHG of a low-power laser to enable frequency stabilization by locking the output to an Rb or an iodine cell [185, 36], optical time-division multiplexing at 160 Gb/s using a PPLN waveguide as an efficient gated mixer for a  $1.5\text{-}\mu\text{m}$  clock and four channels of 40 Gb/s NRZ data [186], and ultra-low-threshold one-dimensional solitons in RPE planar waveguides [187].

The techniques for accurate characterization of waveguides were used for the development of the most efficient APE channel SHG waveguide device in 5 mol-% MgO:LN at  $1.55\ \mu\text{m}$  (in collaboration with J. Tian, L. Zhang and G. Imeshev) [188], which could be used for frequency conversion and mid-span spectral inversion. The device had significantly improved resistance to photorefractive damage compared to waveguides in congruent  $\text{LiNbO}_3$ .

In addition, a VTE-based method for obtaining  $\text{LiNbO}_3$  crystals with Li-rich composition that solves the problems of photorefractive damage and green-induced infrared absorption has been developed. The initial problems with formation of scattering centers and difficulty of periodic poling have been solved. A simple poling method for obtaining short periods with good quality has been developed by utilizing the advantages of lightly-doped SLN compared to 5 mol-% MgO:LN, and at the same time properly analyzing the reasons for difficulty of periodic poling of all MgO-doped crystals. Stable generation of 2 W of CW green radiation has been experimentally demonstrated in the new VTE- 0.3 mol-% MgO-doped  $\text{LiNbO}_3$ . The potential for generation of more than 3 W of green radiation has been experimentally demonstrated, and the challenges caused by residual absorption identified.

## 6.2 Future possibilities

The waveguide model has not yet realized its full potential. Integrated optical circuits with several components operating mainly at  $1.55\ \mu\text{m}$  should be accurately predicted by the model. Further improvements of the model should be considered if applications demand more accuracy and precision. Several areas of further improvement have been mentioned in terms of the new findings related to stability of the soft-annealed and annealed waveguides and the simplifying model assumptions.

In the area of mid-IR generation, further improvements can be done by taking the mid-IR losses into account during device performance optimizations. Ways to reduce the losses must be explored. Some possibilities for improvement include deeper burying of the RPE waveguide to further avoid the dead layer, combined with reducing the peak proton concentration. This approach is most likely to lead to improvements in the range  $2.5\text{-}3.5\ \mu\text{m}$ , where the losses due to OH absorption seem to be significant. In the range around  $4\ \mu\text{m}$ , the losses are only moderate and their reduction could only improve performance by  $\sim 50\%$ , assuming that light confinement is unchanged. If the reduction of losses in that wavelength range is pursued merely by reducing peak proton concentration, it is likely to lead to disappointing results, since the resulting reduced confinement of the idler can lead to lower mode-mixing efficiency and lower overall performance. To obtain mid-IR power levels in the range of  $100\ \text{mW}$ , similar waveguide devices may need to be developed in MgO-doped substrates, such that more pump power can be used without photorefractive damage.

In the area of lightly MgO-doped VTE-SLN, the main focus in the near future must be the proper identification of the source of increased absorption in the presence of intense green light. In comparison to congruent non-doped  $\text{LiNbO}_3$ , the GRIIRA effect has clearly been significantly reduced in the periodically poled samples used in the 2-W SHG experiment. Yet, the maximum SHG power was limited by thermal effects, so more work needs to be done in order to increase the output power. Ways of decreasing the absorption in the visible, such as more complete oxidation of the sample, can be explored. In addition, comparison of the GRIIRA of samples with different values of the space-charge field can be made, to find whether the GRIIRA effect varies significantly between samples with space-charge fields of  $1$  and  $10\ \text{V/mm}$ .

In the area of periodic poling of MgO:SLN, more sophisticated methods can be explored, to allow the fabrication of thicker periodically poled substrates, as well as shorter periods.

Finding the reasons for the absorption shoulder in the UV and ways to eliminate it may allow using VTE:SLN for generation of UV by frequency conversion.

APE and RPE waveguides can be developed in MgO:SLN. Some promising results have already been obtained, in terms of moderate-loss waveguides in 1 mol-% MgO:SLN. A significant amount of data has been collected on one-dimensional diffusion of protons on planar  $z$ -cut substrates. An accurate fabrication model similar to the one for CLN will likely be developed in the near future. It is expected that APE and RPE waveguides in MgO-doped SLN will provide the great advantage of resistance to photorefractive damage. In addition, the  $\text{OH}^-$  absorption peak in SLN has a simpler structure than that in CLN. There may be a possibility of significantly lower RPE-waveguide losses in the mid-IR in regions far from the main  $\text{OH}^-$  peak. These possibilities can be explored. MgO:SLN waveguides may provide a better alternative to CLN waveguides for power levels beyond 10 mW. The expected resistance to photorefractive damage will be a great advantage by allowing higher pump power to be used. Finally, exploring new ways of waveguide formation that do not involve proton exchange will help completely eliminate the problem of  $\text{OH}^-$  absorption.

## Appendix A

# Calibration of the OH absorption measurement

This appendix describes the calibration used to correct for the dependence of the OH<sup>-</sup> absorption peak on crystalline phase of PE LiNbO<sub>3</sub>. The absorption measurement is used for estimating the total number of protons in a planar SA, APE, or RPE waveguide.

In all measurements, the  $z$ -cut planar waveguide sample was placed across the spectrophotometer beam in a fixture cut in such a way that the angle between the crystal  $z$  axis and the beam was  $8\pm 1$  degrees rather than zero to suppress Fabry-Perot fringes that would occur due to multi-pass interference in the thin sample.

The polarized OH absorption peak alone has a complex structure consisting of at least four peaks for waveguides containing  $\alpha$ ,  $\kappa_1$  and  $\kappa_2$  phases and at least three peaks in the  $\alpha$  phase alone [139, 140]. The multiple peaks in a single phase are due to the existence of several slightly different sites that protons can occupy. In lithium niobate of the congruent composition, the peaks overlap and look like a single broad peak that cannot be fitted with a single Gaussian or Lorentzian due to its underlying structure.

A study of the dependence of the area of the OH absorption peak on anneal time revealed the possibility to account for the effects of the complex structure of the absorption peak in a simple way without the need for resolving multiple overlapped peaks. An “average wavelength”  $\lambda^{av}$  of the peak, defined as

$$\lambda^{av} = \int d\lambda \lambda \int_0^t dz \alpha(z, \lambda), \quad (\text{A.1})$$

was found to increase with annealing. Annealing generally leads to the conversion of  $\kappa_2$  to  $\kappa_1$  and  $\kappa_1$  to  $\alpha$  phase via diffusion-based reduction in proton concentration. The area  $A$  of the absorption peak defined in Eq. 2.31 was also found to change with annealing. The relationship between  $\lambda^{av}$  and the area is plotted in figure A.1 for several samples with different soft-annealed depth  $d_{SA}$  of the protonated layer.

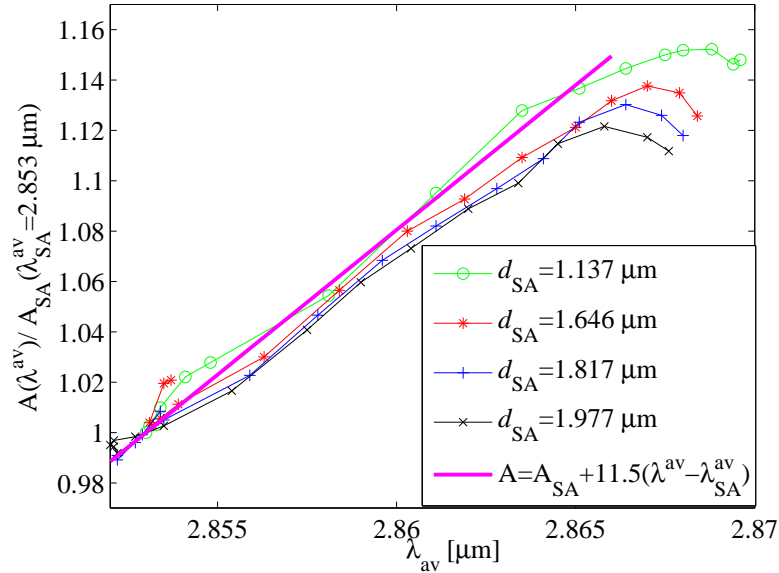


Figure A.1: Calibration curves for the absorption measurement

The slight decrease of  $A$  for  $\lambda^{av} > 2.865\mu\text{m}$  is due to some loss of protons from the surface of the planar waveguide sample during the high-temperature annealing. Korkishko and coworkers [130] observed that the area of the absorption peak of APE waveguides covered with a layer of  $\text{SiO}_2$  prior to annealing was larger than the area of the peak for waveguides that were not overcoated. They attributed the difference to a flux of protons out of the crystal surface in the form of water vapor. A similar experiment was performed in this study to qualitatively estimate the effect and its influence on the waveguide characterization and modeling. One of two identical planar waveguides was overcoated with  $\text{SiO}_2$  and the two waveguides were annealed multiple times at  $328^\circ\text{C}$  for a total of  $\sim 200$  hours. The difference in the areas of their  $\text{OH}^-$  absorption peaks started from 0 and grew monotonically with time. After a total of  $\sim 200$  hours, the area of the sample with the  $\text{SiO}_2$  overcoat was 3 % larger than the area of the non-coated sample. The area of the coated sample did not start

to decline within the 200-hour annealing period, although its rate of growth significantly decreased, perhaps due to the slowing down of diffusion when the proton concentration distribution became very deep and nearly flat. The typical annealing time at 328 °C for practical waveguide devices is shorter than 30 hours. For such short times, the difference between the absorption of the coated and the uncoated sample was within the measurement error of 0.5%. Therefore the effect was disregarded in the modeling of proton diffusion in the crystal.

The curves in Fig.A.1 that correspond to the deeper waveguides have a smaller slope than the curves corresponding to the shallower because a thicker initial layer has more protons which take longer to diffuse, causing the corresponding absorption peak to shift more slowly in wavelength. By the time the absorption peak of a deeper waveguide shifts as much as the peak of a shallower waveguide, the deeper waveguide loses more protons from the surface because protons evaporate from the surface at the same rate for shallow and deep waveguides. This is why the calibration curves for deeper waveguides lie below those for shallower waveguides.

Most of the shift in  $\lambda^{av}$  and the correlated increase of absorption area happens during the first 30-60 hours of annealing at 328 °C for APE waveguides with depths optimised for telecommunication wavelength conversion. This is the time necessary for most of the index profile to enter the  $\alpha$ -crystalline phase. The average peak position for APE waveguides is usually in the range 2.860-2.862  $\mu\text{m}$ , while for RPE waveguides it is around 2.865  $\mu\text{m}$ . The thick straight line in Fig.A.1 was used for calibration of all absorption measurements used in the characterization of APE and RPE waveguides. It was chosen closer to the curve corresponding to the shallowest calibration waveguide since the linear approximation was to be used mostly for characterization of RPE waveguides. Their appropriate annealing time in air at 328 °C is short (typically less than 10 hours), making the loss of protons insignificant.

## Appendix B

### List of acronyms

APE	annealed proton-exchange
BA	benzoic acid
CDMA	code-division multiple access
CLN	congruent lithium niobate
DFG	difference-frequency generation
DM	dilute melt
GRIIRA	green-induced infrared absorption
IWKB	inverse Wentzel-Kramers-Brillouin
LN	lithium niobate
LT	lithium tantalate; low-temperature
MgO:	magnesium-oxide-doped
mid-IR	middle infrared
OFM	optical-frequency mixer
OPA	optical parametric amplification
PE	proton exchange
PRD	photorefractive damage
QPM	quasi-phasematching
RPE	reverse proton-exchange
SA	soft anneal
SCF	space-charge field
SFG	sum-frequency generation

SHG	second harmonic generation
SLN	near-stoichiometric lithium niobate
SLT	near-stoichiometric lithium tantalate
TSS	top-seeded solution
VPE	vapor-phase exchange
VTE	vapor-transport equilibration
VTEMgLN	vapor-transport equilibrated MgO-doped LiNbO <sub>3</sub>
WDM	wavelength-division multiplexing

# Bibliography

- [1] J. A. Armstrong, N. Bloembergen, J. Ducuing, and P. S. Pershan, “Interactions between light waves in a nonlinear dielectric,” *Phys. Rev.* **127**(6), 1918–1939 (1962).
- [2] M. L. Bortz, “Quasi-phasematched Optical Frequency Conversion in Lithium Niobate Waveguides,” Ph.D. thesis, Stanford University (1994).
- [3] G. D. Boyd and D. A. Kleinman, “Parametric Interaction of Focused Gaussian Light Beams,” *Journal of Applied Physics* **39**(8), 3597–3639 (1968).
- [4] M. A. Arbore, “Generation and manipulation of infrared light using quasi-phasematched devices: ultrashort-pulse, aperiodic-grating and guided-wave frequency conversion,” Ph.D. thesis, Stanford University (1997).
- [5] M.-H. Chou, “Optical Frequency Mixers Using Three-wave Mixing for Optical Fiber Communications,” Ph.D. thesis, Stanford University (1999).
- [6] G. Imeshev, “Tailoring of ultrafast frequency conversion with quasi-phase-matching gratings,” Ph.D. thesis, Stanford University (2000).
- [7] C. R. Menyuk, R. Schiek, and L. Torner, “Solitary waves due to  $\chi^{(2)} : \chi^{(2)}$  cascading,” *Journal of the Optical Society of America B* **11**(12), 2434–2443 (1994).
- [8] S. Wang, V. Pasiskevicius, F. Laurell, and H. Karlsson, “Ultraviolet generation by first-order frequency doubling in periodically poled KTiOPO<sub>4</sub>,” *Optics Letters* **23**(24), 1883–1885 (1994).
- [9] K. Mizuuchi, K. Yamamoto, M. Kato, and H. Sato, “Broadening of the Phase-Matching Bandwidth in Quasi-Phase-Matched Second-Harmonic Generation,” *IEEE J. Quantum Electronics* **30**(7), 1596–1604 (1994).

- [10] L. E. Myers, R. C. Eckardt, M. M. Fejer, R. L. Byer, and W. R. Bosenberg, "Multigrating quasi-phase-matched optical parametric oscillator in periodically poled LiNbO<sub>3</sub>," *Optics Letters* **21**(8), 591–593 (1996).
- [11] V. Pruneri, S. D. Butterworth, and D. C. Hanna, "Low-threshold picosecond optical parametric oscillation in quasi-phase-matched lithium niobate," *Applied Physics Letters* **69**(8), 1029–1031 (1996).
- [12] J. P. Meyn and M. M. Fejer, "Tunable ultraviolet radiation by second-harmonic generation in periodically poled lithium tantalate," *Optics Letters* **22**(16), 1214–1216 (1997).
- [13] K. C. Burr, C. L. Tang, M. A. Arbore, and M. M. Fejer, "Broadly tunable mid-infrared femtosecond optical parametric oscillator using all-solid-state-pumped periodically poled lithium niobate," *Optics Letters* **22**(19), 1458–1460 (1997).
- [14] S. D. Butterworth, P. G. R. Smith, and D. C. Hanna, "Picosecond Ti:Sapphire-pumped optical parametric oscillator based on periodically poled LiNbO<sub>3</sub>," *Optics Letters* **22**(9), 618–620 (1997).
- [15] M. H. Chou, I. Brener, M. M. Fejer, E. E. Chaban, and S. B. Christman, "1.5- $\mu$ m-band wavelength conversion based on cascaded second-order nonlinearity in LiNbO<sub>3</sub> waveguides," *IEEE Photonics Technology Letters* **11**(6), 654–656 (1999).
- [16] M. H. Chou, K. R. Parameswaran, M. M. Fejer, and I. Brener, "Multiple-channel wavelength conversion by use of engineered quasi-phase-matching structures in LiNbO<sub>3</sub> waveguides," *Optics Letters* **24**(16), 1157–1159 (1999).
- [17] M. J. Missey, V. Dominic, P. E. Powers, and K. L. Schepler, "Periodically poled lithium niobate monolithic nanosecond optical parametric oscillators and generators," *Optics Letters* **24**(17), 1227–1229 (1999).
- [18] A. Galvanauskas, A. Hariharan, D. Harter, M. A. Arbore, and M. M. Fejer, "High-energy femtosecond pulse amplification in a quasi-phase-matched parametric amplifier," *Optics Letters* **23**(3), 210–212 (1998).

- [19] Z. E. Penman, C. McGowan, P. Loza-Alvarez, D. T. Reid, M. Ebrahimzadeh, W. Sibbett, and D. H. Jundt, "Femtosecond optical parametric oscillators based on periodically poled lithium niobate," *Journal of Modern Optics* **45**(6), 1285–1294 (1998).
- [20] P. E. Powers, T. J. Kulp, and S. E. Bisson, "Continuous tuning of a continuous-wave periodically poled lithium niobate optical parametric oscillator by use of a fan-out grating design," *Optics Letters* **23**(3), 159–161 (1998).
- [21] P. Loza-Alvarez, D. T. Reid, P. Faller, M. Ebrahimzadeh, W. Sibbett, H. Karlsson, and F. Laurell, "Simultaneous femtosecond-pulse compression and second-harmonic generation in aperiodically poled  $\text{KTiOPO}_4$ ," *Optics Letters* **24**(15), 1071–1073 (1999).
- [22] F. Rotermund, V. Petrov, F. Noack, V. Pasiskevicius, J. Hellstrom, and F. Laurell, "Efficient femtosecond traveling-wave optical parametric amplification in periodically poled  $\text{KTiOPO}_4$ ," *Optics Letters* **24**(24), 1874–1876 (1999).
- [23] L. Gallman, G. Steinmeyer, U. Keller, G. Imeshev, and M. M. Fejer, "Generation of sub-6-fs blue pulses by frequency doubling with quasi-phase-matching gratings," *Optics Letters* **26**(9), 614–616 (2001).
- [24] K. R. Parameswaran, R. K. Route, J. R. Kurz, R. V. Roussev, and M. M. Fejer, "Highly efficient SHG in buried waveguides formed using annealed and reverse proton exchange," *Optics Letters* **27**(3), 179–181 (2002).
- [25] J. R. Kurz, A. M. Schober, D. S. Hum, A. J. Saltzman, and M. M. Fejer, "Nonlinear Physical Optics with Transversely Patterned Quasi-Phase-Matching Gratings," *IEEE Journal of Selected topics in Quantum Electronics* **8**(3), 660–664 (2002).
- [26] T. Ohara, H. Takara, I. Shake, K. Mori, S. Kawanishi, S. Mino, T. Yamada, M. Ishii, T. Kitoh, T. Kitagawa, K. R. Parameswaran, and M. M. Fejer, "160 Gbit/s optical-time-division multiplexing with PPLN hybrid integrated planar lightwave circuit," *IEEE Photonics Technology Letters* **15**(2), 302–304 (2003).
- [27] A. M. Schober, G. Imeshev, and M. M. Fejer, "Tunable-chirp pulse compression in quasi-phase-matched second-harmonic generation," *Optics Letters* **27**(13), 1129–1131 (2002).

- [28] K. A. Tillman, D. T. Reid, D. Artigas, J. Hellstrom, V. Pasiskevicius, and F. Laurell, “Low-threshold femtosecond optical parametric oscillator based on chirped-pulse frequency conversion,” *Optics Letters* **28**(7), 543–545 (2003).
- [29] N. E. Yu, S. Kurimura, K. Kitamura, J. H. Ro, M. Cha, S. Ashihara, T. Shimura, K. Kuroda, and T. Taira, “Efficient frequency doubling of a femtosecond pulse with simultaneous group-velocity matching and quasi phase matching in periodically poled, MgO-doped lithium niobate,” *Applied Physics Letters* **82**, 3388–3390 (2003).
- [30] Y. Guan, J. W. Haus, and P. Powers, “Broadband and off-axis optical parametric generation in periodically poled LiNbO<sub>3</sub>,” *Journal of the Optical Society of America B* **21**(6), 1225–1233 (2004).
- [31] J. Huang, J. Kurz, C. Langrock, A. M. Schober, and M. M. Fejer, “Quasi group-velocity matching using integrated-optic structures,” *Optics Letters* **29**(21), 2482–2484 (2004).
- [32] X. Xie, A. M. Schober, C. Langrock, R. V. Roussev, J. R. Kurz, and M. M. Fejer, “Picojoule threshold, picosecond optical parametric generation in reverse proton-exchanged lithium niobate waveguides,” *Journal of the Optical Society of America B* **21**(7), 1397–1399 (2004).
- [33] S. D. Yang, A. M. Weiner, K. R. Parameswaran, and M. M. Fejer, “400-photon-per-pulse ultrashort pulse autocorrelation measurement with aperiodically poled lithium niobate waveguides at 1.55  $\mu\text{m}$ ,” *Optics Letters* **29**(17), 2070–2072 (2004).
- [34] Z. Jiang, D. S. Seo, S. D. Yang, D. E. Leaird, R. V. Roussev, C. Langrock, M. M. Fejer, and A. M. Weiner, “Low-power high-contrast coded waveform discrimination at 10 GHz via nonlinear processing,” *IEEE Phot. Techn. Lett.* **16**, 1778–1780 (2004).
- [35] C. Langrock, E. Diamanti, R. Roussev, Y. Yamamoto, and M. M. Fejer, “Highly efficient single-photon detection at communication wavelengths by use of upconversion in reverse-proton-exchanged periodically poled LiNbO<sub>3</sub> waveguide,” *Optics Letters* **30**, 1725–1727 (2005).
- [36] H.-C. Chui, S. Shaw, M.-S. Ko, Y. Liu, J.-T. Shy, T. Lin, W.-Y. Cheng, R. Roussev, and M. M. Fejer, “Iodine stabilization of a diode laser in the optical communication band,” *Optics Letters* **30**, 646–648 (2005).

- [37] F. S. Chen, "Optically Induced Change of Refractive Indices in  $\text{LiNbO}_3$  and  $\text{LiTaO}_3$ ," *Journal of Applied Physics* **40**, 3389–3396 (1969).
- [38] A. M. Glass, D. von der Linde, D. H. Auston, and T. J. Negran, "Excited state polarization bulk photovoltaic effect, and the photorefractive effect in electrically polarized media," *J. Electron. Mater.* **4**(5), 915–943 (1975).
- [39] P. Yeh and C. Gu, *Landmark Papers on Photorefractive Nonlinear Optics* (World Scientific, 1995).
- [40] P. Gunther and J. P. Huignard, *Photorefractive Materials and Their Applications* (Springer-Verlag, Berlin, 1988).
- [41] R. W. Boyd, *Nonlinear Optics* (Academic Press, 1992).
- [42] N. Iyi, K. Kitamura, F. Izumi, J. K. Yamamoto, T. Hayashi, H. Asano, and S. Kimura, *J. Solid State Chem.* **101**, 340 (1992).
- [43] Y. Furukawa, K. Kitamura, A. Alexandrovski, R. K. Route, M. M. Fejer, and G. Foulon, *Applied Physics Letters* **78**, 1970 (2001).
- [44] G.-G. Zhong, J. Jian, and Z.-K. Wu, 11th International Quantum Electronics Conference, IEEE Cat. No. 80 **CH 1561-0**, 631 (1980).
- [45] D. A. Bryan, R. Gerson, and H. E. Tomaschke, "Increased optical damage resistance in lithium niobate," *Applied Physics Letters* **44**, 847–849 (1984).
- [46] R. Sommerfeldt, L. Holtmann, E. Kratzig, and B. Grabmaier, *Phys. Status Solidi A* **106**, 89 (1988).
- [47] Y. Furukawa, K. Kitamura, S. Takekawa, A. Miyamoto, M. Terao, and N. Suda, "Photorefraction in  $\text{LiNbO}_3$  as a function of  $[\text{Li}]/[\text{Nb}]$  and  $\text{MgO}$  concentration," *Appl. Phys. Lett.* **77**, 2494 (2000).
- [48] M. Jazbinsek, M. Zgonik, S. Takekawa, M. Nakamura, K. Kitamura, and H. Hatano, "Reduced space-charge fields in near-stoichiometric  $\text{LiTaO}_3$  for blue, violet, and near-ultraviolet light beams," *Appl. Phys. B* **75**, 891894 (2002).

- [49] M. Katz, R. K. Route, D. S. Hum, K. R. Parameswaran, G. D. Miller, , and M. M. Fejer, “Vapor-transport equilibrated near-stoichiometric lithium tantalate for frequency-conversion applications,” *Optics Letters* **29**, 1775–1777 (2004).
- [50] D. Hum, R. Route, and M. M. Fejer, Prepared for publication.
- [51] A. Grisard, E. Lallier, K. Polgár, and Á.Péter, “Low electric field periodic poling of thick stoichiometric lithium niobate,” *Electronics Letters* **36**, 1043–1044 (2000).
- [52] K. Polgár, Á.Péter, and M. Ferriol, “Phase relations in the growth of stoichiometric lithium niobate,” *Phys. Stat. Sol. (a)* **201**, 284–288 (2004).
- [53] Y. Furukawa, K. Kitamura, E. Suzuki, and K. Niwa, *J. Cryst. Growth* **197**, 889 (1999).
- [54] K. Kitamura, J. K. Yamamoto, N. Iyi, S. Kimura, and T. Hayashi, *J. Cryst. Growth* **116**, 327 (1992). Contains description of double crucible Czochralski growth.
- [55] Y. Furukawa, M. Sato, and F. Nitanda, “Growth and characterization of MgO-doped  $\text{LiNbO}_3$  for electro-optic devices,” *Journal of Crystal Growth* **99**, 832–836 (1990).
- [56] R. L. Holman, “Novel Uses of Gravimetry in the Processing of Crystalline Ceramics,” *Mater. Sci. Res.* **11**, 343 (1978).
- [57] R. L. Holman, P. J. Cressman, and J. F. Revelli, “Chemical control of optical damage in lithium niobate,” *Applied Physics Letters* **32**, 280–282 (1978).
- [58] D. H. Jundt, “Lithium Niobate: Single Crystal Fiber Growth and Quasi-phase-matching,” Ph.D. thesis, Stanford University (1991).
- [59] D. H. Jundt, M. M. Fejer, and R. L. Byer, “Optical Properties of Lithium-rich Lithium Niobate Fabricated by Vapor Transport Equilibration,” *IEEE Journal of Quantum Electronics* **26**, 135–138 (1990).
- [60] D. H. Jundt, M. M. Fejer, R. G. Norwood, and P. F. Bordui, “Composition dependence of lithium diffusivity in lithium niobate at high temperature,” *Journal of Applied Physics* **72**, 3468–3473 (1992).

- [61] P. F. Bordui, R. G. Norwood, D. H. Jundt, and M. M. Fejer, "Preparation and characterization of off-congruent lithium niobate crystals," *Journal of Applied Physics* **71**, 875–879 (1992).
- [62] V. Gopalan, T. E. Mitchell, Y. Furukawa, and K. Kitamura, "The role of nonstoichiometry in 180-degree domain switching of  $\text{LiNbO}_3$  crystals," *Applied Physics Letters* **72**(16), 1981–1983 (1998).
- [63] A. Kuroda, S. Kurimura, and Y. Uesu, "Domain inversion in ferroelectric  $\text{MgO}:\text{LiNbO}_3$  by applying electric fields," *Applied Physics Letters* **69**(11), 1565–1567 (1996).
- [64] K. Nakamura, J. Kurz, K. Parameswaran, and M. M. Fejer, "Periodic poling of magnesium-oxide-doped lithium niobate," *Journal of Applied Physics* **91**(7), 4528–4534 (2002).
- [65] H. Ishizuki, I. Shoji, and T. Taira, "Periodical poling characteristics of congruent  $\text{MgO}:\text{LiNbO}_3$  crystals at elevated temperature," *Applied Physics Letters* **82**(23), 4062–4064 (2003).
- [66] K. Mizuuchi, A. Morikawa, T. Sugita, and K. Yamamoto, "Electric-field poling in Mg-doped  $\text{LiNbO}_3$ ," *Journal of Applied Physics* **96**(11), 6585–6590 (2004).
- [67] K. Mizuuchi, K. Yamamoto, and M. Kato, *Electron. Lett.* **33**, 806 (1997). Provides details about 2D-electrode poling of  $\text{MgO-LN}$ .
- [68] T. Sugita, K. Mizuuchi, Y. Kitaoka, , and K. Yamamoto, "31%-efficient blue second-harmonic generation in a periodically poled  $\text{MgO}:\text{LiNbO}_3$  waveguide by frequency doubling of an  $\text{AlGaAs}$  laser diode," *Optics Letters* **24**(22), 1590–1592 (1999).
- [69] A. Harada and Y. Nihei, "Bulk periodically poled  $\text{MgO-LiNbO}_3$  by corona discharge method," *Appl. Phys. Lett.* **69**(18), 2629–2631 (1996).
- [70] M. M. Fejer, G. A. Magel, D. H. Jundt, and R. L. Byer, "Quasi-Phase-Matched Second Harmonic Generation: Tuning and Tolerances," *IEEE Journal of Quantum Electronics* **28**(11), 2631–2654 (1992).

- [71] L. E. Myers, R. C. Eckardt, M. M. Fejer, R. L. Byer, W. R. Bosenberg, and J. W. Pierce, "Quasi-phase-matched optical parametric oscillators in bulk periodically poled LiNbO<sub>3</sub>," *Journal of the Optical Society of America B* **12**(11), 2102–2116 (1995).
- [72] K. Kintaka, M. Fujimura, T. Suhara, and H. Nishihara, *IEEE J. Lightwave Technol.* **14**, 462 (1996).
- [73] S. Nagano, M. Konishi, T. Shiomi, and M. Minakata, "Study on Formation of Small Polarization Domain Inversion for High-Efficiency Quasi-Phase-Matched Second-Harmonic Generation Device," *Jpn. J. Appl. Phys.* **42**, 43344339 (2003).
- [74] R. V. Roussev, R. Route, M. Katz, D. Jundt, C. Kajiyama, and M. Fejer, "Vapor transport equilibrated lithium niobate resistant to photorefractive damage," *Proceedings of SPIE* **4**, 5710–5719 (2005).
- [75] R. V. Roussev, R. Route, J. Schaar, K. Urbanek, M. M. Fejera, D. Jundt, and C. Kajiyama, "Periodically poled vapor transport equilibrated lithium niobate for visible light generation," *Proceedings of SPIE* **6103-2 V. 3** (2006).
- [76] H. Ishizuki and T. Taira, Private communication (2006).
- [77] K. Kitamura, Presented at Photonics West SPIE conference, San Jose, CA (2006).
- [78] D. Marcuse, *Theory of dielectric optical waveguides, 2nd ed.* (Boston, Harcourt, 1991).
- [79] R. L. Byer, *Nonlinear Optics*, chap. Parametric oscillators and nonlinear materials, pp. 47–160 (Academic, San Francisco, 1977).
- [80] M. L. Bortz, S. J. Field, M. M. Fejer, D. W. Nam, R. G. Waarts, and D. F. Welch, "Noncritical Quasi-phase-matched Second Harmonic Generation in an Annealed Proton-exchanged LiNbO<sub>3</sub> Waveguide," *IEEE Transactions on Quantum Electronics* **30**, 2953 (1994).
- [81] J. L. Jackel, C. E. Rice, and J. J. Veselka, "Proton exchange for high index waveguides in LiNbO<sub>3</sub>," *Appl. Phys. Lett.* **41**, 607–608 (1982).
- [82] E. Y. B. Pun, K. K. Loi, S. A. Zhao, and P. S. Chung, "Experimental studies of proton-exchanged lithium niobate waveguides using cinnamic acid," *Applied Physics Letters* **59**, 662–664 (1991).

- [83] Y. N. Korkishko, V. A. Fedorov, and O. Y. Feoktistova, "LiNbO<sub>3</sub> Optical Waveguide Fabrication by High-Temperature Proton Exchange," *J. Lightwave Technol.* **18**(4), 562–568 (2000).
- [84] W. J. Liao, X. Chen, F. Chen, Y. Chen, Y. Xia, and Y. Chen, "Proton-exchanged optical waveguides fabricated by glutaric acid," *Optics & Laser Technology* **36**, 603–606 (2004).
- [85] K. Yamamoto and T. Taniuchi, "Characteristics of pyrophosphoric acid proton-exchanged waveguides in LiNbO<sub>3</sub>," *Journal of Applied Physics* **70**, 6663–6668 (1991).
- [86] K. Yamamoto, K. Mizuuchi, and K. Takeshige, "Characteristics of periodically domain-inverted LiNbO<sub>3</sub> and LiTaO<sub>3</sub> waveguides for second harmonic generation," *Journal of Applied Physics* **70**, 1947–1951 (1991).
- [87] E. Y. B. Pun, K. K. Loi, and P. S. Chung, "Proton-exchanged Optical Waveguides in Z-cut LiNbO<sub>3</sub> Using Phosphoric Acid," *IEEE Transactions on Lightwave Technology* **11**, 277–284 (1993).
- [88] J. Rams and J. M. Cabrera, "Characterization of LiNbO<sub>3</sub> waveguides fabricated by proton exchange in water," *Applied Physics A: Materials Science & Processing* **81**(1), 205–208 (2005).
- [89] Y. N. Korkishko, V. A. Fedorov, and S. M. Kostritskii, "Optical and x-ray characterization of  $H_xLi_{1-x}NbO_3$  phases in proton-exchanged LiNbO<sub>3</sub> optical waveguides," *Journal of Applied Physics* **84**, 2411–2419 (1998).
- [90] D. J. Bamford and D. J. Cook, "Proton exchange in glycerol: a new technique for fabricating nonlinear optical waveguides," *Conference on Lasers and Electro-optics (CLEO)* (2003).
- [91] V. A. Ganshin and Y. N. Korkishko, "Stress and strain in H:LiNbO<sub>3</sub> optical waveguides," *Sov. Phys. Tech. Phys.* **37**, 49–54 (1992).
- [92] T. Veng, T. Skettrup, and K. Pedersen, "Second-order optical nonlinearities in dilute melt proton exchange waveguides in z-cut LiNbO<sub>3</sub>," *Appl. Phys. Lett.* **69**, 2333–2335 (1996).

- [93] T. Veng and T. Skettrup, "Dilute-melt, proton-exchange slab waveguides in LiNbO<sub>3</sub>: a new fabrication and characterization method," *Applied Optics* **36**, 59415,948 (1997).
- [94] J. Rams, J. Olivares, and J. M. Cabrera, "High-index proton-exchanged waveguides in Z-cut LiNbO<sub>3</sub> with undegraded nonlinear optical coefficients," *Applied Physics Letters* **70**, 2076–2078 (1997).
- [95] J. Rams and J. M. Cabrera, "Nonlinear optical efficient LiNbO<sub>3</sub> waveguides proton exchanged in benzoic acid vapor: Effect of the vapor pressure," *Journal of Applied Physics* **85**(3), 1322–1328 (1999).
- [96] J. Rams and J. M. Cabrera, "Preparation of proton-exchange LiNbO<sub>3</sub> waveguides in benzoic acid vapor," *Journal of the Optical Society of America B* **16**(3), 401–406 (1999).
- [97] R. Osellame, R. Ramponi, M. Marangoni, and V. Russo, "Waveguide fabrication in LiTaO<sub>3</sub> by vapour-phase proton-exchange," *Electronics Letters* **36**(5), 431–433 (2000).
- [98] D. Tsou, M. Choub, P. Santhanaraghavan, Y. Chena, and Y. Huang, "Structural and optical characterization for vapor-phase proton exchanged lithium niobate waveguides," *Materials Chemistry and Physics* **78**, 474479 (2002).
- [99] J. L. Jackel and C. E. Rice, "Short- and long-term stability in proton exchanged lithium niobate waveguides," *SPIE* **460**, 43–48 (1984).
- [100] M. Minakata, K. Kumagai, and S. Kawakami, "Lattice constant changes and electro-optic effects in proton-exchanged LiNbO<sub>3</sub> optical waveguides," *Applied Physics Letters* **49**(16), 992–994 (1986).
- [101] Y. Kondo, L. Hu, and Y. Fujii, "Exact determination of electro-optic constants of single-mode proton-exchanged guiding layers," *Trans. of the IEICE* **E71**, 1122–1126 (1988).
- [102] M. Rottschalk, A. Rasch, and W. Karthe, "Efficient electro-optic x-switch using proton exchanged LiNbO<sub>3</sub> channel waveguides," *J. Opt. Commun.* **10**, 1326–1328 (1989).
- [103] F. Laurell, M. G. Roelofs, and H. Hsiung, "Loss of optical nonlinearity in proton-exchanged LiNbO<sub>3</sub> waveguides," *Appl. Phys. Lett.* **60**, 301–303 (1992).

- [104] M. L. Bortz and M. M. Fejer, "Measurement of the second-order nonlinear susceptibility of proton-exchanged LiNbO<sub>3</sub>," *Opt. Lett.* **17**, 704–706 (1992).
- [105] W. Hsu, C. S. Willand, V. Gopalan, and M. C. Gupta, "Effect of proton exchange on the nonlinear optical properties of LiNbO<sub>3</sub> and LiTaO<sub>3</sub>," *Appl. Phys. Lett.* **61**, 2263–2265 (1992).
- [106] P. G. Suchoski, T. K. Findakly, and F. J. Leonberger, "Stable low-loss proton-exchanged LiNbO<sub>3</sub> waveguide devices with no electro-optic degradation," *Optics Letters* **13**, 1050–1052 (1988).
- [107] A. Loni, G. Hay, R. M. D. L. Rue, and J. M. Winfield, "Proton-exchanged LiNbO<sub>3</sub> waveguides: The effects of post-exchange annealing and buffered melts as determined by infrared spectroscopy, optical waveguide measurements and hydrogen isotopic exchange reactions," *J. Lightwave Technol.* **7**, 911–919 (1989).
- [108] M. L. Bortz, L. A. Eyres, and M. M. Fejer, "Depth profiling of the d<sub>33</sub> nonlinear coefficient in annealed proton exchanged LiNbO<sub>3</sub> waveguides," *Applied Physics Letters* **62**, 2012–2014 (1993).
- [109] V. A. Ganshin, Y. N. Korkishko, and V. Z. Petrova, "Reverse ion exchange in H:LiNbO<sub>3</sub> optical waveguides," *Zh. Techn. Fiz.* **58**, 1168–1170 (1988).
- [110] V. A. Ganshin and Y. N. Korkishko, "Some features of reverse ion exchange in H:LiNbO<sub>3</sub> optical waveguides," *Sov. Phys. Tech. Phys.* **35**, 1095–1096 (1988).
- [111] J. L. Jackel and J. J. Johnson, "Reverse exchange method for burying proton exchanged waveguides," *Electronics Letters* **27**, 1360–1361 (1991).
- [112] J. Olivares and J. M. Cabrera, "Guided modes with ordinary refractive index in proton exchanged LiNbO<sub>3</sub> waveguides," *Applied Physics Letters* **62**, 2648–2670 (1993).
- [113] Y. N. Korkishko, V. A. Fedorov, S. V. Katin, and A. V. Kondratiev, "Reverse proton exchange in LiTaO<sub>3</sub> and LiNbO<sub>3</sub> for buried optical waveguides," *Proceedings of the SPIE* **2401**, 149–161 (1995).
- [114] K. E. Hadi, M. Sundheimer, P. Aschieri, P. Baldi, M. P. D. Micheli, D. B. Ostrowsky, and F. Laurell, "Quasi-phase-matched parametric interactions in proton-exchanged lithium niobate waveguides," *J. Opt. Soc. Am. B* **14**, 3197–3203 (1997).

- [115] Y. N. Korkishko, V. A. Fedorov, E. A. Baranov, M. V. Proyaeva, T. V. Morozova, F. Caccavale, F. Segato, C. Sada, and S. M. Kostritskii, "Characterization of  $\alpha$ -phase soft proton-exchanged LiNbO<sub>3</sub> optical waveguides," *J. Opt. Soc. Am. A* **18**, 1186–1191 (2001).
- [116] J. Rams, F. Agulló Rueda, and J. M. Cabrera, "Structure of high index proton exchange LiNbO<sub>3</sub> waveguides with undegraded nonlinear optical coefficients," *Applied Physics letters* **71**(23), 3356–3358 (1997).
- [117] C. E. Rice, *J. Solid. St. Chem.* **64**, 188 (1986).
- [118] V. A. Ganshin and Y. N. Korkishko, *J. Opt. Commun* **13**, 2 (1992).
- [119] V. A. Fedorov and Y. N. Korkishko, *Proceedings of the SPIE* **2291**, 243 (1995).
- [120] Y. N. Korkishko and V. A. Fedorov, "Relationship between refractive indices and hydrogen concentration in proton exchanged LiNbO<sub>3</sub> waveguides," *Journal of Applied Physics* **82**(3), 1010–1017 (1997).
- [121] D. F. Clark, A. C. G. Nutt, K. K. Wong, P. J. R. Laybourn, and R. M. D. L. Rue, "Characterization of proton-exchange slab optical waveguides in z-cut LiNbO<sub>3</sub>," *Journal of Applied Physics* **54**, 6218–6220 (1983).
- [122] W. Bollmann, "Diffusion of Hydrogen (OH<sup>-</sup> ions) in LiNbO<sub>3</sub> crystals," *Phys. Stat. Sol. (a)* **104**, 643–648 (1987).
- [123] V. A. Ganshin and Y. N. Korkishko, "Kinetic model of proton-lithium exchange in LiNbO<sub>3</sub> and LiTaO<sub>3</sub> crystals: The role of cation vacancies," *Solid State Ionics* **58**, 23–32 (1992).
- [124] S. T. Vohra, A. R. Mickelson, and S. E. Asher, "Diffusion characteristics and waveguiding properties of proton-exchanged and annealed LiNbO<sub>3</sub> channel waveguides," *Journal of Applied Physics* **66**, 5161–5174 (1989).
- [125] L. Kovács, K. Polgár, R. Capelletti, and C. Mora, "Diffusion of Hydrogen Isotopes in Pure and Mg-Doped LiNbO<sub>3</sub> crystals," *Phys. Stat. Sol. (a)* **120**, 97–104 (1990).
- [126] M. L. Bortz and M. M. Fejer, "Annealed proton-exchanged LiNbO<sub>3</sub> waveguides," *Optics Letters* **16**, 1844–1846 (1991).

- [127] J. M. Zavada, H. C. Casey, C.-H. Chen, and A. Loni, "Correlation of refractive index profiles with substitutional hydrogen concentrations in annealed proton-exchanged LiNbO<sub>3</sub> waveguides," *Applied Physics Letters* **62** (1993).
- [128] J. M. Zavada, H. C. Casey, R. J. States, S. W. Novak, and A. Loni, "Correlation of substitutional hydrogen to refractive index profiles in annealed proton-exchanged Z- and X-cut LiNbO<sub>3</sub>," *Journal of Applied Physics* **77**, 2697–2708 (1995).
- [129] T. Veng and T. Skettrup, "Ion Exchange Model for  $\alpha$  Phase Proton Exchange Waveguides in LiNbO<sub>3</sub>," *Journal of Lightwave Technology* **16**, 646–649 (1998).
- [130] Y. N. Korkishko, V. A. Fedorov, O. Y. Feoktistova, and T. V. Morozova, "Effect of SiO<sub>2</sub> cladding on properties of annealed proton-exchanged LiNbO<sub>3</sub> waveguides," *Journal of Applied Physics* **87**, 4404–4409 (2000).
- [131] J. M. M. M. de Almeida and A. M. P. P. Leite, "Proton exchanged waveguides in LiNbO<sub>3</sub>: characterization and design methodology," *Proceedings of SPIE* **6123**, 612,319–1–613,219–12 (2006).
- [132] G. S. Kanter, P. Kumar, R. V. Roussev, J. R. Kurz, K. R. Parameswaran, and M. M. Fejer, "Squeezing in a LiNbO<sub>3</sub> integrated optical waveguide circuit," *Optics Express* **10**(3) (2002).
- [133] R. Ulrich and R. Torge, "Measurement of thin film parameters with a prism coupler," *Applied Optics* **12**(12), 1901–2908 (1973).
- [134] J. M. White and P. F. Heidrich, "Optical waveguide refractive index profiles determined from measurement of mode indices: a simple analysis," *Applied Optics* **15**(1), 151–155 (1976).
- [135] Y. M. Dikaev, Y. L. Kopylov, and I. M. Kotelyanskii, "A simple method of determining the profiles of diffused waveguides," *Sov. J. Quantum Electron.* **11**(2), 225–226 (1981).
- [136] K. S. Chiang, "Construction of refractive-index profiles of planar dielectric waveguides from the distribution of effective indexes," *Journal of Lightwave Technology* **LT-3**(2), 385–391 (1985).

- [137] K. S. Chiang, “Simplified universal dispersion curves for graded-index planar waveguides based on the WKB method,” *Journal of Lightwave Technology* **13**(2), 158–162 (1995).
- [138] L. P. Shi, E. Y. B. Pun, and P. S. Chung, “Extended IWKB method for determination of the refractive-index profile in optical waveguides,” *Optics Letters* **20**(15), 1622–1624 (1995).
- [139] J. Cabrera, J. Olivares, M. Carrascosa, J. Rams, R. Muller, and E. Diegues, “Hydrogen in lithium niobate,” *Advances in Physics* **45**(5), 349 – 392 (1996).
- [140] L. Kovács, M. Wolecke, M. Jovanovic, K. Polgár, and S. Kapphan, *J. Phys. Chem. Solids* **52**, 797 (1991).
- [141] J. Weickert, B. M. ter Haar Romeny, and M. A. Viergever, “Efficient and reliable schemes for nonlinear diffusion filtering,” *IEEE Transactions on Image Processing* **7**(3), 398–410 (1998).
- [142] W. H. Press, B. P. Flannery, S. A. Teukolsky, and W. T. Vetterlin, *Numerical recipes in C: the art of scientific computing* (Cambridge University Press, 1988).
- [143] K. R. Parameswaran, “Highly Efficient Optical Frequency Mixing,” Ph.D. thesis, Stanford University (2002).
- [144] F. Helfferich and M. S. Plesset, “Ion exchange kinetics. A nonlinear diffusion problem,” *Journal of Chemical Physics* **28**(3), 418–424 (1958).
- [145] D. H. Jundt, “Temperature-dependent Sellmeier equation for the index of refraction,  $n_e$ , in congruent lithium niobate,” *Optics Letters* **22**(20), 1553–1555 (1997).
- [146] X. Xie, Private communication (2003).
- [147] S. Sharpe, Private communication.
- [148] R. Regener and W. Sohler, “Loss in low-finesse Ti:LiNbO<sub>3</sub> optical waveguide resonators,” *Applied Physics B* **36**, 143–147 (1985).
- [149] Y. N. Korkishko and V. A. Fedorov, *Ion exchange in single crystals for integrated optics and optoelectronics* (Cambridge, MA: Cambridge International Science, 1999).

- [150] Y. N. Korkishko, V. A. Fedorov, and F. Laurell, "The SHG-Response of Different Phases in Proton Exchanged Lithium Niobate Waveguides," *IEEE Journal of Selected Topics in Quantum Electronics* **6**(1), 132–142 (2000).
- [151] R. V. Roussev, C. Langrock, J. R. Kurz, and M. M. Fejer, "Periodically poled lithium niobate waveguide sum-frequency generator for efficient single-photon detection at communication wavelengths," *Optics Letters* **29**(13), 1518–1520 (2004).
- [152] M. H. Chou, K. R. Parameswaran, M. A. Arbore, J. Hauden, and M. M. Fejer, "Bidirectional wavelength conversion between 1.3- and 1.5-  $\mu\text{m}$  telecommunication bands using difference frequency mixing in  $\text{LiNbO}_3$  waveguides with integrated coupling structures," *Conference on Lasers and Electro-Optics Technical Digest Series* **6**, Paper CThZ2 (1998).
- [153] H. Herrmann and W. Sohler, "Difference-frequency generation of tunable, coherent mid-infrared radiation in  $\text{Ti:LiNbO}_3$  channel waveguides," *J. Opt. Soc. Am. B* **5**, 278 – 284 (1988).
- [154] D. Hofmann, G. Schreiber, C. Haase, H. Herrmann, W. Grundkotter, R. Ricken, and W. Sohler, "Quasi-phase-matched difference-frequency generation in periodically poled  $\text{Ti:LiNbO}_3$  channel waveguides," *Optics Letters* **24**(13), 896 – 898 (1999).
- [155] E. J. Lim, H. M. Hertz, M. L. Bortz, and M. M. Fejer, "Infrared radiation generated by quase-phase-matched difference-frequency mixing in a periodically poled lithium-niobate waveguide," *Applied Physics Letters* **59**(18), 2207–2209 (1991).
- [156] K. Petrov, A. Roth, T. Patterson, T. Thoms, L. Huang, A. Ryan, and D. Bamford, "Efficient difference-frequency mixing of diode lasers in lithium niobate channel waveguides," *Appl. Phys. B* **70**, 777 – 782 (2000).
- [157] T. Yanagawa, O. Tadanaga, Y. Nishida, H. Miyazawa, K. Magari, M. Asobe, and H. Suzuki, "Efficient broadband difference frequency generation in a direct-bonded periodically-poled  $\text{LiNbO}_3$  waveguide and the observation of CO isotopomer absorption from 2.3 to 2.45  $\mu\text{m}$ ," *Proc. SPIE* **6103**, 61,030O–1 – 8 (2006).
- [158] R. Roussev, A. K. Sridharan, K. Urbanek, R. Byer, and M. Fejer, "Parametric amplification of 1.6  $\mu\text{m}$  signal in anneal- and reverse- proton exchanged waveguides," in

- IEEE LEOS Annual Meeting Conference Proceedings, 27-28 Oct. 2003, Tucson, AZ, USA*, vol. 1, pp. 334 – 335 (2003).
- [159] A. K. Sridharan, Ph.D. thesis, Stanford University (2007).
- [160] A. M. Glass, “The photorefractive effect,” *Optical Engineering* **17**, 470–479 (1978).
- [161] F. Jermann, M. Simon, and E. Kratzig, “Photorefractive properties of congruent and stoichiometric lithium niobate at high light intensities,” *Journal of the Optical Society of America* **12**(11), 2066–2070 (1995).
- [162] T. Volk, N. Rubina, and M. Wohlecke, “Optical-damage-resistant impurities in lithium niobate,” *J. Opt. Soc. Am. B* **11**(9), 1681–1687 (1994).
- [163] M. Fontana, K. Chah, M. Aillerie, R. Mouras, and P. Bourson, “Optical damage resistance in undoped LiNbO<sub>3</sub> crystals,” *Optical Materials* **16**, 111–117 (2001).
- [164] K. Kitamura, Y. Furukawa, Y. Li, M. Zgonik, C. Medrano, G. Montemezzani, and P. Gunter, “Photorefractive effect in LiNbO<sub>3</sub> crystals enhanced by stoichiometry control,” *Journal of Applied Physics* **82**, 1006–1009 (1997).
- [165] Y. Furukawa, M. Sato, K. Kitamura, and Y. Yajima, “Optical damage resistance and crystal quality of LiNbO<sub>3</sub> single crystals with various [Li]/[Nb] ratios,” *Journal of Applied Physics* **72**, 3250–3254 (1992).
- [166] M. Katz, R. Route, A. Alexandrovski, M. Fejer, M. C. C. Custodio, and D. H. Jundt, “Characterization of near-stoichiometric 1 % Mg-doped LiNbO<sub>3</sub> fabricated by vapor transport equilibration,” in *Conference on Lasers and Electro-Optics*, p. Paper CThT4 (2003).
- [167] Y. Furukawa, K. Kitamura, S. Takekawa, K. Niwa, and H. Hatano, *Opt. Lett.* **23**, 1892 (1998).
- [168] S. Bredikhin, S. Scharner, M. Klinger, V. Kveder, B. Redkin, and W. Weppner, “Nonstoichiometry and electrocoloration due to injection of Li<sup>+</sup> and O<sup>2-</sup> ions into lithium niobate crystals,” *Journal of Applied Physics* **88**(10), 5687–5694 (2000).
- [169] A. Alexandrovski, G. Foulon, L. E. Myers, R. K. Route, and M. M. Fejer, *Proceedings of SPIE* **3610**, 44 (1999).

- [170] U. Schlarb and K. Betzler, "Refractive indices of lithium niobate as a function of wavelength and composition," *Journal of Applied Physics* **73**(7), 3472–3476 (1993).
- [171] Y. lin Chen, C. bo Lou, Z. heng Huang, S. lin Chen, L. Zhang, and S. guo Liu, "Green Light Generation in Stoichiometric Mg:LiNbO<sub>3</sub> Periodically Poled by Lower Electric Field," *Chinese Journal of Luminescence* **23**(3), 253–256 (2003).
- [172] Y.-H. Chen, J.-H. Yao, B.-X. Yan, H.-L. Deng, Y.-F. Kong, S.-L. Chen, J.-J. Xu, and G.-Y. Zhang, "Harmonic violet light generation in periodically poled bulk near-stoichiometric MgO-doped LiNbO<sub>3</sub>," *Optics Communications* **224**, 149153 (2003).
- [173] L. E. Myers, "Quasi-phasematched optical parametric oscillators in bulk periodically poled lithium niobate," Ph.D. thesis, Stanford University (1995).
- [174] G. D. Miller, "Periodically Poled Lithium Niobate: Modeling, Fabrication and Nonlinear-optical Performance," Ph.D. thesis, Stanford University (1998).
- [175] M. Molotskii, R. Kris, and G. Rosenman, "Fluctuon effects in ferroelectric polarization switching," *Journal of Applied Physics* **88**(9), 5318–5327 (2000).
- [176] V. Y. Shur, E. V. Nikolaeva, E. I. Shishkin, A. P. Chernykh, K. Terabe, K. Kitamura, H. Ito, and K. Nakamura, "Domain shape in congruent and stoichiometric lithium tantalate," *Ferroelectrics* **269**, 195–200 (2002).
- [177] V. Y. Shur, E. L. Rumyantsev, E. V. Nikolaeva, E. I. Shishkin, R. G. Batchko, M. M. Fejer, R. L. Byer, and I. Mnushkina, "Domain kinetics in congruent and stoichiometric lithium niobate," *Ferroelectrics* **269**, 189–194 (2002).
- [178] A. P. Chernykh, V. Y. Shur, E. V. Nikolaeva, E. I. Shishkin, A. G. Shur, K. Terabe, S. Kurimura, K. Kitamura, and K. Gallo, "Shapes of isolated domains and field induced evolution of regular and random 2D domain structures in LiNbO<sub>3</sub> and LiTaO<sub>3</sub>," *Materials Science and Engineering: B* **120**(1-3), 109–113 (2005).
- [179] V. Y. Shur, "Kinetics of Ferroelectric Domains: Application of General Approach to LiNbO<sub>3</sub> and LiTaO<sub>3</sub>," *Journal of Material Science* **41**(1), 199–210 (2006).
- [180] A. I. Lobov, V. Y. Shur, I. S. Baturin, E. I. Shishkin, D. K. Kuznetsov, A. G. Shur, M. A. Dolbilov, and K. Gallo, "Field Induced Evolution of Regular and Random 2D

- Domain Structures and Shape of Isolated Domains in  $\text{LiNbO}_3$  and  $\text{LiTaO}_3$ ,” *Ferroelectrics* **341**, 109–116 (2006).
- [181] V. Y. Shur, Private communication.
- [182] H. Takesue, E. Diamanti, T. Honjo, C. Langrock, M. M. Fejer, K. Inoue, and Y. Yamamoto, “Differential phase shift quantum key distribution experiment over 105 km fibre,” *New J. Phys* **7**, 232 (2005).
- [183] Z. Jiang, D. S. Seo, D. E. Leaird, A. M. Weiner, R. V. Roussev, C. Langrock, and M. M. Fejer, “Multi-user, 10Gb/s spectrally phase coded O-CDMA system with hybrid chip and slot-level timing coordination,” *IEICE Electronics Express* **1**, 398–403 (2004).
- [184] Z. Jiang, D. Seo, S. Yang, D. Leaird, R. Roussev, C. Langrock, M. Fejer, and A.M.Weiner, “Four-user 10-Gb/s spectrally phase-coded O-CDMA system operating at  $\sim 30$  fJ/bit,” *IEEE Phot. Techn. Lett.* **17**, p.705–707 (2005).
- [185] H.-C. Chui, Y.-W. Liu, J.-T. Shy, S.-Y. Shaw, R. V. Roussev, and M. M. Fejer, “Frequency-stabilized 1520-nm diode laser with rubidium  $5S_{1/2}$  to  $7S_{1/2}$  two-photon absorption,” *Appl. Opt.* **43**, 6348–51 (2004).
- [186] T. Ohara, H. Takara, I. Shake, K. Mori, K. Sato, S. Kawanishi, S. Mino, I. Yamada, A. Ishii, I. Ogawa, T. Kitoh, K. Magari, A. Okamoto, R. V. Roussev, J. R. Kurz, K. R. Parameswaran, and M. M. Fejer, “160-Gb/s OTDM transmission using integrated all-optical MUX/DEMUX with all-channel modulation and demultiplexing,” *IEEE Phot. Techn. Lett.* **16**, 650–652 (2004).
- [187] G. Leo, A. Amoroso, L. Colace, G. Assanto, R. V. Roussev, and M. M. Fejer, “Low-threshold spatial solitons in reverse-proton-exchanged periodically poled lithium niobate waveguides,” *Opt. Lett.* **29**, 1778–1780 (2004).
- [188] R. V. Roussev, M. M. Fejer, J. Tian, and L. Zhang, “Highly efficient SHG using non-critical quasi-phase-matching for the  $\text{TM}_{01}$  mode in annealed proton-exchange waveguides in 5% MgO-doped  $\text{LiNbO}_3$ ,” in *Conference on Lasers and Electro-Optics*, p. CTuT5 (2003).